The Magnetic Structure of Ferromagnetic Filaments of a CoNi(P) Alloy in a Porous Silicon Matrix

R. S. Iskhakov[a], S. V. Komogortsev[a], L. A. Chekanova[a], A. D. Balaev[a], V. A. Yuzova[b], and O. V. Semenova[b]

[a] *Kirensky Institute of Physics, Siberian Division, Russian Academy of Sciences, Krasnoyarsk, Russia*
[b] *Krasnoyarsk State Technical University, Krasnoyarsk, Russia*
Received October 8, 2002

Abstract—The magnetic and resonance properties of CoNi(P) alloys, synthesized by chemical deposition as films on single crystal silicon substrates and as filaments in linear pores of porous silicon substrates, were studied by magnetization and ferromagnetic resonance measurements. It is established that CoNi(P) alloys of the same composition but different morphologies occur in states characterized by different degrees of nonequilibrium, which is manifested by different modes of the magnetization approach to saturation. © 2003 MAIK "Nauka/Interperiodica".

In the past decade, there has been extensive development of the technology of novel magnetic materials representing magnetic filaments formed through chemical deposition of fine particles possessing desired properties inside linear pores of a matrix, for example, porous silicon (por-Si) [1]. Investigation of the structural features of such objects by conventional diffraction methods is rather difficult, because a small volume fraction of the magnetic filaments in a composite sample makes the integral diffraction measurements insufficiently informative. For this reason, it is a usual practice to study the structure of single filaments (isolated from the matrix) by means of transmission and scanning electron microscopy [2, 3]. Experimental investigation of the micromagnetic structure of ferromagnetic filaments in nonmagnetic matrices encounters analogous difficulties. This probably accounts for the fact that, to our knowledge, no experimental data on the magnetic structure of such filaments have been reported so far.

In recent years, the crystal structure and magnetic microstructure of nanocrystalline materials, amorphous alloys, and ensembles of small particles are frequently studied by an indirect method based on the analysis of magnetization approach to saturation [4–7]. We have used this magnetostructural approach to study the magnetic and resonance properties of CoNi(P) alloys chemically deposited as films on single crystal silicon plates and as filaments in linear pores of por-Si substrates. This investigation allowed us to compare the peculiarities in magnetic response related to both geometric shape and structural features of the ferromagnetic material.

The layers of porous silicon were obtained by anodic dissolution in aqueous hydrofluoric acid solutions. Variable parameters included the HF–H_2O solution composition (component volume ratio $x : y$), current density ($j = 5$–30 mA/cm^2), and anodizing time ($t = 10$–180 min) at a constant applied dc voltage ($U = 10$ V). The resulting porous structure was studied in an optical microscope (JENAVERT, Germany) at a magnification of x_{250} and x_{630}. Figure 1 shows the microphotographs of two porous samples cleaved upon the electrochemical treatment in different regimes. These substrates were used for depositing ferromagnetic CoNi(P) filaments. The images reveal well-defined cylindrical pores perpendicular to the sample surface, with a diameter of 1–2 μm and a length (depth) of 10–100 μm.

Ferromagnetic filaments of a CoNi(P) alloy were grown in the pores of silicon plates by means of a heterogeneous reaction of metal reduction from an aqueous solution of cobalt ($CoSO_4$) and nickel ($NiSO_4$) salts under the action of a reducing agent—sodium hypophosphite (NaH_2PO_2) at $T = 80°C$. Reference films were prepared by chemical deposition from the same system onto a polished single crystal silicon surface. A comparison of the samples obtained on porous and single crystal silicon substrates allowed us to reveal the features of magnetic response related to geometric shape of the ferromagnetic material.

The magnetic properties of the ferromagnetic filaments and planar layers synthesized as described above were studied using the ferromagnetic resonance (FMR) and magnetization techniques. The measurements were performed on an EPA-2M spectrometer operating at a frequency of $f = 9.2$ GHz and on a vibrating-sample magnetometer in a range of magnetic fields up to 10 kOe.

The magnetization curves and the FMR spectra obtained for various experimental geometries (Figs. 2 and 3) revealed a magnetic anisotropy in the direction of linear pores (oriented perpendicularly to the silicon plate surface). The FMR data allowed the nature of this
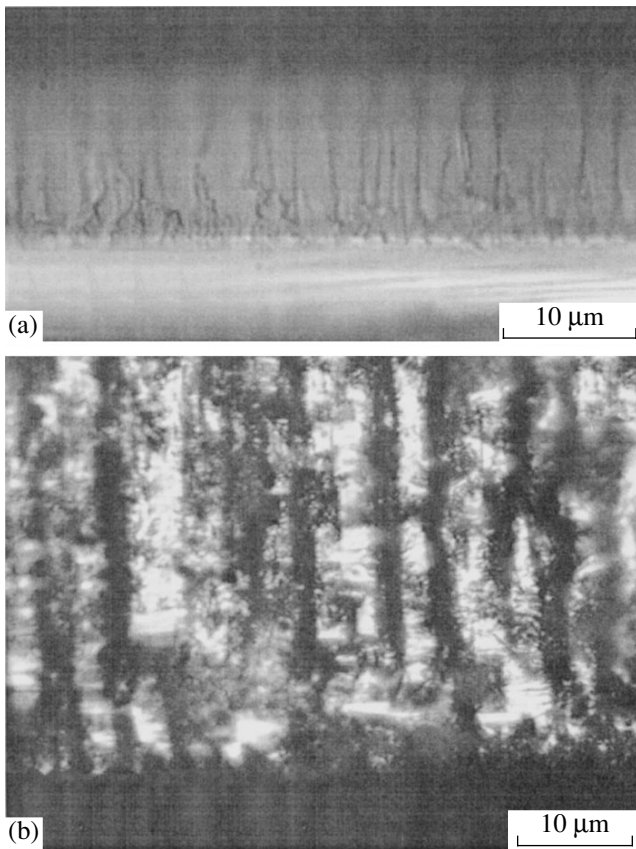
Fig. 1. Microphotographs of cleaved silicon plates upon anodization in an HF–H$_2$O (1 : 1) solution for 60 min at $U = 10$ V: (a) $j = 64$ mA/cm^2 (highly doped silicon); (b) $j = 105$ mA/cm^2.
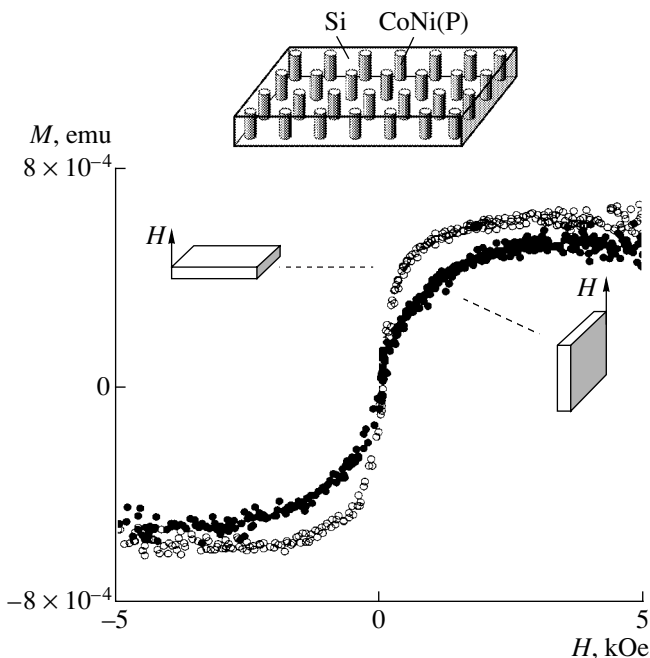

Fig. 2. Magnetization curves of the samples with ferromagnetic CoNi(P) filaments in a por-Si matrix (the inset on top shows a schematic diagram of the system).

anisotropy to be identified as the shape anisotropy. Figure 3 presents the FMR spectra of magnetic filaments of a CoNi(P) alloy in por-Si in comparison to the spectra of films of the same alloy on single crystal substrates, measured in different geometries. As can be seen, the two kinds of samples are characterized by significantly different values of the resonance fields H_r observed for the same material, substrate orientation, and applied field strength. This is explained by the material occurring in different morphological modifications.

The resonance field strength H_r is given by the formula [8]

$$\omega_H = |\gamma|\{[H_r + (N_x - N_z)M_z][H_r + (N_y - N_z)M_z]\}^{1/2}, \quad (1)$$

where $|\gamma| = 2.8$ MHz/Oe, M_z is the effective magnetization and N is the demagnetizing factor related to the shape of the ferromagnetic material. Substituting the experimental resonance fields into this formula with $N_x = N_y = 0$, $N_z = 4\pi$ for the field **H** perpendicular to a CoNi(P) film and $N_z = N_y = 0$, $N_x = 4\pi$ for the field **H** parallel to the film, we determined the effective magnetization of the alloy studied: $M_z = 450$ G. Using this experimental value, we calculated the demagnetizing factor N for the CoNi(P) alloy synthesized in porous silicon. Calculated by formula (1) under a natural assumption that $N_x = N_y = N \neq N_z$, this value has proved to be close to 2π, that is, to the demagnetizing factor of the ideal ferromagnetic cylinder (see the inset in Fig. 3). This result indicates that a CoNi(P) alloy synthesized in por-Si represents an ensemble of well-defined ferromagnetic filaments possessing a cylindrical shape. Using specially prepared films of the same CoNi(P) composition, we have measured the spin wave resonance (SWR) spectrum for the field **H** perpendicular to the film plane and, using standard formulas [8], calculated the exchange coupling constant: $A = 0.3 \times 10^{-6}$ erg/cm.

The characteristics of the magnetic anisotropy and magnetic microstructure of CoNi(P) alloys with different morphologies were studied by methods described in [6, 9, 10]. Following an approach developed in these papers, we measured the curves of magnetization to saturation and analyzed their shapes, mostly for the external field oriented parallel to the easy axis of a sample (in order to exclude the influence of the form factor).

The magnetization approach to saturation in the CoNi(P) alloy film deposited onto a silicon plate obeys the law $M \sim H^{-2}$ (Fig. 4). This behavior is characteristic of polycrystalline magnetic materials, which allowed us to describe the experimental magnetization curve by the Akulov formula [11]

$$\frac{M(H) - M_s}{M_s} = \left(\frac{D^{1/2}H_a}{H}\right)^2, \quad (2)$$

where M_s is the saturation magnetization and H is the magnetic field strength. Using this formula, it is possible to determine the rms fluctuation of the local anisotropic magnetic field: $D^{1/2}H_a = 600$ Oe.

For the CoNi(P) filaments in por-Si, the magnetization approach to saturation in the range from 1 to 5 kOe obeys the law $M \sim H^{-1/2}$ (Fig. 4). This power law is typical of the amorphous and nanocrystalline magnetic materials. Indeed, a necessary condition for this asymptotic behavior is $R_c < \delta = (A/K)^{1/2}$ [6], where R_c is the correlation radius of local anisotropy (in nanocrystalline alloys, $2R_c$ approximately equals the grain size) and $\delta = 200$–400 Å (in magnetic alloys of $3d$ metals). According to this estimate, the grain size of a CoNi(P) alloy in the synthesized magnetic filaments does not exceed a few hundred Ångströms and, hence, the material occurs in a nanocrystalline state. Since the filament diameter equals the pore diameter and amounts to $1-2$ µm, which is much greater than the grain size, the $M(H)$ data suggest that ferromagnetic filaments in the linear cylindrical pores of por-Si represent a three-dimensional package of nanodimensional grains. Indeed, according to [10], the magnetization of a three-dimensional system of exchange-coupled grains must approach saturation according to the law $M \sim H^{-1/2}$, precisely as is observed in experiment.

Describing the magnetization approach to saturation by the formula [6]

$$\frac{M(H) - M_s}{M_s} = \left(\frac{D^{1/2} \langle H_a \rangle}{H} \right)^{1/2}, \qquad (3)$$

we can determine $D^{1/2}\langle H_a \rangle$, the rms fluctuation of the local anisotropic magnetic field of a block of exchange-coupled nanocrystalline grains. For the CoNi(P) alloy studied, this value has proved to be $D^{1/2}\langle H_a \rangle = 64$ Oe. This parameter characterizes the magnetic microstructure of the nanocrystalline alloy and can be used to estimate the size of a homogeneous magnetization region (magnetic block) in the filaments by the formula $R_f = (2A/D^{1/2}\langle H_a \rangle M)^{1/2}$ [6]. Using the exchange coupling constant of the CoNi(P) alloy determined from the SWR data, we obtain an estimate of $R_f = 460$ Å. This vale is much smaller than the magnetic filament diameter (~1 µm).

Thus, we have established that the synthesized CoNi(PO) alloys of the same composition but different morphologies (a film on single crystal silicon substrate versus filaments in por-Si) are characterized by different laws of the magnetization approach to saturation. This is explained by different degrees of defectness of the material structure. The ferromagnetic filaments in por-Si are characterized by a correlation radius of local anisotropy (R_c) on the order of a few hundred Ångströms, while the film material has R_c at least one order of magnitude greater and, hence, occurs in a state characterized by a much lower degree of nonequilibrium.
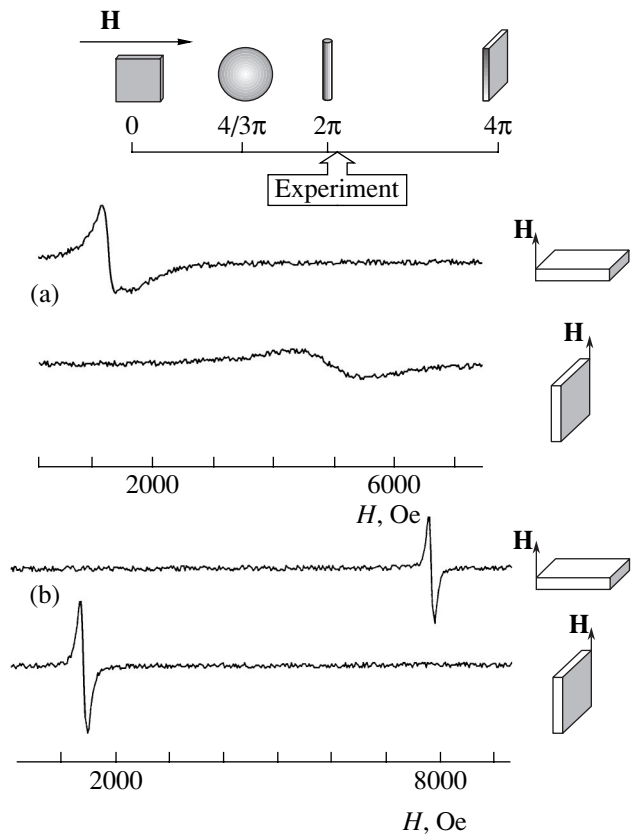
Fig. 3. FMR spectra of a CoNi(P) alloy in the form of (a) ferromagnetic filaments in a por-Si matrix and (b) a film on single crystal silicon substrate measured in various geometries.
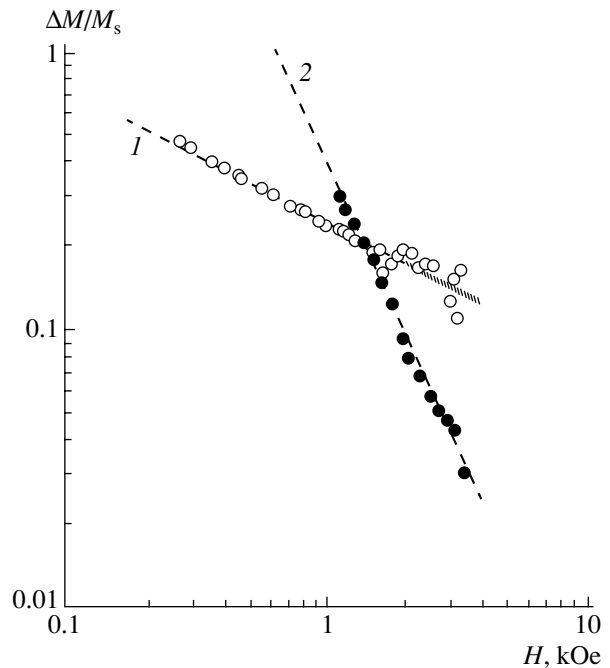

Fig. 4. The curves of magnetization to saturation (plotted in logarithmic coordinates) for a CoNi(P) alloy in the form of (*1*) ferromagnetic filaments in a por-Si matrix and (*2*) a film on single crystal silicon substrate.

In conclusion, note that the obtained composite medium, comprising ferromagnetic filaments in the linear pores of por-Si, must exhibit a specific response to the applied magnetic field. The results of investigation of the electrical and galvanomagnetic properties of this material is the subject for a separate publication.

REFERENCES

1. S. A. Gusev, N. A. Korotkova, D. B. Rozenshteĭn, *et al.*, Pis'ma Zh. Tekh. Fiz. **20** (11), 50 (1994) [Tech. Phys. Lett. **20**, 450 (1994)].

2. A. Fert and L. Piraux, J. Magn. Magn. Mater. **200**, 338 (1999).

3. D. J. Sellmyer, M. Zheng, and R. Skomski, J. Phys.: Condens. Matter **13**, R433 (2001); M. Zheng, R. Skomski, Y. Liu, *et al.*, J. Phys.: Condens. Matter **12**, L497 (2000).

4. J. P. Perez, V. Dupius, J. Tuailon, *et al.*, J. Magn. Magn. Mater. **145**, 74 (1995).

5. J. F. Löffler, J. P. Meier, B. Doudin, *et al.*, Phys. Rev. B **57**, 2915 (1998).

6. R. S. Iskhakov, S. V. Komogortsev, Zh. M. Moroz, *et al.*, Pis'ma Zh. Éksp. Teor. Fiz. **72**, 872 (2000) [JETP Lett. **72**, 603 (2000)].

7. R. S. Iskhakov, S. V. Komogortsev, A. D. Balaev, *et al.*, Pis'ma Zh. Tekh. Fiz. **28** (17), 37 (2002) [Tech. Phys. Lett. **28**, 725 (2002)].

8. C. Kittel, in *Ferromagnetic Resonance* (Inostrannaya Literatura, Moscow, 1962).

9. V. A. Ignatchenko, R. S. Iskhakov, and G. V. Popov, Zh. Éksp. Teor. Fiz. **82**, 1518 (1982) [Sov. Phys. JETP **55**, 878 (1982)].

10. V. A. Ignatchenko and R. S. Iskhakov, Fiz. Met. Metalloved. **6**, 75 (1992).

11. N. S. Akulov, Z. Phys. **69**, 278 (1931).

Translated by P. Pozdeev

Laser Cavity Switching Matched with Target Fracture

P. Yu. Kikin, A. I. Pchelintsev, and E. E. Rusin

Nizhni Novgorod Branch, Blagonravov Institute of Engineering Science, Russian Academy of Sciences,
Nizhni Novgorod, Russia

Abstract—The scheme of a single-laser source capable of switching from free lasing to modulated Q mode synchronously with the target fracture is described. This scheme has good prospects for optimization of the laser processing of thin sheet materials. © *2003 MAIK "Nauka/Interperiodica".*

Experimental investigations aimed at increasing the efficiency of laser processing have shown the advantages of irradiating targets with laser pulses of complicated temporal structure. In the simplest case, laser action should represent a time-correlated (synchronized) combination of pulses generated in the free and modulated Q modes [1, 2]. In the stage of irradiation with a free lasing signal, the target material in the laser action zone is predominantly heated and melted, while the action of a high-intensity (giant) pulse leads to ejection of the condensed phase caused by significantly increased vapor pressure in the channel. Estimates have shown that effective ejection of the melt by a single giant pulse takes place provided that the vapor pressure in the channel is on the order of $P = 10^5$ atm. For the melt removal by small portions, it is sufficient to use a rather short sequence of regular pulses of moderate intensity ensuring a lower excess vapor pressure of $P = 10^4$ atm (which can be provided by using passive Q switching schemes based on LiF crystals).

In the experiments cited above, the combined laser action scheme was implemented using time-correlated and spatially matched pulses of two independent lasers. One of these operated in a quasistationary lasing mode, and the other, in a modulated Q mode. However, gaining the advantages of the aforementioned combined scheme was hindered by problems encountered in practical realization of this two-laser scheme, mostly by difficulties in temporal synchronization and spatial optical matching of laser beams in the focal spot on the target surface.

Here we describe an alternative, nontraditional variant of solving the above problems. This is achieved by using a single laser source with a complex resonator system capable of switching the laser mode in a regime synchronized with stages of the target fracture.

The scheme of the experiment is outlined in Fig. 1. In contrast to the traditional schemes of laser processing, including yttrium aluminum garnet based laser *1*, mirrors *2* and *3* with the reflection coefficients $R = 100$ and 40%, respectively, and focusing lens *4* with a target *5*

placed in the focus, the proposed scheme includes an additional resonator stage comprising lens *6* confocal with the first focusing lens *4*, a passive modulator *7* based on LiF crystal, and mirror *8* with $R = 100\%$.

The first stage of laser action, involving the target heating, melting, and a partial formation of the channel (typical of the free lasing mode), lasts until the formation of an optical channel (through hole) turning on the additional resonator stage. The laser switches to the modulated Q mode to yield a sequence of regular pulses with a single pulse width of 100 ns and repetition period of 10 μs (Fig. 2).

Figure 2 shows an oscillogram of the laser signal illustrating the interaction of laser radiation with a target. In the initial stage, the additional resonator is
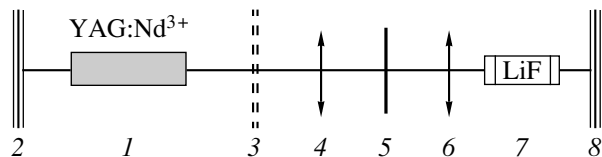

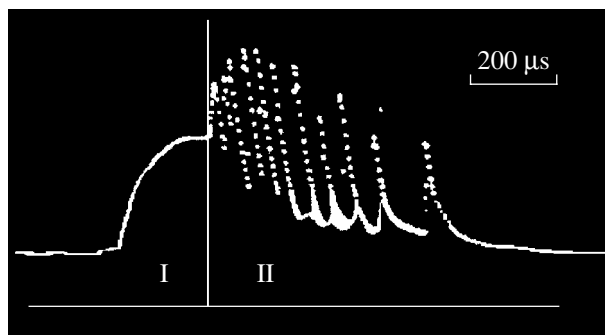**Fig. 1.** A schematic diagram of the experiment (see the text for explanations).

Fig. 2. Oscillogram of the output laser signal showing the stages of operation in the (I) free lasing and (II) modulated Q modes.

blocked by target *5*. This corresponds to a relatively smooth portion I of the laser signal intensity, which is characteristic of the free lasing mode. In this stage, the condensed phase is not effectively removed from the zone of laser action. Beginning with the moment of hole formation in the target, the additional resonator stage starts operating and the laser switches to the regime of producing regular intense pulses. This provides for the intense evaporation of the melt and favors effective removal of the melt by small portions from the laser spot.

REFERENCES

1. N. A. Gippius, Yu. K. Danileĭko, P. V. Ionov, *et al.*, Dokl. Akad. Nauk SSSR **308**, 1122 (1989) [Sov. Phys. Dokl. **34**, 930 (1989)].

2. A. A. Deev, P. Yu. Kikin, and A. I. Pchelintsev, Pis'ma Zh. Tekh. Fiz. **18** (6), 68 (1992) [Sov. Tech. Phys. Lett. **18**, 195 (1992)].

Translated by P. Pozdeev

A Model of the Turbulence Development in the Upper Atmosphere

Yu. N. Zaĭko

Volga Region Academy of State Service, Saratov, Russia

Received October 28, 2002

Abstract—The appearance of quasiperiodic solutions of the Korteweg–de Vries equation, describing waves in the upper atmosphere within the framework of the Freeman–Johnson model, is considered. Evolution of these quasiperiodic solutions can lead to stochastization according to the Ruel–Tackens–Newhouse scenario. Increasing reflection of solar radiation from a turbulent atmosphere influences the entropy balance of the Earth considered as an open system. © 2003 MAIK "Nauka/Interperiodica".

Problems pertaining to the phenomenon of turbulence development in atmospheric flows are of interest for several reasons. First, this phenomenon is a factor directly influencing the weather and the entire character of climate both in separate regions and on the global scale. The task of weather monitoring, especially in predicting catastrophes (whirlwinds, tornado, hurricanes, etc.), is of a federal significance related to the state policy in economics, ecology, etc. [1]. Second, this phenomenon also directly influences the entropy exchange between the Earth and Cosmos, that is, relates to the conditions of stable existence of the Earth as an open system. Indeed, it is now commonly accepted that the export of entropy from the Earth, which amounts to $dS/dt = -6 \times 10^{14}$ W/K as accounted by the absorption of radiation from the Sun (possessing a surface temperature of $T_1 = 5770$ K) and emission from the Earth's surface (at $T_2 = 257$ K, which is the average temperature determined with allowance for reflection from the stratosphere [2]), compensates for an average entropy production density of 10^{-3}–10^{-4} W/(K m^3) in the lower atmosphere. The process of atmosphere turbulization, leading to an additional reflection of solar radiation, can violate the balance by decreasing the export of entropy.

This paper considers the transition to turbulence within the framework of the Freeman–Johnson atmosphere model [3]. According to this model, the atmosphere represents a gas layer with the density ρ and the thickness h. The system is described by the Euler equations for a compressible nonviscous fluid with the corresponding boundary conditions at the free surface and the Earth surface represented by the plane $y' = 0$. Let us introduce the normalized coordinates and velocities

defined as

$$x = \frac{x'}{L}, \quad y = \frac{y'}{h}, \quad t = \frac{Vt'}{L}; \quad u = \frac{u'}{V},$$

$$v = \frac{v'}{V}\delta, \quad p = \frac{p'}{\rho V^2};$$

$$V = \sqrt{gh}, \quad \delta = \frac{h}{L} \ll 1, \tag{1}$$

where x', y', and t' are the nonnormalized horizontal and vertical coordinates and the time, respectively; u' and v' are nonnormalized horizontal and vertical velocity components of the gas per unit volume; L is a characteristic horizontal scale (we assume $L \ll R$, where R is the Earth's average radius, which reduces the problem to a planar case); g is the acceleration of gravity; p' and p are the nonnormalized and normalized pressures, respectively; and V is the velocity of long gravitational waves on the free surface of the gas layer.

Using the multiscale perturbation theory, the initial Euler equation can be reduced to the so-called Korteweg–de Vries (KdV) equation for the variable $\eta = y - 1$ (deviation of the atmosphere boundary from the constant level of $y = 1$) [3]

$$\alpha\eta_{\bar{t}} + \beta\eta\eta_{\bar{x}} + \gamma\eta_{\bar{x}\bar{x}\bar{x}} = 0, \quad \bar{t} = \varepsilon t,$$

$$\bar{x} = x - ct, \quad \bar{y} = y; \quad \delta^2 = K\varepsilon \tag{2}$$

(where K is a constant factor) with a boundary condition for the velocity c of the longwave perturbations:

$$I_2(l) = 1;$$

$$I_n(y) = \int_0^y \frac{d\bar{y}}{[U(\bar{y}) - c]^n}, \quad n = 1, 2, \ldots. \tag{3}$$
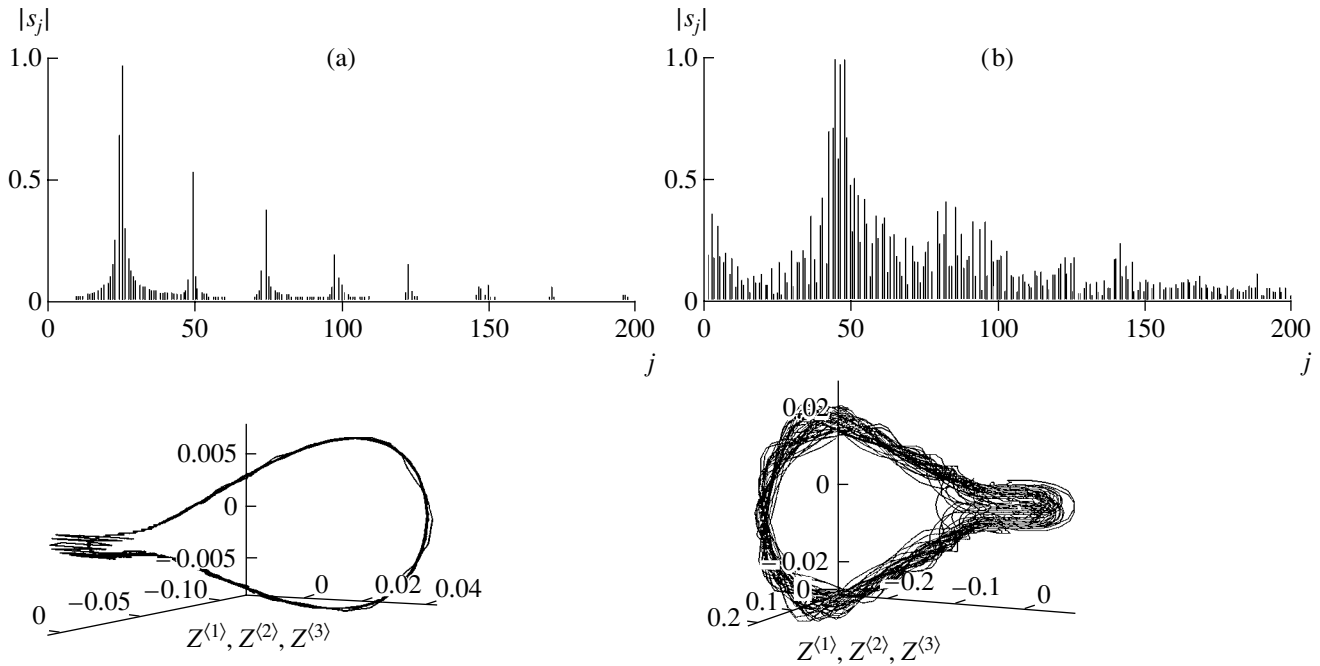
The results of the numerical analysis of Eq. (5) showing the spectrum of solutions calculated by the fast Fourier transform method, $s_j = \mathrm{fft}(\psi_{1i})$ ($0 \le i \le 4096$, $0 \le j \le 2048$) and the corresponding phase portraits ($Z^{\langle 1 \rangle} = \psi_1$, $Z^{\langle 2 \rangle} = \psi_2$, $Z^{\langle 3 \rangle} = \psi_1'$) on the interval $0 \le x \le 2580$ for the initial conditions $\psi_1 = \psi_2 = 0.01$, $\psi_1' = \psi_2' = 0.001$, and (a) $\Gamma_1 = 1.5$, $\Gamma_2 = 4.95$, $\nu = 0.792$ and (b) $\Gamma_1 = 1.5$, $\Gamma_2 = 0.95$, $\nu = 0.792$.

Here, $U(y)$ is the unperturbed profile of the horizontal velocity component $u(x, y) = U(y) + \varepsilon \bar{u}(x, y)$; the expressions for α, β, and γ as functionals of $U(y)$ were obtained in [3], where Eq. (2) was analyzed for some approximate solutions of the dispersion equation (3).

Below, we will study quasiperiodic solutions of the KdV equation (2), the appearance of which precedes the development of dynamic chaos in the system considered within the framework of the Ruel–Tackens–Newhouse model [4]. An important premise for this study is the existence of multiple roots of Eq. (3). A condition for the appearance of such roots is $dI_2(l)/dc = 0$. As can be readily seen, this condition can be satisfied by defining $U(y)$, for example, in the form of a piecewise linear function.

The appearance of multiple roots of Eq. (3) precedes the appearance of complex conjugate roots $c = c_1 + ic_2$. It should be recalled that c is the velocity of the system of reference (longwave perturbations of small amplitude) in which Eq. (2) is valid. Physically, the condition $c_2 \ne 0$ implies the appearance of a nontransmitting band in the corresponding linear problem. In the nonlinear case, this leads to the appearance of quasiperiodic solutions [5]. In order to demonstrate this, let us use the Galilean transformation to pass to a frame in which $c =$

c_1, whereby Eq. (2) converts into

$$\psi_{\tilde{t}} + i \nu \psi_{\tilde{x}} + \psi \psi_{\tilde{x}} + \tilde{\gamma} \psi_{\tilde{x}\tilde{x}\tilde{x}} = 0;$$

$$\psi = \frac{\beta}{\alpha}\eta, \quad \nu = \frac{c_2}{\varepsilon}, \quad \tilde{\gamma} = \frac{\gamma}{\alpha}, \quad \tilde{t} = \bar{t}, \quad \tilde{x} = \bar{x} + i\nu\bar{t}; \tag{4}$$

$$\alpha = \frac{1}{W_1} + \int_0^1 \frac{(WI_2)'}{W^2}d\bar{y}; \quad \gamma = -K\int_0^1\int_{\bar{y}}^1\int_0^y \frac{W^2(\bar{y}')}{W^2(\bar{y})W^2(\bar{y}'')}d\bar{y}d\bar{y}'d\bar{y}'';$$

$$W(\bar{y}) = U(\bar{y}) - c, \quad W_1 = W(l),$$

where expressions for α and γ are taken from [2]. Note that, in the general case, $\tilde{\gamma} = \Gamma_1 + i\Gamma_2$ is a complex quantity. Now let us rewrite Eq. (4) by omitting tildas at x and t, putting $\psi = \psi_1 + i\psi_2$, and substituting $x \longrightarrow x(\Gamma_1^2 + \Gamma_2^2)^{1/2}$. After single integration with respect to x, we obtain the system of equations

$$\psi_{1xx} = \nu(\Gamma_1\psi_2 - \Gamma_2\psi_1) + \frac{1}{2}\Gamma_1(\psi_2^2 - \psi_1^2) - \Gamma_2\psi_1\psi_2,$$

$$\psi_{2xx} = -\nu(\Gamma_2\psi_2 + \Gamma_1\psi_1) - \frac{1}{2}\Gamma_2(\psi_2^2 - \psi_1^2) - \Gamma_1\psi_1\psi_2. \tag{5}$$

The solutions of this equation for various ν and $\Gamma_{1,2}$ values are presented in the figure. Using the phase por-

trait and the spectrum of solutions, it is easy to trace the appearance of a quasiperiodic solution and the initial stage of its breakage leading to stochastization of the solutions of Eq. (2) by analogy with other problems [6].

REFERENCES

1. L. Daniel, http://www.legislative.noaa.gov/Testimony/03140/albritton.html.

2. V. Ebeling, A. Engel, and R. Faistel, *The Physics of Evolution Processes: Synergistic Approach* (Editorial URSS, Moscow, 2001).

3. N. C. Freeman and R. S. Johnson, J. Fluid Mech. **42**, 401 (1970).

4. A. Lichtenberg and M. Liberman, *Regular and Stochastic Motion* (Springer, Heidelberg, 1982; Mir, Moscow, 1984).

5. Yu. N. Zaĭko, Pis'ma Zh. Tekh. Fiz. **28** (6), 42 (2002) [Tech. Phys. Lett. **28**, 235 (2002)].

6. Yu. N. Zayko and I. S. Nefedov, Appl. Math. Lett. **14**, 115 (2001).

Translated by P. Pozdeev

Diffraction of Electromagnetic Waves on Two Spheres: Application to Designing Antennas for Space Vehicles

I. P. Kozlov

Moscow State Aviation Institute (Technical University), Moscow, Russia
Received September 20, 2002

Abstract—Designing the antenna systems for space vehicles employing electrojet thrusters has to be based on a strict solution of the problem of electromagnetic wave diffraction on two bodies. Here, the problem of diffraction on two spherical surfaces is strictly solved in terms of the scalar field potentials. A method for the transformation of wave amplitudes upon a shift of the spherical coordinate system is proposed. The results of numerical calculations are presented. © 2003 MAIK "Nauka/Interperiodica".

Introduction. Designing radio antennas operating in the microwave range for space vehicles frequently involves significant limitations with respect to position, weight, dimensions, and some other technical parameters and, hence, encounters considerable technical difficulties. Especially big problems are caused by closely located protruding structures and by inhomogeneous cold plasma (for example, that of a jet thruster) with a critical density. According to the method of mathematical modeling applicable in the first stage of designing antennas for space vehicles [1], the optimum system is selected based on a strict solution of the problem of electromagnetic wave diffraction on two bodies. These objects can represent an ideally conducting disk with hemispheres (modeling antennas and a space vehicle body) or an inhomogeneous dielectric ball (modeling a plasma jet). Using such an electrodynamic two-body model, it is possible to take into account the mutual influence of antennas and the interaction of electromagnetic waves with the space vehicle body and its protruding structures (including sharp edges) in the presence of the thruster plasma jet. Methods developed for strictly solving the problem of electromagnetic wave diffraction on two bodies, based on the separation of variables in spherical coordinates, and the corresponding methods of numerical calculations allow the computations to be conducted for the characteristic system dimensions up to several wavelengths [1, 2].

The importance of these investigations increases in view of the qualitative and quantitative dependence of the solution on the small variation of parameters, predicted for the problem of the electromagnetic wave propagation in a plane-layered dielectric with extremely small absorption near the zero of ε [3, 4]. Moreover, the nonlinear phenomena possible at $\varepsilon \approx 0$ require a special analysis. In connection with this, the mathematical modeling of the interaction of electromagnetic waves with a cold plasma possessing a nearly critical density (corresponding to zero ε) has to be based on a strict solution of the problem of electromagnetic wave diffraction on two bodies.

The plasma stream of an electrojet thruster is modeled by two homogeneous dielectric balls, embedded into one another, with nonintersecting spherical surfaces the centers of which are shifted along the symmetry axis (Fig. 1). The results presented below show that the proposed mathematical apparatus offers an effective tool for designing antennas of space vehicles.

Fig. 1. The model of a space vehicle with plasma formation.

Using the two-body model, it is possible to study the physical phenomena related to electromagnetic compatibility of the radio equipment of space vehicles in the presence of an inhomogeneous plasma with a nearly critical density.

Method of the wave amplitude transformation upon a shift of the coordinate system. Solutions of the Maxwell equations, obtained by separating variables in a spherical coordinate system, can be represented in terms of the scalar potentials

$$V = \sum_{m=0}^{\infty} \sum_{n=1}^{\infty} \left\{ \frac{\bar{A}_{nm}}{\bar{C}_{nm}} \cos(m\varphi) + \frac{\bar{B}_{nm}}{\bar{D}_{nm}} \sin(m\varphi) \right\}$$
$$\times P_n^m(\cos\theta) \frac{\zeta_n^{(1)}(\rho)}{\Psi_n(\rho)}, \quad r \gtrless r' \qquad (1)$$

of the magnetic waves ($E_r = 0$) and by analogous expressions for the potentials U of the electric waves ($H_r = 0$) (obtained by eliminating bars over the wave amplitudes). Here, $\rho = \sqrt{\varepsilon\mu}\, kr$, r' is the radius of the region occupied by sources, $k = 2\pi/\lambda$, λ is the wavelength in free space, and ε and μ are the permittivity and permeability of the homogeneous medium.

In the local spherical coordinate systems (Fig. 2) centered at O_s ($s = \pm 1$), the components of the electric field E (and, similarly, of the magnetic field H) are related by the formulas

$$r_s E_{r_s} = (r_{-s} + sl\cos\theta_{-s}) E_{r_{-s}} - sl\sin\theta_{-s} E_{\theta_{-s}}, \qquad (2)$$

where l is the distance between centers O_s and O_{-s}. Taking into account orthogonality of the eigenfunctions, we obtain the following expressions describing the transformation of the wave amplitudes in a homogeneous medium [5]:

$$\frac{C_{nm}^n}{\bar{D}_{nm}^s} = \sum_j \left\{ \alpha_{nmj}^{-s} \frac{A_{jm}^{-s}}{\bar{B}_{jm}^{-s}} + \frac{I}{w_i} \bar{\alpha}_{nmj}^{-s} \frac{\bar{B}_{jm}^{-s}}{-A_{jm}^{-s}} \right\} \quad \text{at} \quad r_s < l, \quad (3)$$

where $n, m = 0, 1, 2, \dots$ ($n \neq 0$, $m \leq n$); $w_j = \sqrt{\mu_j/\varepsilon_j}$; and the coefficients α_{nmj}^{-s} and $\bar{\alpha}_{nmj}^{-s}$ (determined by the coordinates of the new origin in the old coordinate system) depend on the kl distance, for example, $\alpha_{nmj}^{-s} = f(kl, -s, n, m, j)$. Expressions (3) show that, on the passage from one to another local system of coordinates, waves of one type give rise to waves of both types. Thus, the wave amplitude transformations (3) reveal a mutual relation between the electric and magnetic waves with respect to a shift of the origin of coordinates. This result demonstrates the incorrectness of replacing a superposition of fields with the superposition of scalar poten-
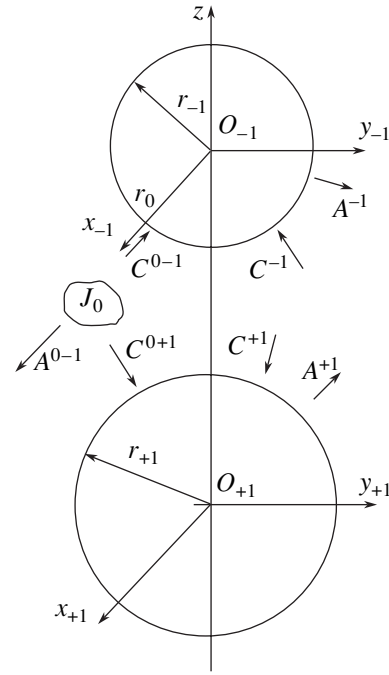
Fig. 2. A model describing the diffraction of electromagnetic waves on two bodies. The amplitudes of incident electric and magnetic waves (C_{nm}^s, $\bar{D}_{nm}^s$) are denoted by C^s; the reflected waves (A_{nm}^s, $\bar{B}_{nm}^s$) are denoted by A^s ($s = \pm 1$).

tials (as it was made in [6] in solving the problem of diffraction on two balls) [5].

Now let us consider an axisymmetric system of bodies in which the wave amplitudes for various azimuthal harmonics are independent. Therefore, the solution can be presented for an arbitrary m (for brevity, expressions are written for the electric and magnetic wave harmonics of the $\cos m\varphi$ and $\sin m\varphi$ types, respectively).

Electromagnetic wave diffraction on two bodies. Consider the diffraction of electromagnetic waves on two spheres in vacuum (Fig. 2). Each body is related to its own system of coordinates centered at O_s ($s = \pm 1$) and bears a coordinate surface of radius r_s (the two spheres with the radii r_s do not intersect with each other). Let the field in the common region near r_s be determined by the wave amplitudes of the external currents (A_{nm}^{Os}, $\bar{B}_{nm}^{Os}$, C_{nm}^{Os}, $\bar{D}_{nm}^{Os}$) and by the unknown amplitudes of waves (A_{nm}^s, $\bar{B}_{nm}^s$, C_{nm}^s, and $\bar{D}_{nm}^s$) caused by the mutual influence of the two bodies. If the boundary conditions of continuity of the tangential field components on the surface of each body are satisfied, a solution of the diffraction problem for the wave amplitudes is determined by the relations

$$A_{nm}^s = a_{sn}(C_{nm}^s + C_{nm}^{Os}), \quad \bar{B}_{nm}^s = b_{sn}(\bar{D}_{nm}^s + \bar{D}_{nm}^{Os}), \quad (4)$$
$$s = \pm 1, \quad n = 1, 2, 3, \dots,$$

where the coefficients are expressed through the eigenfunctions; for example, a_{1n} and b_{1n} values for an ideally conducting sphere are as follows:

$$a_{1n} = -\frac{\psi_n'(kr_1)}{\zeta_n^{(1)'}(kr_1)}, \quad b_{1n} = -\frac{\psi_n(kr_1)}{\zeta_n^{(1)}(kr_1)}.$$

In the common region between spheres, the fields in the vicinity of surfaces with the radii r_s ($s = \pm1$) are determined by the scalar potentials (1) of the electric and magnetic waves:

$$U_s = U(A_{nm}^s, C_{nm}^{Os} + C_{nm}^s),$$

$$V_s = V(\bar{B}_{nm}^s, \bar{D}_{nm}^{Os} + \bar{D}_{nm}^s), \quad s = \pm1.$$

Substituting expressions (3) for the wave amplitude transformation into relations (4), we obtain an infinite system of equations for the unknown wave amplitudes:

$$A_{nm}^s - a_{sn} \sum_{j=m}^{\infty} \{\alpha_{nmj}^{-s} A_{jm}^{-s} + \bar{\alpha}_{nmj}^{-s} \bar{B}_{jm}^{-s}\} = a_{sn} C_{nm}^{Os},$$

$$\bar{B}_{nm}^s - b_{sn} \sum_{j=m}^{\infty} \{\alpha_{nmj}^{-s} \bar{B}_{jm}^{-s} - \bar{\alpha}_{nmj}^{-s} A_{jm}^{-s}\} = b_{sn} \bar{D}_{nm}^{Os}, \tag{5}$$

$$s = \pm1, \quad n = 1, 2, 3, \dots.$$

The solution of the system of equations (5) with respect to A_{nm}^s and $\bar{B}_{nm}^s$ ($s = \pm1$), obtained by the method of truncation, is the solution of the initial problem. The total field in the common region between spheres represents a geometric sum of the fields determined in the local coordinate systems by the amplitudes of these waves and the waves of external currents (e.g., A_{nm}^{O-1}, $\bar{B}_{nm}^{O-1}$). In the far field zone ($r \gg r_s$, $kr \gg 1$), expressions for the fields appear to be much simpler.

Using the method of the wave amplitude transformation described above, a strict solution of the problem of electromagnetic wave diffraction on two balls is constructed as follows. First, the field in the common region near the surface of each ball in the local coordinate system is represented as a sum of the given wave amplitudes of external currents and the unknown wave amplitudes related to the influence of the other ball (Fig. 2). The boundary conditions of continuity on the surface of each ball yield an infinite system of equations for the unknown wave amplitudes. Adding expressions for the transformation of these unknown amplitudes on the passage from one to another local coordinate system makes the total system of equations complete. Solving this system by the method of truncation, we obtain the solution of the initial problem.

If the wave amplitudes $A_{nm}^{s1} \equiv A_{nm}^s$ and $\bar{B}_{nm}^{s1} \equiv \bar{B}_{nm}^s$ are solutions of the system of equations obtained as described above, these amplitudes will not change upon multiply repeated transformation (3), that is, $A_{nm}^{sp} = A_{nm}^{s1}$ and $\bar{B}_{nm}^{sp} = \bar{B}_{nm}^{s1}$ (for $p = 1, 2, 3, \dots$). This property of the wave amplitude transformation can be used for verification of the solution of an infinite system of equations obtained by the truncation method. When an approximate solution of the diffraction problem is known, it can be refined by multiple application of the wave amplitude transformation (3), provided that the iterative process is convergent. Based on such repeated application of the wave amplitude transformation (3), a method has been developed for the calculation of a two-body system with dimensions of up to several wavelengths [1]. This formalized approach significantly simplifies the process of designing microwave antennas for space vehicles.

Excitation of two spheres by a turnstile antenna. The problem of two spheres excited by the radiation of a turnstile antenna reduces to the problem presented by Eqs. (5) with C_{nm}^{O-1} and $\bar{D}_{nm}^{O-1}$ given for $m = 1$. The total field in the far zone represents a sum of the primary field of external currents with the wave amplitudes A_{nm}^{O-1} and $\bar{B}_{nm}^{O-1}$ and the field of the waves reflected from the sphere, determined by the wave amplitudes A_{nm}^s and $\bar{B}_{nm}^s$ ($s = \pm1$) via standard formulas (1) for the scalar potentials U and V.

As an example, the problem of excitation of an ideally conducting sphere with $kr_{-1} = 4$ by a turnstile antenna in the presence of another conducting sphere of variable radius was numerically solved using a computational program written in FORTRAN. The turnstile antenna parameters were as follows: $kz_0 = 4.8$, $f_0 = 30°$, and $kl_0 = 0.8$ (z_0 is the distance from 0_{-1} center to the antenna mount point along the z axis, f_0 is the antenna dipole sloping angle relative to the positive z axis direction, and l_0 is the length of the dipole with a sinusoidal current). Figure 3 shows the antenna directivity patterns observed for the excitation of a lone sphere (curve *1*), lone hemisphere (curve *2*), and two spheres. As can be seen, all patterns have similar shapes. This result implies that neither the shape of the spherical antenna in the shadowed zone nor the presence of another body influence the directivity pattern to any significant extent.

Excitation of a sphere by a ring slot in the presence of an inhomogeneous ball. Using an axisymmetric system of two bodies, it is possible to model a space vehicle with an obstacle in the form of an inhomogeneous ball comprising two embedded dielectric balls with displaced centers (such an inhomogeneous ball can model the plasma stream of an electrojet thruster, see Fig. 1). Let an ideally conducting sphere centered at
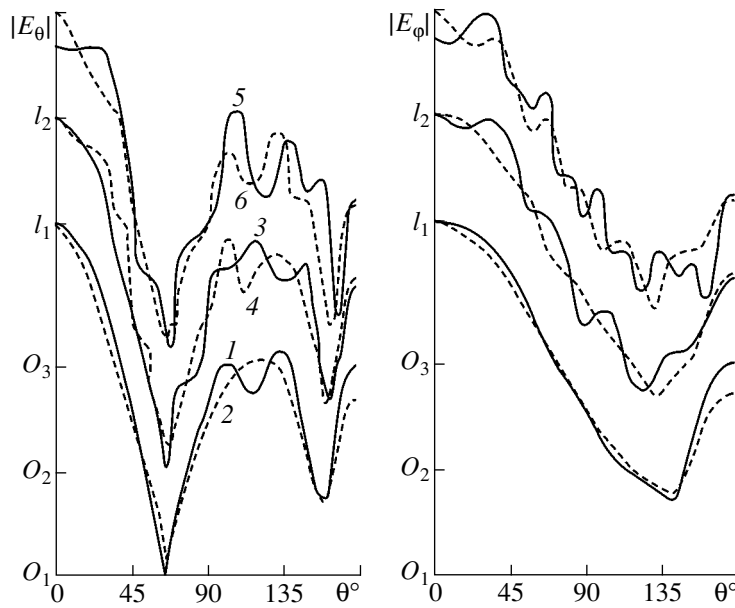
Fig. 3. Directivity patterns of a sphere excited by an antenna with $kr_{-1} = 4$, $kz_0 = 4.8$, $f_0 = 30°$, and $kl_0 = 0.8$ in the presence of another sphere, calculated for various radii and positions of this sphere (curve *2* refers to a lone hemisphere with $kr_{-1} = 4$): (*1*) $kr_{+1} = 0$ (lone sphere); (*3*) $kr_{+1} = 4$, $kl = 10$; (*4*) $kr_{+1} = 2$, $kl = 10$; (*5*) $kr_{+1} = 8$, $kl = 14$; (*6*) $kr_{+1} = 4$, $kl = 14$.
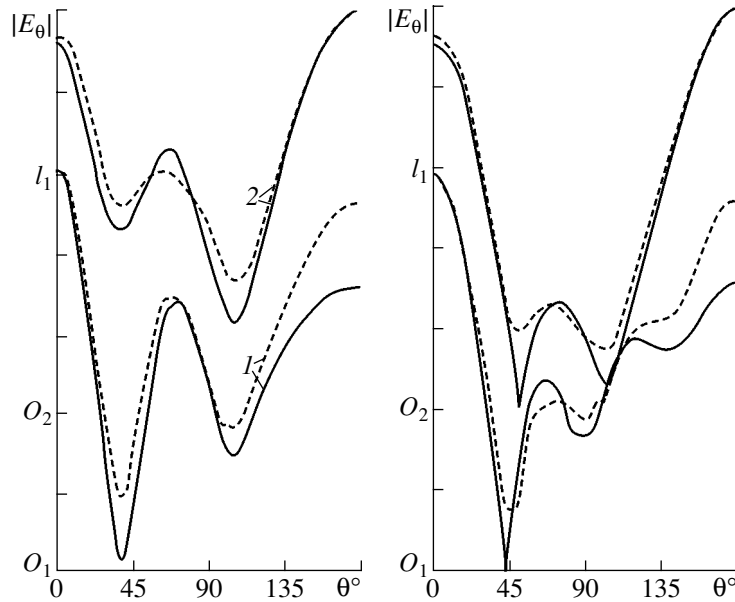

Fig. 4. Directivity patterns of a spherical antenna ($kr_{-1} = 1$, $kr_0 = 1$) affected by the presence of a closely spaced inhomogeneous dielectric ball, as calculated for $kr_{+1} = 2$, $\varepsilon_1 = 4$, $\varepsilon_2 = 8$, $kl = 4$, $kd = 0.5$, and $kr_2 = 0.5$ (*1*) and 1.5 (*2*).

O_{-1} bear an external ring-shaped magnetic current ($kr_0 = 1$, $\theta_0 \geq 90°$) expressed as $e^{-i\varphi}$. A strict solution of the problem for a lone inhomogeneous ball centered at O_{+1} was obtained in [2]. A strict solution of the problem of excitation of two bodies, the other representing a homogeneous ball centered at O_{+1}, is determined by a system of type (5) with preset external currents for $m = 1$. In the general case, the calculation for a system comprising a spherical antenna and an inhomogeneous ball can be performed using an iterative method of transreflections [1]. Figure 4 presents the directivity patterns calculated in this case. Here, solid curves show the results of calculations based on a strict solution of the diffraction problem, while the dashed curves represent the approximate results obtained with neglect of the mutual influence of two bodies.

The results of our investigations for a sphere ($kr_{-1} = 1$) excited in the presence of a ball showed that the results of calculations based on the strict and approximate solutions coincide for distances from the ball exceeding one and a half wavelengths. The accuracy of calculations provided by the strict solution is quite sufficient in the first stage of designing antennas for space vehicles. Using the proposed method, it is possible to perform calculations for a system of two balls with radii up to about one wavelength.

Conclusion. A method for investigation of the diffraction of electromagnetic waves on two bodies described by spherical coordinates is developed. Use of this method is expedient for designing antennas of space vehicles with allowance of the presence of plasma bodies. The mutual influence of the waves of two types, with allowance of the diffraction on two bodies, detrimentally influences the polarization decoupling of receiving and transmitting antennas. The problem of electromagnetic compatibility is complicated by the probability of nonlinear phenomena. The experimental data reported in [7] show evidence of a sharp increase in the microwave noise level of electrojet thrusters operating at a maximum output power level (this factor additionally complicates the problem). The method developed above will be employed in subsequent investigations aimed at solving electromagnetic compatibility problems.

REFERENCES

1. I. P. Kozlov, *Proceedings of the 26th International Electric Propulsion Congress (IEPC-99), Kitakyushu, Japan, 1999*, p. 229.
2. I. P. Kozlov, Radiotekh. Élektron. (Moscow) **46** (2), 180 (2001).
3. I. P. Kozlov, Pis'ma Zh. Tekh. Fiz. **26** (14), 28 (2000) [Tech. Phys. Lett. **26**, 605 (2000)].
4. I. P. Kozlov, Radiotekh. Élektron. (Moscow) **42** (2), 142 (1997).
5. I. P. Kozlov, Izv. Vyssh. Uchebn. Zaved., Radiofiz. **18**, 997 (1975).
6. E. A. Ivanov, *Diffraction of Electromagnetic Waves on Two Bodies* (Nauka i Tekhnika, Minsk, 1968).
7. V. I. Brukhty and K. P. Kirdyashev, Pis'ma Zh. Tekh. Fiz. **26** (14), 42 (2000) [Tech. Phys. Lett. **26**, 612 (2000)].

Translated by P. Pozdeev

Photonic Bandgap Structures
with Electronically Controlled Characteristics

N. V. Britun* and V. V. Danilov

Kiev National University, Kiev, Ukraine
* e-mail: britun@mail.univ.kiev.ua
Received October 22, 2002

Abstract—Microwave filters based on periodic metallized ferrite–dielectric structures are described. The spectral characteristics of such a photonic bandgap filter can be electronically controlled on a real-time scale. © *2003 MAIK "Nauka/Interperiodica"*.

Introduction. Photonic bandgap (PBG) structures have been extensively investigated since the 1980s. The properties of related synthetic materials (photonic crystals) [1] were studied in both optical and microwave ranges. One of the promising microwave applications of PBG materials are filters based on metallized dielectric structures [2]. Placed in a waveguide, such metallized PBG structures create a periodic distribution of impedance that is equivalent to a metallized "crystal lattice" arranged between conducting walls. Radiation reflected from the "crystallographic planes" of this lattice exhibits interference to form a pattern of transmission and band gaps observed in experiment.

For example, microwave radiation in a waveguide containing periodic matrices of $n \times m$ patchboards composed of metal disks is incident perpendicularly onto [001] planes of a tetragonal lattice created by this PBG structure [2]. The appearance of band gaps in the spectrum of such a PBG filter is explained in terms of the well-known Bragg formula. According to this, in the vicinity of a band gap, a longitudinal period of the crystal lattice accommodates an integer number of half-waves:

$$2d\sin\theta = k\lambda, \quad d = k\frac{\lambda}{2}, \tag{1}$$

where d is the interplanar spacing, k is an integer, λ is the radiation wavelength, and $\theta = 90°$ is the incidence angle.

There is a need for PBG structures admitting real-time electronic control of the amplitude–frequency characteristics. This problem has been mostly studied in the optical range. Figotin *et al.* [3] theoretically studied the possibility of spectral tuning in two-dimensional PBG structures. Recently, Golubev *et al.* [4] reported on an optical filter in which the spectral characteristics can be adjusted by controlling the degree of filling pores in a synthetic opal and switched in a jump-like manner [5] as a result of the temperature-induced

phase transition in the filling material. The problems of creating PBG structures with the optical characteristics controlled on a real-time scale were studied in [6, 7] using synthetic opals in which the pores are filled with nematic liquid crystals. By changing the liquid crystal orientation with the aid of an applied electric field, it is possible to control the density of states of such photonic crystals. The optical properties of PBG with liquid crystals can be also temperature-controlled [8]. Although the real-time control in the PBG structures described in [5–8] is possible, the relative magnitude of changes in parameters of the these systems is still rather small.

Here we report on the results of investigation of the real-time electronic control of the spectral characteristics of microwave PBG structures.

Experimental results. The experiments were performed with PBG structures of two types: (i) $n \times m = 1 \times 2$, 2×4, and 3×6 patchboards composed of metal disks and (ii) narrow metal strips arranged at the center of a rectangular waveguide, perpendicularly to the wide wall. The spaces between metal elements were filled with foamy microwave plastic ($\varepsilon \approx 1$, $\tan\delta \approx 0$), 1-mm-thick Al_2O_3 plates (polycor, $\varepsilon = 9.6$, $\tan\delta \approx 15 \times 10^{-4}$), or 1-mm-thick polycrystalline yttrium iron garnet (YIG) plates matched to the waveguide cross section ($\varepsilon \approx 15$, $\tan\delta \approx 2 \times 10^{-4}$). All experiments were performed with a TE_{10} waveguide mode for a 3-cm waveguide in a frequency range from 7.8 to 12.5 GHz. The metal layer thickness varied from 1 to 20 μm (being at least one order of magnitude greater than the skin layer thickness).

Typical amplitude–frequency characteristics (AFCs) of the microwave filters based on the metallized PBG structures studied, measured in the absence of external control factors, are presented in Figs. 1 and 2a (solid curves *1*). The characteristics were modified by applying a homogeneous magnetic field. In these
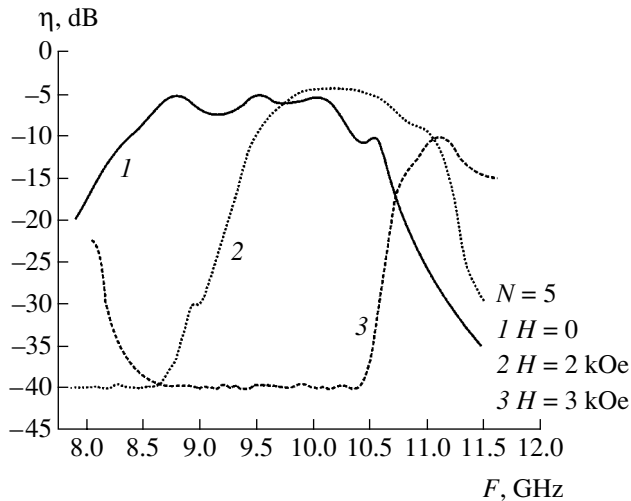
Fig. 1. Magnetic-field-induced variations of the transmission band of a PBG-based microwave filter (N is the number of layers in the PBG structure, H is the applied field strength).
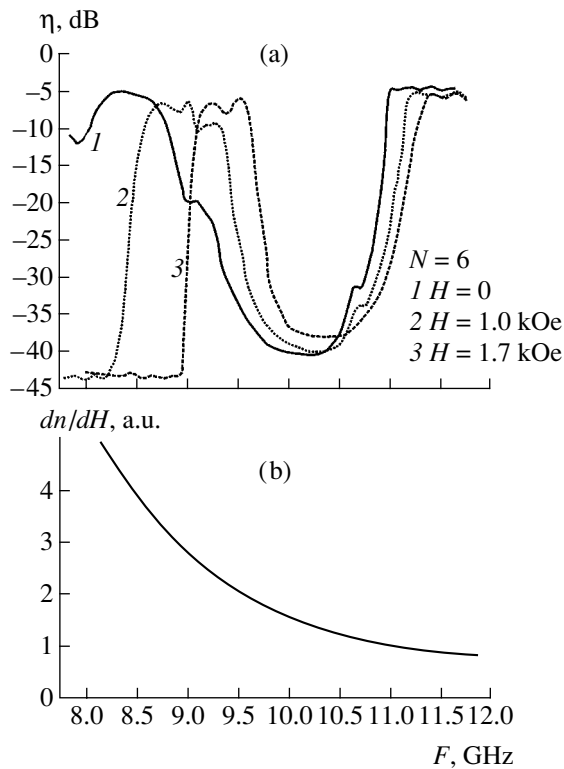

Fig. 2. Amplitude–frequency characteristics of a six-layer PBG filter: (a) variation in the applied magnetic field H; (b) a dispersion curve explaining the observed behavior (different variation rates of the LF and HF fronts).

experiments, the waveguide contained PBG structures with additional YIG plates. Using this ferrite in a biased regime, the transmission band of the microwave filter could be controlled by applying an external field (Fig. 1). The experiment illustrated in Fig. 1 was per-

formed with five layers of metallized 2×4 disk patchboards. Each layer consisted of a disk patchboard, contacting with a YIG plate, and six Al_2O_3 plates. The magnetic field was oriented in the plane of the ferrite plate, perpendicularly to the wide wall of the waveguide.

As an alternative type of metallized element, we used narrow metal strips arranged at the center of the waveguide, perpendicularly to the wide wall (not contacting with the waveguide). As is known, such conducting strips create a periodic distribution of impedance in the waveguide. The central position corresponded to the TE_{10} mode, ensuring the coincidence of the maxima of the electric wave field intensity with the maxima of the impedance and providing for the maximum concentration of electromagnetic field in the ferrite. Using this type of metallized elements reduces the losses for reflection as compared to the system with large disks and significantly simplifies the process of manufacturing filters, especially in cases when etching has to be employed.

Figure 2a presents data illustrating adjustment of the AFC of a microwave filter comprising six layers of 0.5-mm-wide aluminum strips, deposited onto Al_2O_3 plates of the same width, and YIG plates arranged so that the metal occurs between ferrite and polycor. As can be seen from Fig. 2a, the high-frequency (HF) and low-frequency (LF) fronts of the curve shift at different rates in response to the magnetic field. This is explained by features of the complex permeability (χ) dispersion in YIG (see. e.g., [9]). As the magnetic field strength is increased, the real part of the permeability (χ') at a given frequency grows, which leads to increasing field concentration in the ferrite. To the first approximation, the field-induced AFC shift can be calculated using the concept of the optical pathlength in a medium with the refractive index

$$n = \sqrt{\varepsilon\mu}. \qquad (2)$$

As this parameter changes upon application of the magnetic field H, the AFC shifts at a rate of

$$\frac{\partial n}{\partial H} \sim \frac{1}{\sqrt{\mu}}\frac{\partial \mu}{\partial H} \approx \frac{1}{\sqrt{1 + 4\pi\chi'}}\frac{\partial \chi'}{\partial H}. \qquad (3)$$

Figure 2b shows the AFC shift rate calculated by formula (3) and plotted in the same scale as the AFC. The AFC shift rate is normalized to that of the HF front of the band gap (see Fig. 2a), that is, to the value at 11.2 GHz. A comparison of the field-induced AFC shift rates observed for the HF and LF fronts shows good coincidence of the experimental and calculated results. Indeed, the left-hand front of the AFC moves at a rate which is approximately twice that for the right-hand front (for $H \sim 1$ kOe). The absolute AFC shift in the

PBG structure studied amounts on the average to 250 and 125 MHz for the LF and HF fronts, respectively.

The data in Fig. 2a show that, in the general case, a magnetic-field-controlled PBG filter may possess a relatively narrow transmission band (on the order of 0.5 GHz), with a level of losses not exceeding 6 dB and a level of quenching about 40–43 dB. This transmission band can be effectively adjusted by applying a magnetic field in the range from 0 to 2.5 kOe.

Conclusion. The results of our experiments demonstrate the possibility of controlling the amplitude–frequency characteristics of microwave filters based on metallized PBG structures. A new variant of such structures is proposed that significantly simplifies the technology of manufacturing filters, for example, for the millimeter wavelength range. The characteristics and the controllability of filters employing metallized ferrite–dielectric patchboards of various types are essentially the same. Attempts at explaining the mechanism of control in the PBG structures studied showed that features of the field-induced shift of the amplitude–frequency characteristics can be related to peculiarities in the dispersion properties of ferrites employed.

REFERENCES

1. E. Yablonovitch, J. Opt. Soc. Am. B **10**, 283 (1993).

2. C. A. Kuriazidou, H. F. Contopanagos, and N. G. Alexopolos, IEEE Trans. Microwave Theory Techn. **49**, 297 (2001).

3. A. Figotin, Yu. A. Godin, and I. Vitebsky, Phys. Rev. B **57**, 2841 (1998).

4. V. G. Golubev, V. A. Kosobukin, D. A. Kurdyukov, *et al.*, Fiz. Tekh. Poluprovodn. (St. Petersburg) **35**, 710 (2001) [Semiconductors **35**, 680 (2001)].

5. V. G. Golubev, D. A. Kurdyukov, A. V. Pevtsov, *et al.*, Fiz. Tekh. Poluprovodn. (St. Petersburg) **36**, 1122 (2002) [Semiconductors **36**, 1043 (2002)].

6. K. Busch and S. John, Phys. Rev. Lett. **83**, 967 (1999).

7. D. Kang, J. E. Maclennan, N. A. Clark, *et al.*, Phys. Rev. Lett. **86**, 4052 (2001).

8. K. Yoshino, Y. Shimoda, Y. Kawagishi, *et al.*, Appl. Phys. Lett. **75**, 932 (1999).

9. A. G. Gurevich and G. A. Melkov, *Magnetic Oscillations and Waves* (Fizmatlit, Moscow, 1994).

Translated by P. Pozdeev

Peculiarities of the Ge(111)–(2 × 8) Crystal Face Structure Studied by Electron Energy Loss Spectroscopy

N. N. Gorobeĭ, V. E. Korsukov*, A. S. Luk'yanenko,
R. R. Nazarov, and B. A. Obidov
Ioffe Physicotechnical Institute, Russian Academy of Sciences, St. Petersburg, 194021 Russia
* e-mail: Vjacheslav.Korsukov@mail.ioffe.ru
Received October 14, 2002

Abstract—The dispersion of surface plasma oscillations of a Ge(111)–(2 × 8) single crystal face was studied by electron energy loss spectroscopy. The experimental data are indicative of a reduced density in the surface layer, which confirms the existing adatom model of the 2 × 8 surface superstructure. © *2003 MAIK "Nauka/Interperiodica".*

In [1], measurements of electron energy losses on surface plasmons (i.e., the discrete losses related to the quanta of surface plasma oscillations) were originally used to investigate the Al(111) surface. These data were used to determine the thermal expansion coefficient (TEC) and the static relaxation parameter (a change in the mean equilibrium values of the lattice constants) of the surface layer. Then [2], electron energy loss spectroscopy (EELS) was used to determine the rms displacements of atoms—another important parameter of the atomic dynamics—on the same Al(111) crystal face. The parameters of atomic dynamics measured by this alternative technique agreed well with the data obtained by the conventional method of low energy electron diffraction (LEED), while the EELS data on the static relaxation were consistent with theoretical estimates for the metal surfaces [3].

Later [4], the EELS technique was used for the first time to determine the TEC of a Ge(111)–(2 × 8) surface. Below we report on the use of EELS to determine the structure of the uppermost layer of the Ge(111) crystal face.

The experimental techniques and the method of data processing have been described in detail elsewhere [1, 2, 4]. The Ge(111)–(2 × 8) surface was prepared for the EELS measurements using a conventional procedure, including mechanical grinding and polishing in air, followed by repeated Ar$^+$ ion sputter and annealing cycles in vacuum. The secondary electron energy spectrum was measured as a function of the primary beam energy in the reflection mode. The secondary electron take-off angle (determined by the analyzer entrance aperture) was 90°, so that the EELS signal measured was integral with respect to the scattering angle. The results of our measurements showed that the bulk (E_b) and surface (E_s) plasmon energies on the Ge(111)–(2 × 8) surface

depend on the primary electron energy (E_p) as depicted in Fig. 1.

Below, we will consider the energy dependence of the surface plasmon energy $E_s(E_p)$, since this quantity is more sensitive to the structure of the uppermost surface layer. Following [1], we relate this energy dependence to the dispersion $\omega_s(k)$, where ω_s and k are the frequency and the wavevector of the surface plasma oscillations. The dispersion relation is established by applying the laws of conservation of the energy and momentum in the elementary event of plasmon excitation by a primary electron [5].

When the secondary electrons are detected in the direction of mirror reflection with respect to the inci-
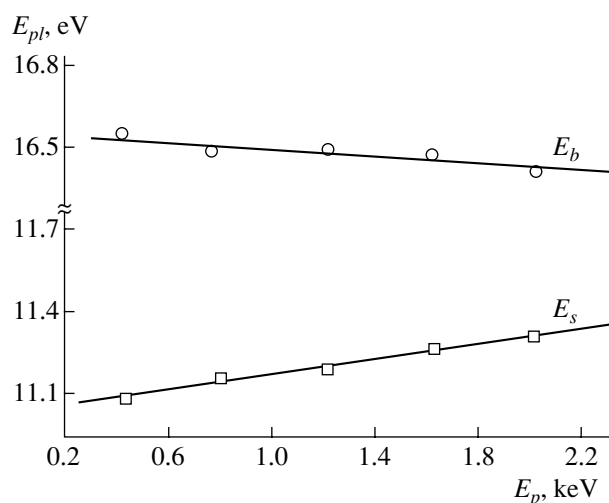

Fig. 1. Plots of the bulk (E_b) and surface (E_s) plasmon energies versus primary energy E_p for the Ge(111)–(2 × 8) crystal face studied by electron energy loss spectroscopy.

dent electron beam, the minimum (and most probable) value of the wavevector is

$$ k = \sqrt{\frac{m}{2}} \frac{E_s}{\hbar \sqrt{E_p} \sin\theta}, \qquad (1) $$

where m is the electron mass and θ is the angle of electron beam incidence relative to the surface normal (in our case, $\theta = 60°$). The direct use of relation (1) for analysis of the experimental energy dependences of the surface plasmon energy is hindered by the aforementioned angular averaging for the secondary electrons detected in the reflection mode (see [1]). This factor leads to an effective increase (by our estimates, up to a several tens of percent) in the k value at a given primary electron energy E_p.

Taking the above circumstance into account, we applied relation (1) to the experimental $E_s(E_p)$ curve and obtained the dispersion curve for the surface plasma oscillations, which is depicted in Fig. 2. As can be seen, the plot is characterized by a negative slope, which is evidence (as in the case of the Al(111) face) of a certain change in the structure of the surface layers on the Ge(111) surface. Using the model proposed in [1], it is possible to take into account the contribution from the inhomogeneity of the electron profile to the dispersion of surface plasma oscillations. At small k values ($kd \ll 1$, where d is surface the thickness), the dispersion can be expressed as

$$ \omega_s = \omega_{pb}/\sqrt{2} + \alpha k, \qquad (2) $$

where

$$ \alpha \equiv (\omega_{pb}/n_b\sqrt{2})\int_0^d (n(z) - n_b)ds, \qquad (3) $$

$n(z)$ is the variable electron density in the surface transition layer, n_b is the bulk electron density, and ω_{pb} is the bulk plasmon frequency. By measuring the slope of the linear portion of the experimental dispersion curve in Fig. 1 and using relation (2), we can determine an effective decrease in electron density on the Ge(111)–(2 × 8) crystal face, which amounts to approximately 3%. A thickness of this transition layer can also be estimated from the position of a nonmonotonic portion of the dispersion curve. This yields about 0.5 nm, which corresponds to 2–3 atomic monolayers.

Therefore, the EELS data show evidence of a change in the structure of the surface atomic layers on the Ge(111)–(2 × 8) crystal face. We relate this decrease in the density to reconstruction of the Ge(111) crystal face. The 2 × 8 superstructure is well described by an adatom model (NIST Surface Structure Database) featuring a large effective loosening of the uppermost surface layers.
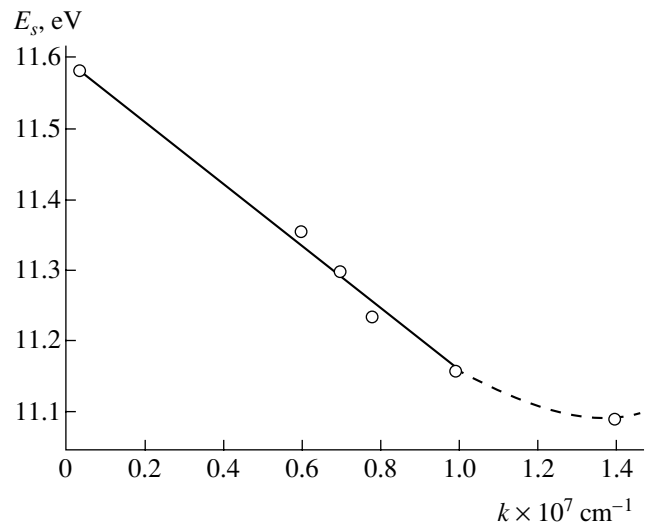
Fig. 2. The surface plasmon energy E_s versus wavevector k plotted by the EELS data for the Ge(111)–(2 × 8) surface.

It should be borne in mind that the theory [6] predicts that covalent crystals (in contrast to metals) must feature a decrease in the length of chemical bonds (i.e., contraction of the crystal lattice) on the surface. However, this prediction does not take into account the surface reconstruction. According to the adatom model for a reconstructed Ge(111)–(2 × 8) crystal face, the surface layer exhibits an integral loosening even if the underlying are contracted. Thus, our EELS results confirm validity of the conventionally accepted adatom model of the reconstructed Ge(111)–(2 × 8) crystal face.

REFERENCES

1. V. E. Korsukov, A. S. Luk'yanenko, and V. N. Svetlov, Poverkhnost, No. 11, 28 (1983).

2. V. E. Korsukov, A. S. Luk'yanenko, P. V. Patrievskiĭ, and V. N. Svetlov, Poverkhnost, No. 5, 27 (1987).

3. J. Xie, S. de Gironcili, S. Baroni, and M. Scheffler, J. Appl. Phys. **81** (1) (1997).

4. R. R. Nazarov, V. E. Korsukov, A. S. Luk'yanenko, and M. Shermatov, Poverkhnost, No. 1, 97 (1990).

5. H. Raether, Shpringer Tracts Mod. Phys. **38**, 157 (1965).

6. B. A. Nesterenko and O. V. Snitko, *Physical Properties of Atomically Clean Semiconductor Surfaces* (Naukova Dumka, Kiev, 1983).

Translated by P. Pozdeev

Approximate Analytical Solution of the Takagi Equations for X-ray Diffraction in the Backscattering Mode from a Cylindrically Bent Crystal

T. Tchen

Moscow State Academy of Fine Chemical Technology, Moscow, Russia
e-mail: docent65@mtu-net.ru; ttchen@e-mail.ru
Received October 10, 2002

Abstract—The dynamic diffraction of a spherical X-ray wave from a cylindrically bent crystal in the backscattering mode has been theoretically studied. An approximate analytical solution of the system of Takagi differential equations is obtained under certain conditions imposed on the coordinates of atoms inside the crystal. © 2003 MAIK "Nauka/Interperiodica".

The dynamic theory of Bragg diffraction for hard X-ray radiation scattered from an elastically bent crystal has been developed by Chukhovskii *et al.* [1–3]. In particular, the exact analytical solution of the Takagi equations was obtained for the Bragg angles $\theta_B \neq \pi/2$ in a crystal with arbitrary radius of bending. However, the theory developed in [1–3] is not quite correct in describing X-ray diffraction in the reverse direction (i.e., in the backscattering mode).

This paper presents an analytical solution of the system of Takagi differential equations for one particular case of a spherical wave diffracted in the backscattering mode from a cylindrically bent crystal.

Consider a monochromatic spherical X-ray wave $\mathbf{E}_0(\mathbf{r}, t) = \mathbf{E}_0(\mathbf{r}, \omega)\exp(i\mathbf{k}_0\mathbf{r} - i\omega t)$ outgoing from a point source and incident onto a cylindrically bent crystal. The source is situated on the z axis coinciding with the internal normal to the crystal surface at its center. Here, ω is the frequency of the incident wave, $|\mathbf{k}_0| = \kappa = \omega/c = 2\pi/\lambda$, c is the speed of light, and λ is the X-ray wavelength. Let us assume that the angle φ_0 between vector $\mathbf{k}_0$ and the normal $\mathbf{n}$ to the reflecting surface at the crystal center falls within the interval $|\chi_{hr}| \leq \varphi_0 \leq |\chi_{hr}|^{1/2}$. Under this condition, we may ignore the effects of multiple scattering upon the backscattered wave.

In a two-wave approximation, the wave field in the crystal represents a coherent sum of the transmitted and backscattered waves:

$$\mathbf{E}(\mathbf{r}, t) = \mathbf{E}_0(\mathbf{r}, t) + \mathbf{E}_h(\mathbf{r}, t), \qquad (1)$$

where $\mathbf{E}_h(\mathbf{r}, t) = \mathbf{E}_h(\mathbf{r}, \omega)\exp(i\mathbf{k}_h\mathbf{r} - i\omega t)$ is the electric field of the diffracted wave, $\mathbf{k}_h = \mathbf{k}_0 + \mathbf{h}$, $\mathbf{h}$ is the reciprocal lattice vector of the ideal unbent crystal, $|\mathbf{k}_h|^2 \approx$

$|\mathbf{k}_0|^2 = \kappa^2$, $\mathbf{r}(x, y, z)$ is the radius vector of an arbitrary atom in the crystal lattice, $\mathbf{E}_{0, h}(\mathbf{r}, \omega) = E_{0, h}(\mathbf{r}, \omega)\mathbf{e}_{0, h}$, and $\mathbf{e}_{0, h}$ are the unit vectors of polarization.

The wave field $\mathbf{E}(\mathbf{r}, t)$ is a solution of the Maxwell equation

$$-(\nabla^2 + \kappa^2)\mathbf{E} = \kappa^2\chi(\mathbf{r}), \qquad (2)$$

where $\chi(\mathbf{r})$ is the X-ray polarizability of the crystal. Expanding this polarizability into a Fourier series and restricting the expansion to the first three terms, we obtain

$$\chi(\mathbf{r}) = \chi_0 + \chi_h\exp\{i\mathbf{h}\mathbf{r} - i\mathbf{h}\mathbf{u}(\mathbf{r})\} + \chi_{-h}\exp\{-i\mathbf{h}\mathbf{r} + i\mathbf{h}\mathbf{u}(\mathbf{r})\}. \qquad (3)$$

Here, vector $\mathbf{u}(\mathbf{r})$ describes the displacement of atoms in the crystal lattice upon elastic bending of the crystal. As is known [1–3] for the system under consideration, $\mathbf{u}(\mathbf{r})$ represents a quadratic function of the initial atomic coordinates (x and y) in the unbent crystal. In this study, we are interested only in the z component of vector $\mathbf{u}$:

$$u_z = -x^2/2R_x - z^2/2R_z, \qquad (4)$$

where R_x is the radius of crystal bending in the plane of diffraction reflection and R_z is the radius representing a certain combination of components of the reciprocal tensor of elastic moduli. For diffraction in the backscattering mode,

$$\mathbf{h}\mathbf{u} = \kappa(x^2/R_x + z^2/R_z).$$

Substituting (1) and (3) into Eq. (2) and assuming amplitudes $E_{0, h}$ to be slowly varying over a distance on

the order of λ, we obtain a system of two Takagi differential equations

$$2i(1-\gamma_0^2)^{1/2}\partial E_0/\partial x + 2i\gamma_0 \partial E_0/\partial z$$
$$+ \kappa\chi_0 E_0 + \kappa C \chi_{-h}\exp(i\mathbf{hu})E_h = 0,$$
$$2i(1-\gamma_h^2)^{1/2}\partial E_h/\partial x + 2i\gamma_h \partial E_h/\partial z$$
$$+ \kappa(\chi_0 - \alpha)E_h + \kappa C \chi_h \exp(-i\mathbf{hu})E_0 = 0. \qquad (5)$$

Here, $\gamma_0 = (\mathbf{k}_0\mathbf{n})/\kappa = -\gamma_n = -(\mathbf{k}_n\mathbf{n})/\kappa$, $C = (\mathbf{k}_0\mathbf{k}_h)/\kappa^2 = -1$ is the polarization factor for a backscattering wave, $\alpha = (\mathbf{k}_h^2 - \mathbf{k}_0^2)/\kappa^2 = 2(\Delta\theta)^2$, $\Delta\theta = \theta - \pi/2$, and θ is the sliding angle for the incident plane harmonic wave.

Now consider a symmetric X-ray wave diffraction in the reverse direction (backscattering), whereby we can assume that $\gamma_0 = -\gamma_h = 1 - \varphi_0^2/2$ ($\varphi_0 \ll 1$). Then $(1 - \gamma_0^2)^{1/2} = (1 - \gamma_h^2)^{1/2} \cong \varphi_0$. Let $\varphi_0 = D|\chi_{hr}|^{1/2}$, where D is a dimensionless coefficient. Below we will consider the case of $D = \pm 1$, which corresponds to the edge of the total backscattering curve.

Let the condition $|\chi_{hr}|^{1/2}\partial E_{0,h}/\partial x \ll \partial E_{0,h}/\partial z$ be satisfied for a point with the coordinates (x, z) inside the crystal, as well as on the crystal surface. This implies that all the following relations are valid provided that $x \gg |\chi_{hr}|^{1/2}z$. For the backscattering reflection (199) from a Si crystal ($|\chi_{hr}| \cong 2.39 \times 10^{-7}$), this condition is quite well satisfied for $0 < z < 100$ μm and $x \gg 5 \times 10^{-8}$ m. For the atoms displaced by $u_z = -x^2/2R_x$, where $x \cong l_x/2$, $l_x \le 10^{-2}$ m is the crystal plate size along the x axis, and $R_x \ge 10$ m, the above condition is also valid for distances on the order of interatomic spacing.

Ignoring the terms involving partial derivatives with respect to x in the Takagi equations and representing the wave amplitudes as $E_{0,h}(x, z) = E_{0,h}(x)E_{0,h}(z)$, the system of equations (5) can be reduced to a second-order differential equation for the diffracted wave amplitude $E_h(z)$:

$$d^2 E_h/dz^2 + A(z)dE_h/dz + B(z)E_h(z) = 0, \qquad (6)$$

where

$$A(z) = A_1 + A_2 z, \quad A_1 = 2i\kappa(\Delta\theta)^2, \quad A_2 = 2\kappa/R_z.$$

$$B(z) = B_1 + B_2 z, \quad B_1 = \kappa^2\{\chi_0(\chi_0 + \alpha) - \chi_h\chi_{-h}\}/4, \qquad (7)$$

$$B_2 = i(\chi_0 + \alpha)\kappa^2/R_z, \quad \alpha = 2(\Delta\theta)^2.$$

A solution of Eq. (6) can be found in the form of a Fourier integral

$$E_h(z) = (2\pi)^{-1}\int dk\, G_h(k)\exp(ikz) \qquad (8)$$

with the boundary condition $E_h(z \longrightarrow \infty) \longrightarrow 0$. For the Fourier component $G_h(k)$, we obtain a differential equation of the first order,

$$(-A_2 k + iB_2)\partial G_h/\partial k - (k^2 - ikA_1 - B_1 - A_2)G_h = 0, \qquad (9)$$

with the boundary condition $G_h(k \longrightarrow \pm\infty) \longrightarrow 0$. A solution to Eq. (9) is given by the function

$$G_h(k) = \exp(-k^2/2A_2 + iA_1 k/A_2 - iB_2 k/A_2^2)$$
$$\times (1 + ikA_2/B_2)^{(-A_3)}, \qquad (10)$$

where

$$A_3 = (A_1 A_2 B_2 - B_2^2 - B_1 A_2^2 - A_2^3)/A_2^3. \qquad (11)$$

For an ideal unbent crystal ($A_2 \longrightarrow 0$, $B_2 \longrightarrow 0$), the function $G_h(k)$ reduces to the delta function $\delta(k - \varepsilon_{1,2})$, where $\varepsilon_{1,2}$ is the excitation errors for the ideal crystal:

$$\varepsilon_{1,2} = \{iA_1 \pm (-A_1^2 + 4B_1)^{1/2}\}/2$$
$$= \kappa(2)^{-1}\{(-\alpha/2) \pm [(\chi_0 + \alpha/2)^2 - \chi_h\chi_{-h}]^{1/2}\}. \qquad (12)$$

The x-dependent diffracted wave amplitude is $E_h(x) = \exp(-i\kappa x^2/R_x)$.

For the transmitted wave amplitude, it is possible to obtain a differential equation of the second order analogous to Eq. (6).

REFERENCES

1. F. N. Chukhovskii, K. T. Gabrielyan, and P. V. Petrashen', Acta Cryst. A **34**, 610 (1978).
2. F. N. Chukhovskii, K. T. Gabrielyan, and P. V. Petrashen', Dokl. Akad. Nauk SSSR **238**, 81 (1978) [Sov. Phys. Dokl. **23**, 52 (1978)].
3. K. T. Gabrielyan, F. N. Chukhovskii, and D. I. Piskunov, Zh. Éksp. Teor. Fiz. **96**, 834 (1989) [Sov. Phys. JETP **69**, 474 (1989)].

Translated by P. Pozdeev

The Topology of "Vacuum" in a Dielectric Waveguide

I. V. Dzedolik

Tauride National University, Simferopol, Ukraine
e-mail: dzedolik@crimea.edu
Received September 30, 2002

Abstract—The energy states of a nonlinear system of the electromagnetic field–dielectric waveguide type is considered. It is shown that this system possesses a manifold of "vacuum" states with a zero "internal" energy. The presence of such states is evidence that the system can feature field states in the form of three-dimensional solitary waves. © *2003 MAIK "Nauka/Interperiodica".*

Since the very appearance of quantum mechanics, it has been possible to describe the quantum particles in terms of waves [1]. On the other hand, there were attempts at describing classical waves as fluxes of quasiparticles [2, 3]. In the case of a field propagating in a nonlinear medium, the formation of both periodic cnoidal waves and solitary waves possessing the properties of particles is possible for a certain relation between the parameters of the field and the medium [4]. The existence of such a field in the form of solitary waves possessing the properties of particles (solitons) is related to the ability of the field–medium system to form topological vacuum states with zero internal energy, in which the field magnitude can be nonzero [5].

Let us determine such vacuum states of a classical electromagnetic field–dielectric waveguide system. To this end, consider the propagation of electromagnetic radiation in an isotropic dielectric waveguide possessing the shape of a circular cylinder. Taking into account the cubic response of the waveguide medium (quartz), a nonlinear equation for the electric field strength $\mathbf{E}$ can be written as

$$\left(\nabla^2 - \frac{\varepsilon_1}{c^2}\frac{\partial^2}{\partial t^2}\right)\mathbf{E} = \frac{4\pi\chi_3}{c^2}\frac{\partial^2}{\partial t^2}|\mathbf{E}|^2\mathbf{E}, \tag{1}$$

where $\nabla = \mathbf{l}_x\partial/\partial x + \mathbf{l}_y\partial/\partial y + \mathbf{l}_z\partial/\partial z$ is the nabla operator, $\mathbf{l}_{x,y,z}$ are the unit vectors, and $\varepsilon_1 = 1 + 4\pi\chi_1$.

Assuming that $\mathbf{E}$ is a harmonic function of the time (i.e., ignoring the generation of harmonics), we can present the field in the form of waveguide modes with real amplitudes $\mathbf{e}(\mathbf{r})$:

$$\mathbf{E} = \mathbf{e}(r)\exp(ikl\varphi)\exp[i(\omega t - \beta z)] \tag{2}$$
$$(\kappa = \pm 1,\ l = 0, 1, 2, \ldots).$$

Then, substituting expression (2) into Eq. (1), we obtain

a system of equations in the cylindrical coordinates

$$\left(\frac{d^2}{dR^2} + \frac{1}{R}\frac{d}{dR} - \frac{l^2}{R^2}\right)e_j + m^2 e_j + \alpha e^2 e_j = 0 \tag{3}$$
$$(j, k = x, y, z),$$

where

$$m^2 = r_0^2(\omega^2\varepsilon_1/c^2 - \beta^2), \quad \alpha = 4\pi\chi_3 r_0^2\omega^2/c^2,$$

$$e^2 = \sum_{j = x, y, z} e_j^2, \quad R = r/r_0 \in [0, 1],$$

and r_0 is the waveguide radius. The mode propagation constants β are determined from a dispersion equation [6]. Note that the field equation (3) has the form of a nonlinear steady-state Klein–Gordon equation. This implies that the electromagnetic field propagating in the waveguide can be considered (in view of the discreteness of the spectrum of the propagation constants β_l) as a flux of quasiparticles possessing effective dimensionless masses $m_l = r_0\sqrt{\omega^2\varepsilon_1/c^2 - \beta_l^2}$.

Upon substituting $e_j = \psi_j(R)/\sqrt{R}$, the system of equations (3) can be written in the form of equations describing the motion of a quasiparticle under the action of a central force:

$$m_l\ddot{\psi}_x = -\frac{\partial U_l}{\partial\psi_x}, \quad m_l\ddot{\psi}_y = -\frac{\partial U_l}{\partial\psi_y},$$
$$m_l\ddot{\psi}_z = -\frac{\partial U_l}{\partial\psi_z}, \tag{4}$$

where upper dot indicates differentiation with respect to R;

$$U_l = \frac{m_l}{2}\left(m_l^2 - \frac{l^2 - 1/4}{R^2}\right)\psi^2 + \frac{\alpha m_l}{4R}(\psi^2)^2$$

is the potential; and $\psi^2 = \psi_x^2 + \psi_y^2 + \psi_z^2$. A Hamiltonian of this system has the following form:

$$H = \frac{1}{2}\dot{\psi}^2 + \frac{1}{2}\left(m_l^2 - \frac{l^2 - 1/4}{R^2}\right)\psi^2 + \frac{\alpha m_l}{4R}(\psi^2)^2. \quad (5)$$

In the configuration space, the first term describes the "kinetic" energy (in real space, the potential energy) depending on the rate of the field strength variation in space; the second and third terms describe the internal energy of the system.

Let us determine the states of the system in which $H = $ const. The ground state (with a zero potential energy (5), whereby $\dot{\psi}^2/2 = 0$) corresponds to the internal energy

$$E_I = \frac{\alpha}{4R}(\psi^2)^2 + \frac{1}{2}\left(m_l^2 - \frac{l^2 - 1/4}{R^2}\right)\psi^2. \quad (6)$$

In the excited state, the potential energy is positive, so that vacuum states can take place only when the internal energy is zero ($E_I = 0$). This yields an equation for the field components in the vacuum states,

$$\psi^4 - \frac{2R}{\alpha}\left(m_l^2 - \frac{l^2 - 1/4}{R^2}\right)\psi^2 = 0,$$

which has solutions on the spheres with the square radius

$$\psi_l^2 = \frac{2R}{\alpha}\left(m_l^2 - \frac{l^2 - 1/4}{R^2}\right) > 0.$$

On the waveguide axis ($R = 0$), all field components at $E_I = 0$ are zero: $\psi_x = \psi_y = \psi_z = 0$.

In a system possessing more than one vacuum state, the transitions from one to another vacuum state can take place without energy dissipation, whereby the field acquires the form of a solitary wave (soliton) [5]. At the same time, it is known that soliton solutions correspond to a system trajectory of the phase plane representing separatrix passing through the points $\psi_S = 0$, $dU_l(\psi_S)/d\psi = 0$ [4]. The equation

$$\frac{dU_l}{d\psi} = \psi_S^3 + \frac{R}{\alpha}\left(m_l^2 - \frac{l^2 - 1/4}{R^2}\right)\psi_s = 0$$

has the solutions

$$\psi_S = 0, \quad \psi_{Sl} = \sqrt{\frac{R}{\alpha}\left(\frac{l^2 - 1/4}{R^2} - m_l^2\right)}.$$

Substituting ψ_{Sl} into expression (5), we determine the system energies corresponding to the soliton solutions:

$$H_S = -\frac{m_l R}{4\alpha}\left(m_l^2 - \frac{l^2 - 1/4}{R^2}\right)^2.$$
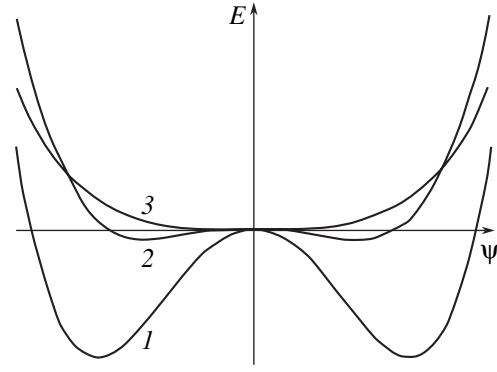
Fig. 1. Profiles of the internal energy E_I calculated for $m_l = 1$, $l = 1$, $\alpha = 0.1$, and $R = 0.4$ (*1*), 0.5 (*2*), and 1 (*3*).
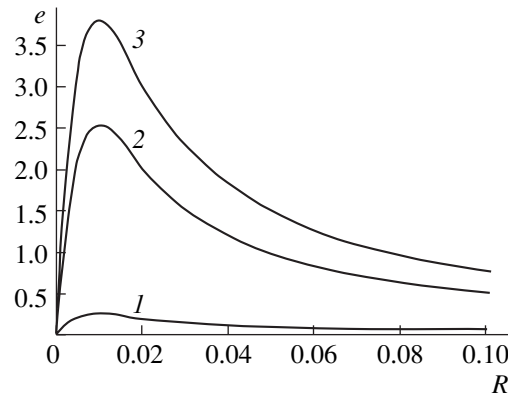
Fig. 2. Profiles of the electric field components calculated for $m_l = 1$, $l = 1$, and $\alpha = 0.1$: (*1*) e_z for $e_z(0) = 0.01$; (*2*) e_x for $e_x(0) = 0.1$; (*3*) e_y for $e_y(0) = 0.15$.

Figure 1 shows the shape of the potential $E_I(\psi, R)$ for various values of the parameter R. Solutions for the field components (e_x, e_y, e_z) of a solitary wave, obtained upon solving Eqs. (3) by numerical methods, are presented in Fig. 2. As can be seen from Fig. 1, the form of the potential E_I depends on the proximity of boundaries (that is, on the parameter R representing the normalized waveguide radius). The potential possesses a characteristic shape favoring a spontaneous breakage of the system symmetry and, hence, making possible particle-like solutions in the region far from the boundaries ($R \neq 1$).

Now let us consider the propagation of a nonmonochromatic electromagnetic field through the waveguide. A vector equation describing the wave packet in a co-moving frame (with $\tau = t - z/v$) moving with the velocity of the packet is

$$\left(\nabla_{\perp}^2 - \frac{1}{u^2}\frac{\partial^2}{\partial\tau^2}\right)\mathbf{E} = \alpha\frac{\partial^2}{\partial\tau^2}|\mathbf{E}|^2\mathbf{E}, \quad (7)$$

where

$$\nabla_\perp = \mathbf{l}_x \frac{\partial}{\partial x} + \mathbf{l}_y \frac{\partial}{\partial y}, \quad \frac{1}{u^2} = \frac{\varepsilon_1}{c^2} - \frac{1}{v^2}, \quad \alpha = \frac{4\pi\chi_3}{c^2}.$$

Upon extracting the slowly varying amplitude and phase of the field $\mathbf{E} = \mathbf{e}(\mathbf{r}, \tau)\exp(i\omega\tau)$ and substituting the expression for $\mathbf{E}$, we can separate the real and imaginary parts of Eq. (7):

$$\left(\nabla_\perp^2 - \frac{1}{u^2}\frac{\partial^2}{\partial\tau^2} + \frac{\omega^2}{u^2}\right)\mathbf{e}$$

$$= \alpha\left(\frac{\partial^2 e^2}{\partial\tau^2} + e^2\frac{\partial^2\mathbf{e}}{\partial\tau^2} + 2\frac{\partial\mathbf{e}}{\partial\tau}\frac{\partial e^2}{\partial\tau} - \omega^2 e^2\mathbf{e}\right), \quad (8)$$

$$\frac{\partial\mathbf{e}}{\partial\tau} = -\alpha u^2\frac{\partial(e^2\mathbf{e})}{\partial\tau}.$$

To the first approximation in $\alpha \ll 1$, relations (8) yield a vector equation for the wave packet envelope:

$$\left(\frac{1}{u^2}\frac{\partial^2}{\partial\tau^2} - \nabla_\perp^2\right)\mathbf{e} = \left(\frac{\omega^2}{u^2} + \alpha\omega^2 e^2\right)\mathbf{e}. \quad (9)$$

If Eq. (9) admits a conserved topological current [7], not related to invariance of the Lagrangian

$$L = \frac{1}{2}\left(\frac{1}{u}\frac{\partial\mathbf{e}}{\partial\tau}\right)^2 - \frac{1}{2}(\partial_q\mathbf{e})^2 + \frac{\omega^2}{2u^2}\mathbf{e}^2 + \frac{\alpha\omega^2}{4}(\mathbf{e}^2)^2$$

with respect to any transformations, this equation possesses soliton solutions. The topological current can be expressed as $J_q^i = e^{ij}\partial_j e_q$, where

$$e^{ij} = \begin{pmatrix} 0 & 1 & 1 \\ -1 & 0 & 1 \\ -1 & -1 & 0 \end{pmatrix}$$

is the antisymmetric unit tensor (i, $j = 0$, 1, 2; $q = 1$, 2, 3). Using the equation of motion (9), we obtain an expression describing conservation of the topological current: $\partial_i J_q^i = 0$.

Thus, the electromagnetic field–dielectric waveguide system possesses a complicated topological structure characterized by the presence of degenerate vacuum states with zero energy. These regions are formed depending on the system energy. The presence of degenerate vacuum states is evidence that an electromagnetic field in the dielectric waveguide can exist in the form of three-dimensional solitary waves possessing the properties of particles.

REFERENCES

1. L. D. Landau and E. M. Lifshits, *Quantum Mechanics: Non-Relativistic Theory* (Nauka, Moscow, 1989; Pergamon Press, Oxford, 1977).

2. N. Markuvits, Trudy Inst. Inzh. Elektron. Radiotekhn. **66** (11), 25 (1980).

3. L. A. Rivlin, Kvantovaya Élektron. (Moscow) **30**, 185 (2000).

4. G. M. Zaslavskiĭ and R. Z. Sagdeev, *Nonlinear Physics: from the Pendulum to Turbulence and Chaos* (Nauka, Moscow, 1988; Harwood, Chur, 1988).

5. K. Rebbi, Usp. Fiz. Nauk **130**, 329 (1980).

6. A. W. Snyder and J. D. Love, *Optical Waveguide Theory* (Chapman and Hall, London, 1983; Radio i Svyaz', Moscow, 1987).

7. L. Ryder, *Quantum Field Theory* (Cambridge University Press, Cambridge, 1985; Mir, Moscow, 1987).

Translated by P. Pozdeev

The Effect of Sample Mass on the Crystallization Supercooling in Bismuth Melt

V. D. Aleksandrov and V. A. Postnikov

Donbass State Academy of Civil Engineering and Architecture, Donetsk, Ukraine
e-mail: mailbox@dgasa.donetsk.ua
Received October 15, 2002

Abstract—The effect of a sample mass (decreasing from 100 g to 0.1 mg) on the crystallization supercooling (ΔT^-) relative to the melting temperature T_L has been studied for bismuth. The entire mass range can be divided into three regions: for massive samples ($m = 100$–6 g), ΔT^- is about several kelvins; for medium masses (1 g to 1.0 mg), ΔT^- amounts to 30 ± 4 K and is virtually independent of m; below 0.1 mg, ΔT^- exhibits a rapid growth. © 2003 MAIK "Nauka/Interperiodica".

Introduction. As is known, the magnitude of crystallization supercooling (ΔT^-) of a melt depends on the sample size d, initial overheating (ΔT^+) relative to the melting temperature T_L, cooling rate (v), and some other factors. Sufficiently large masses of a metal (>100 g) cooled at a "normal" rate (0.01–0.5 K/s) admit only a relatively small supercooling of 1–3 K [1, 2]. At the same time, quenching massive metal samples at a rate of 10^5–10^8 K/s can be accompanied by significant supercooling [3]: in a 150-g sample of iron cooled under such conditions, ΔT^- reached about 270 K, while 80−100 g samples of nickel exhibited supercoolings as large as about 305 K.

The samples of Sb, Sn, Bi, Pb, InSb, and some others with masses ranging from 0.01 to 10 g, melted with small overheating (several kelvins) above T_L and cooled at a low to moderate rate (0.001–10 K/s) exhibit crystallization without supercooling ($\Delta T^- \approx 0$). The same samples overheated 30–50 K above T_L and cooled at the same rates can be supercooled within several tens of kelvins: $\Delta T^- = 10$–30 K (Sn), 11–30 K (Bi), 12–17 K (Pb), 55–65 K (Sb), 25–35 K (InSb) [4–9].

Nanodimensional and microscopic drops usually exhibit significant supercooling when cooled at an ultrahigh rate (10^5–10^8 K/s) [1– 4, 10–15]. Under these conditions, liquid particles of Sb, Sn, Bi, Pb, Cu, Fe, and other metals with dimensions of 40–500 μm can be supercooled below T_L up to 118, 110, 80, 135, 236, and even 550 K, respectively. Still greater supercoolings were reported in [16], where 12-μm particles of Ag, Au, Cu, and Ni showed $\Delta T^- = 245$, 220, 340, and 245 K, respectively. Considerable supercoolings in drops cooled at low rates (~0.33 K/s) were observed in [18], where the relative supercooling $\Delta T^-/T_L$ reached 0.17 (Al), 0.23 (Sb), 0.41 (Bi), 0.19 (Cd), 0.58 (Ga), 0.26 (In), and 0.37 (Sn).

Ultrasmall drops were reported to obey the following empirical relation between the drop size d and supercooling ΔT^- [14]: $\ln d = A_0 - A_1(\Delta T^-/T_L)$, where A_0 and A_1 are constant coefficients. However, this relation does not include the cooling rate v, which is an important parameter usually strongly influencing the ΔT^- value. The dependence of supercooling on the sample size d for Sn, Bi, and Fe was reported in [15]: for $v = 100$–500 K/s, the ΔT^- values in these metals changed from 110–115 K for $d = 40$–50 μm to 60–80 K for $d = 200$–300 μm.

The above data show that some researchers are interested in studying massive samples, while the others investigate ultrasmall particles. The data on supercoolings reported for the same substances are rather contradictory. This is by no means surprising considering the variety of experimental methods employed, ranging from thermal analysis to electron microscopy. No systematic data were reported on the crystallization supercoolings in a wide range of sample masses studied by the same method under equal experimental conditions.

Here we present the results of a thermographic investigation of the effect of a sample mass in the range from ~0.1 to 100 g on the magnitude of supercooling (relative to the melting temperature T_L) for the crystallization of bismuth from melt. Bismuth offers a convenient object for such investigations, since this metal has a relatively low melting temperature T_L, is virtually not oxidized by air in the vicinity of this temperature, and is susceptible to sufficiently large supercoolings at usual cooling rates.

Experimental. The experiments were performed with bismuth of a special purity grade (OSCh), from which the samples were prepared with average masses about 0.1 (I), 1.2 (II), 9.8 (III), and 112.3 mg (IV) and 1 (V), 6 (VI), 26 (VII), and 100 g (VIII). The masses of
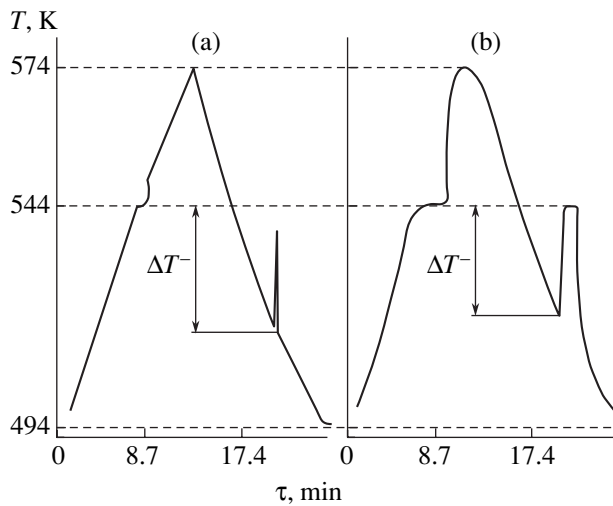
Fig. 1. Typical thermograms recorded during the melting–cooling cycles for bismuth samples with $m = 1$ mg (a) and 1 g (b).
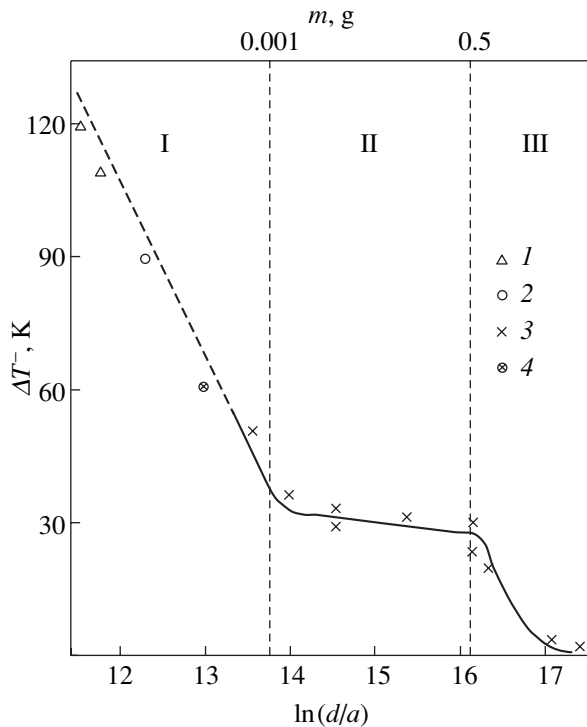

Fig. 2. A plot of supercooling ΔT^- versus logarithm of the relative sample size d/a for bismuth: (*1*) data from [15]; (*2*) data from [14]; (*3*) our thermographic data; (*4*) our microscopic data for a sample with $m = 0.1$ mg.

samples II–VIII were measured with an electronic balance of the VLKT-500g-M type; the mass of the smallest sample (I) was determined using the average size measured by the optical method. The data were obtained by measuring 8–13 samples of each mass.

The process of bismuth melting and crystallization was studied by the method of sequential thermal cycling [5, 6, 16]. The temperature of samples II–VIII were determined using chromel–alumel thermocouples with a diameter of 0.1 mm. Samples III–VIII were studied in alundum crucibles, while sample II was placed onto a flattened junction of the thermocouple. The thermocouple readings were recorded with a KSP-4 chart-recording potentiometer (2 mV scale). The error of the temperature measurements was ~0.5 K. The supercooling of sample I (weighing ~0.1 mg) was studied visually with the aid of a MIM-8 microscope, in which the metal particles were heated and cooled using a special attachment equipped with a chromel–alumel thermocouple, which allowed the samples to be heated and cooled at a controlled rate of $v = 0.1 \pm 0.01$ K/s in a temperature range from 494 to 574 K (for bismuth, $T_L \approx 544$ K). An overheating of 30 K above T_L is sufficient for the melt to lose memory of the initial crystalline state [4, 5]. Still smaller particles (below 0.1 mg) could not be studied by the methods employed.

The reliability of results was confirmed by multiply repeated measurements on the same sample (up to 15 heating–cooling cycles) and on the analogous samples of each mass. The supercooling was characterized by averaging over the values of ΔT^- determined in several thermal cycles. The scatter of ΔT^- values observed for the same sample mass and cooling rate was within $\pm(2–3)$ K about the average value $\langle \Delta T^- \rangle$.

Results. Figure 1 shows typical thermograms observed on heating and cooling of Bi samples with masses about 1 mg and 1 g in a temperature range including melting and crystallization processes. As can be seen, the crystallization supercooling ΔT^- is about 35 K for the 1-mg sample and 31 K for the 1-g sample.

Figure 2 presents a generalized plot of supercooling ΔT^- versus logarithm of the relative sample size d/a. The size d was calculated using the values of mass m and density ρ, assuming a cubic shape of the sample: $d = (m/\rho)^{1/3}$. For bismuth, the density in the vicinity of T_L is $\rho \approx 10.07 \times 10^3$ kg/m^3 and the rhombohedral lattice parameter is $a \approx 0.47$ nm [18]. For comparison, our results are plotted together with the data of other researchers [4, 9, 14, 15, 17]. As can be seen, the entire range of sample dimensions can be divided into three parts representing ultrasmall particles (I), medium masses (II), and large masses (III). For the latter massive samples ($m \geq 26$ g), the values of supercooling are very small, ranging within 3–5 K (region III). For the samples of medium masses (1 mg to 6 g), the ΔT^- value is virtually independent of the particle size and amounts to 30 ± 4 K in the entire region II. This is consistent with Fig. 1, where a decrease in the sample mass by three orders of magnitude is accompanied by a change in the supercooling ΔT^- of about 4 K (i.e., within the error interval of ΔT^- scatter from cycle to cycle). In region I corresponding to small particles, ΔT^- strongly depends on the size d. This is illustrated by a change from $\Delta T^- = 34$ K (for $m = 1$ mg) to 50 K (for $m =$

0.1 mg) and by the data of other researchers [14, 15] for smaller particles.

Discussion. There arise natural questions as to which value of the supercooling is "true" and in which of regions I–III it is most informative for identifying the mechanism of crystallization. Taking into account that the driving force of a phase transition of the first kind is the difference of the Gibbs free energies ΔG between the coexisting phases and that ΔG is a function of ΔT^-, we must conclude that ΔT^- is a physical parameter of the crystallizing medium. This parameter determines the critical nucleus size, the work required for the formation of a nucleus, and the nucleation rate [2].

In massive samples, featuring large temperature gradients and inhomogeneous temperature fields, the crystallization heat in the initial stage is "dissipated" within a certain local region and the temperature probe (thermocouple, etc.) detects only small signals. Therefore, small values of supercooling observed in massive samples are not very informative and are hardly applicable to calculations of various nucleation parameters. These values do reflect the essence of physicochemical processes involved in the phase transition.

The region of ultrasmall samples has to be treated within the framework of the physics of small particles [19]. Here, various size effects can operate and significantly influence the melting temperature, heat capacity, surface tension, etc. Therefore, the possibility of using large supercooling values (achieved under hardly controllable conditions in particles possessing specific properties) in the nucleation theory is problematic. Statements that a decrease in the amount of foreign impurities (crystallization initiators) with decreasing sample size renders the process more homogeneous and reveals the "true" crystallization onset can be disputed. First, such statements [2, 4, 15] have never been confirmed by data on any particular impurities, their concentrations, and their role as the crystallization activators or inhibitors. Second, even small drops usually contact with a heterogeneous substrate that can act as the activator of crystallization; the smaller the particle size, the greater the fraction of surface atoms contacting with the substrate and the closer the process character to heterogeneous. Third, the concentration of foreign impurities in both small and large samples is the same, being independent of the degree of comminution.

We believe that using medium sample masses (from ~1 mg to ~10 g) for studying the parameters of crystallization kinetics is very convenient and more informative. Important effects include a jumplike transition from the equilibrium crystallization at $\Delta T^- = 0$ to a nonequilibrium (explosive) process at $\Delta T^- \neq 0$ depending on the degree of overheating, the absence of spontaneous crystallization in the course of prolonged (hours) isothermal melt exposure in the region of supercooling, etc. These phenomena were observed in medium-size samples of both bismuth [6] and other metals [5, 20–22].

REFERENCES

1. G. F. Balandin, *Principles of the Theory of Casting Formation* (Metallurgiya, Moscow, 1979).
2. B. Chalmers, *Principles of Solidification* (Wiley, New York, 1964; Metallurgiya, Moscow, 1968).
3. V. N. Gudzenko, Doctoral (Tech. Sci.) Dissertation (Dnepropetrovsk. Gos. Univ., Dnepropetrovsk, 1977).
4. V. I. Danilov, *Structure and Crystallization of Liquids* (Naukova Dumka, Kiev, 1956).
5. V. D. Aleksandrov and A. A. Barannikov, Khim. Fiz. **17** (10), 140 (1998).
6. V. I. Petrenko and V. D. Aleksandrov, Pis'ma Zh. Tekh. Fiz. **9**, 1354 (1983) [Sov. Tech. Phys. Lett. **9**, 582 (1983)].
7. M. P. Korobkova, V. P. Maksimov, V. P. Cherpakov, *et al.*, in *Selected Problems in Solid State Physics* (Voronezh, 1969), Vol. 1, pp. 159–165.
8. K. F. Kobayashi, M.-I. Kumikawa, and P. H. Shingu, J. Cryst. Growth **67**, 85 (1984).
9. S. I. Zadumkin, Kh. I. Ibragimov, and D. T. Ozniev, Izv. Vyssh. Uchebn. Zaved., Tsvet. Metall., No. 1, 82 (1979).
10. I. T. Gladkikh, S. V. Dukarov, and V. N. Sukhov, Fiz. Met. Metalloved. **78** (3), 87 (1994).
11. V. K. Yatsimirskiĭ, Zh. Fiz. Khim. **51**, 1041 (1977).
12. G. T. Butorin and V. P. Skripov, Fiz. Met. Metalloved. **33**, 1255 (1972).
13. M. Ya. Dashevskiĭ and A. N. Poterukhin, Izv. Akad. Nauk SSSR, Ser. Neorg. Mater. **4**, 689 (1968).
14. T. Takahashi and W. A. Tiller, Acta Metall. **17**, 643 (1969).
15. A. I. Dukhin, Probl. Metalloved. Fiz. Met., No. 6, 9 (1959).
16. V. D. Aleksandrov and A. A. Barannikov, Pis'ma Zh. Tekh. Fiz. **24** (14), 73 (1998) [Tech. Phys. Lett. **17**, 573 (1998)].
17. D. M. Rasmussen, K. Yaved, M. Appleby, *et al.*, Mater. Lett. **3**, 344 (1985).
18. *Tables of Physical Quantities*, Ed. by I. K. Kikoin (Moscow, 1976).
19. V. V. Pavlov, Rasplavy, No. 5, 35 (2000).
20. Ya. S. Umanskiĭ and Yu. A. Skakov, *Physics of Metals* (Atomizdat, Moscow, 1978).
21. V. D. Aleksandrov, Neorg. Mater. **28**, 709 (1992).
22. V. D. Aleksandrov, M. R. Raukhman, V. I. Borovik, *et al.*, Metally, No. 6, 184 (1992).

Translated by P. Pozdeev

High-Power 1.7–1.8 μm Single-Mode Laser Diodes

A. V. Lyutetskiĭ, N. A. Pikhtin*, S. O. Slipchenko, N. V. Fetisova, A. Yu. Leshko, E. G. Golikova, Yu. A. Ryaboshtan, and I. S. Tarasov

Ioffe Physicotechnical Institute, Russian Academy of Sciences, St. Petersburg, Russia
SigmaPlus Company, Moscow, Russia
* *e-mail: nike@hpld.ioffe.rssi.ru*
Received November 21, 2002

Abstract—Separate confinement InGaAsP/InP laser heterostructures were grown by metalorganic-hydride vapor-phase epitaxy. High-power single-mode laser diodes of mesastripe design based on these heterostructures operate in a wavelength interval of 1.7–1.8 μm with a maximum continuous room temperature output power of 150 mW. The single-mode lasing regime is maintained up to an output power level of 100 mW. © *2003 MAIK "Nauka/Interperiodica"*.

The wavelength range of 1.7–2.0 μm is highly attractive, especially in relation to rapidly developing fiber communication systems with superlow optical losses [1], environmental monitoring [2], and spectroscopy of industrial gases [3]. In connection with these potential applications, there is increasing demand for high-power single-mode lasers operating in the indicated spectral range.

There are two possibilities for obtaining laser diodes operating in the middle IR range. The first is to grow laser diode heterostructures in the AlInGaAsSb/GaSb solid solution system [4, 5], while an alternative is offered by the InGaAsP/InP system [2, 6, 7]. For several reasons, the second approach is considered as advantageous for the technology of lasers emitting in the range of wavelengths below 2 μm [8]. Some recent papers have been devoted to InAsN solid solutions as a promising base for the laser diodes emitting in the 1.7–2.0 μm interval [9, 10]. However, these investigations possess a preliminary character, and the real potential of the new system still cannot be assessed.

This paper expands our concept of high-power semiconductor lasers [11–16] to a wavelength interval of 1.7–1.8 μm, which has been already successfully explored by developers of high-power laser diode systems [1–3, 6–8]. We report on the properties of single-mode laser diodes emitting at 1.7–1.8 μm, based on separate confinement InGaAsP/InP laser heterostructures grown by metalorganic-hydride vapor-phase epitaxy (MOVPE).

Previously [15], we have demonstrated the properties of high-power multimode long-wavelength (1.7–1.8 μm) laser diodes. In order to realize a single-mode generation regime, it was necessary to optimize the laser diode structure and design. The proposed laser heterostructure comprises the following system of epitaxial layers: heavily doped n-InP ($n = 6 \times 10^{17}$ cm^{-3})

and p-InP ($p = 7.8 \times 10^{17}$ cm^{-3}) emitters (with silicon and zinc as the donor and acceptor impurity, respectively), a waveguide representing an intentionally undoped 0.6-μm-thick layer of InGaAsP solid solution, and an active region formed by two 76-Å-thick InGaAsP strained quantum wells (QWs) separated by a 195-Å-thick InGaAsP intermediate waveguide layer.

The laser diode had a basic mesastripe design [12]. In such devices, single-mode generation is provided by a jump (Δn_L) in the effective refractive index in the plane parallel to the p–n junction. As was demonstrated in [16], the Δn_L value is influenced by many factors, the most important being the free charge carriers and the temperature. A certain difficulty of taking these factors into account is related to the fact that both the free charge carrier density in the waveguide and in the active region, as well as the temperatures of these layers, vary depending on the pumping current.

In order to obtain the maximum output power of a laser diode operating in a single-mode regime, we have calculated the structure parameters using a passive waveguide model [17]. The values to be optimized were the etching depth and the stripe width, for the given values of the laser heterostructure parameters. The process of selective etching during the formation of mesastripes of required thickness was terminated by a special 70-Å-thick InGaAsP stopping layer grown in the p-InP emitter. Using a standard postgrowth processing technology [12, 16] and the results of calculations, we fabricated heterolaser structures with a stripe width of $W = 4.5$ μm and various lengths of the Fabry–Perot resonator ($L = 200$–2000 μm). Finally, the laser diodes were mounted with the stripes downside onto copper heat sinks and fixed with the aid of an indium-based solder.

The laser diode samples were studied by measuring the output power–current (P–I) characteristics in a continuous wave (CW) regime at a heat sink temperature of 20°C. These data were used to determine the internal quantum efficiency of stimulated emission ($\eta_i = 55\%$) and the internal optical losses ($a_i = 10$ cm^{-1}). Figure 1 shows a typical P–I curve of a laser diode with $L = 2000$ μm and with high reflection and antireflection coatings applied onto the resonator edges (with power reflection coefficients of 5 and 95%, respectively). The maximum output power of such laser diodes reached 150 mW, as limited by heating of the active region.

An increase in the temperature of the active region leads to a decrease in the emission characteristics of laser diodes [11], one of the reasons being a growth in the threshold carrier density in the QWs [18]. This growth affects the threshold current. In order to characterize the temperature sensitivity of the threshold current, we measured the P–I curves in a pulsed regime at various temperatures of the heat sink. The resulting experimental dependence of the threshold current (I_{th}) on the heat sink temperature (T) varied in the range from 10 to 70°C can be described by an empirical expression

$$I_{th}(T) - I_{th}(300 \text{ K})\exp(T - 300 \text{ K}/T_0),$$

which yields the characteristic temperature parameter $T_0 = 50$ K (for the laser diodes with $L = 1000$–2000 μm). This was a minimum value for laser diodes based on the InGaAsP/InP solid solution system and operating at 1.3–1.55 μm [12]. However, the laser diodes emitting at $\lambda = 1.7$–1.8 μm are characterized by greater QW depths as compared to the devices with $\lambda = 1.3$ μm. According to estimates, the QW depth for electrons in laser heterostructures with the same waveguide energy bandgap width (E_{gw}) increases by 92 meV. For a laser diode with $\lambda = 1.3$ μm and $E_{gw} = 1.23$ eV, the QW depth for electrons is $E_{QWe} = 91$ meV and $T_0 = 70$ K [12], while the proposed laser structure has an effective waveguide with $E_{gw} = 1.23$ eV, a nearly doubled E_{QWe}, and $T_0 = 50$ K.

One possible reason for the observed increase in the temperature sensitivity can be a growth in the intensity of the nonradiative Auger recombination process in the active region due to a greater radiation wavelength. However, this by no means implies that a further increase in the QW depth will not effectively improve the temperature stability of the emission characteristics of laser diodes [18, 19]. For laser diodes based on the AlInGaAsP/InP solid solution system (where the QW depth can be increased), the characteristic temperature parameter T_0 increased by a factor greater than 1.5 as compared to the devices implementing the classical InGaAsP/InP system [19, 20].
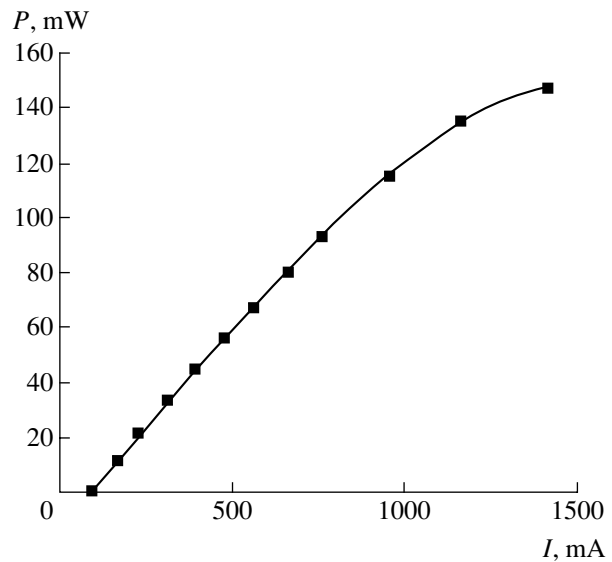
Fig. 1. The plot of output power P versus pumping current I for a laser diode with a resonator length $L = 2000$ μm, stripe width $W = 4.5$ μm, and high (95%) and low (5%) reflecting coatings on the resonator edges, operating in a CW regime at a heat sink temperature of 20°C.
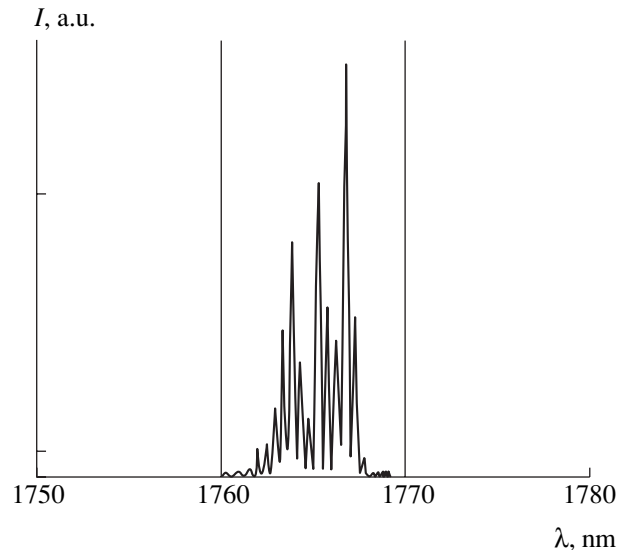

Fig. 2. The emission spectrum of a laser diode with $L = 2000$ μm operating in a CW regime at a pumping current of $1.5I_{th}$.

Figure 2 shows the emission spectrum of a single-mode laser diode operating in the CW regime at a pumping current of $1.5I_{th}$. The distance between the adjacent modes in this spectrum corresponds to the distance between zeroth longitudinal modes of the Fabry–Perot resonator. This result confirms that the laser diode generates a fundamental optical mode.

Figure 3 presents a plot of the peak wavelength versus pumping current for a laser diode operating in a CW regime. As is seen, an increase in the injection level
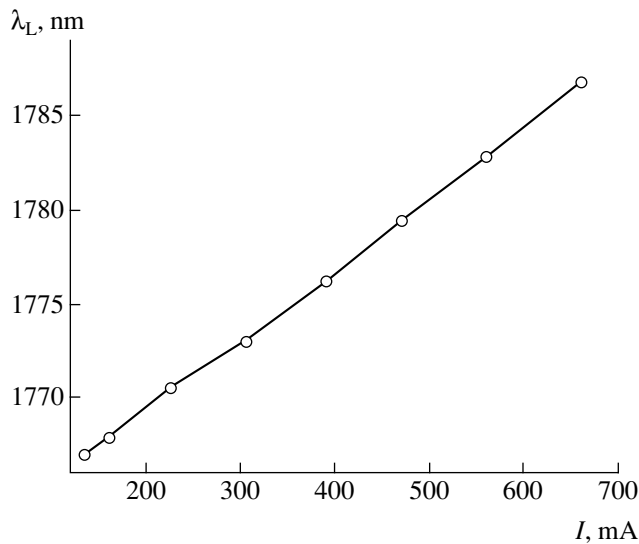
Fig. 3. A plot of the peak wavelength versus pumping current for a laser diode operating in a CW regime at a heat sink temperature of 20°C.
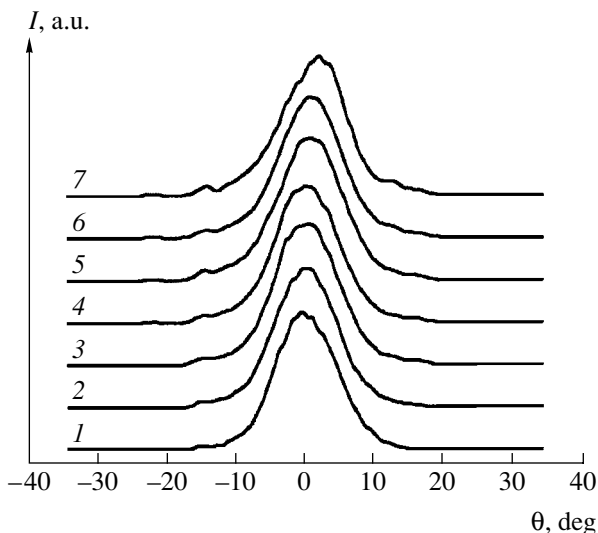

Fig. 4. Distribution of the radiation intensity in the far zone in the plane parallel to the *p–n* junction for a laser diode with $L = 2000$ μm operating in the continuous regime for various pumping currents. The full width at half maximum is $\Theta_{\parallel} = 10.5$ (*1*), 10.6 (*2*), 10.9 (*3*), 10.7 (*4*), 11.1 (*5*), 10.6 (*6*), and 10.1 deg (*7*); the corresponding output power is $P = 5$ (*1*), 20 (*2*), 40 (*3*), 60 (*4*), 80 (*5*), 100 (*6*), and 120 mW (*7*).

smoothly shifts the output radiation spectrum toward longer wavelengths. This is evidence of the active region heating.

The data in Fig. 4 show the distribution of laser radiation intensity in the far zone in the plane parallel to the *p–n* junction for various pumping currents. As can be seen, the full width at half maximum remains virtually constant for currents up to $9I_{th}$, which is one of the cri-

teria of single-mode operation. Further increase in the pumping current leads to a shift of the far field pattern (Fig. 4). In our opinion, this shift is caused by the beam stearing effect [16]. The power corresponding to the maximum pumping current of the laser diode operating in a single-mode continuous regime reached up to 100 mW, which is a record level for single-mode lasers emitting at $\lambda = 1.7–1.8$ μm [7, 8, 21].

Thus, we have fabricated separate confinement InGaAsP/InP laser heterostructures with strained QWs by metalorganic-hydride vapor-phase epitaxy. High-power single-mode laser diodes of mesastripe design based on these heterostructures operate in a wavelength interval of 1.7–1.8 μm. The laser diode structure parameters were optimized so as to maintain singemode lasing at a maximum output power. In the samples studied, single-mode generation was possible up to 100 mW, while the maximum power in a continuous operation regime at room temperature reached up to 150 mW. For laser diodes with a resonator length of 1000–2000 μm, the characteristic temperature parameter is $T_0 = 50$ K.

REFERENCES

1. J.-S. Wang, H.-H. Lin, and L.-W. Sung, IEEE J. Quantum Electron. **QE-34**, 1959 (1998).

2. J. Dong, A. Ubukata, and K. Matsumoto, Jpn. J. Appl. Phys. **36**, 5468 (1997).

3. M. Mitsuhara, M. Ogasawara, M. Oishi, *et al.*, IEEE Photonics Technol. Lett. **11**, 33 (1999).

4. H. K. Choi, G. W. Turner, and S. I. Eglash, IEEE Photonics Technol. Lett. **6**, 7 (1994).

5. D. Z. Garbuzov, H. Lee, V. Khalfin, *et al.*, IEEE Photonics Technol. Lett. **11**, 794 (1999).

6. R. U. Martinelli, T. J. Zamerowski, and P. A. Longeway, Appl. Phys. Lett. **54**, 277 (1989).

7. R. U. Martinelli, R. J. Menna, A. Triano, *et al.*, Electron. Lett. **30**, 324 (1994).

8. J. S. Major, D. W. Nam, J. S. Osinski, and D. F. Welch, IEEE Photonics Technol. Lett. **5**, 733 (1993).

9. M. Kondow, K. Uomi, T. Kitatani, *et al.*, J. Cryst. Growth **164**, 175 (1996).

10. H. Naoi, Y. Naoi, and S. Sakai, Solid-State Electron. **41**, 319 (1997).

11. E. G. Golikova, V. A. Kureshov, A. Yu. Leshko, *et al.*, Fiz. Tekh. Poluprovodn. (St. Petersburg) **34**, 886 (2000) [Semiconductors **34**, 853 (2000)].

12. E. G. Golikova, V. A. Gorbylev, Yu. V. Il'in, *et al.*, Pis'ma Zh. Tekh. Fiz. **26** (7), 57 (2000) [Tech. Phys. Lett. **26**, 295 (2000)].

13. E. G. Golikova, V. A. Gorbylev, N. Yu. Davidyuk, *et al.*, Pis'ma Zh. Tekh. Fiz. **26** (6), 5 (2000) [Tech. Phys. Lett. **26**, 225 (2000)].

14. D. A. Livshits, A. Yu. Egorov, I. V. Kochnev, *et al.*, Fiz. Tekh. Poluprovodn. (St. Petersburg) **35**, 380 (2001) [Semiconductors **35**, 365 (2001)].

15. E. G. Golikova, V. A. Kureshov, A. Yu. Leshko, *et al.*, Pis'ma Zh. Tekh. Fiz. **28** (3), 66 (2002) [Tech. Phys. Lett. **28**, 113 (2002)].

16. A. Yu. Leshko, A. V. Lyutetskiĭ, N. A. Pikhtin, *et al.*, Fiz. Tekh. Poluprovodn. (St. Petersburg) **36**, 1393 (2002) [Semiconductors **36**, 1308 (2002)].

17. S. L. Chuang, *Physics of Optoelectronic Devices* (Wiley, New York, 1995).

18. G. G. Zegrya, N. A. Pikhtin, G. V. Skrynnikov, *et al.*, Fiz. Tekh. Poluprovodn. (St. Petersburg) **35**, 1001 (2001) [Semiconductors **35**, 962 (2001)].

19. S. O. Slipchenko, A. V. Lyutetskiĭ, N. A. Pikhtin, *et al.*, Pis'ma Zh. Tekh. Fiz. **29** (3), 65 (2003) [Tech. Phys. Lett. **29**, 115 (2003)].

20. G. K. Kuang, G. Bohm, N. Graf, *et al.*, IEEE Photonics Technol. Lett. **13**, 275 (2001).

21. M. Ochiai, H. Temkin, S. Forouhar, and R. A. Logan, IEEE Photonics Technol. Lett. **7**, 825 (1995).

Translated by P. Pozdeev

Effect of the External Coupling of Cavities on the Stability and Output Power of a Relativistic Magnetron

I. I. Vintizenko*, V. I. Gusel'nikov, A. I. Zarevich, and S. S. Novikov

Research Institute of Nuclear Physics, Tomsk Polytechnic University, Tomsk, Russia
Tomsk State University, Tomsk, Russia
* e-mail: lablia@npi.tpu.ru
Received October 22, 2002

Abstract—Autooscillation regimes in a relativistic magnetron with external mutual coupling of cavities have been studied. It is demonstrated that the interaction of oscillations under mode competition conditions significantly increases the stability of the working oscillation mode and improves the spectral characteristics of radiation. © *2003 MAIK "Nauka/Interperiodica".*

Microwave tubes with distributed interaction, being multifrequency autooscillation systems, can feature the competition and the related instability of modes. These phenomena are especially typical of superhigh-power magnetron oscillators. In the presence of unstable external fields, oscillations of various types can arise in such devices both between and within working pulses [1, 2]. In the classical variant, the problem of stabilization of the generation process can be effectively solved by using rising-sun systems or straps. Unfortunately, these methods are usually inapplicable in relativistic magnetrons.

A promising means of increasing the stability of oscillators consists in introducing external coupling [3]. In a relativistic magnetron, external coupling can be provided by a waveguide linking different cavities. In this case, the interaction of oscillation components in the magnetron resonance system is physically analogous to the process of coherent interaction in systems of mutually locked autooscillators. Therefore, stable magnetron sources can be created using methods developed for coherent multioscillator systems [4–7]. High stability of the locked oscillation regimes in these systems is achieved for a certain organization of the coupling channels, including common dissipative load elements.

Here we report on the results of experimental investigation of the energy and spectral characteristics of microwave radiation of a relativistic magnetron with external mutual coupling of cavities.

Figure 1 shows a schematic diagram of the experimental setup. Two opposite cavities of a six-cavity S-band relativistic magnetron *1* (pumped from a linear induction accelerator section *2*) are linked by a coupling waveguide *3* via tapers *4* and a 3-dB waveguide H-tee *5*. The waveguide tee allows microwave energy to be extracted from the system via radiating pyramidal horn antenna *6*. Using straps *7*, it is possible to change

(in a discrete manner) the total coupling pathlength and the symmetry of load (radiator).

The experimental setup [8] according to this scheme generates microwave pulses at a repetition frequency of up to 320 Hz at a cathode–anode voltage level of 400–500 kV and a total current of 2.5–3 kA; the system is characterized by highly reproducible working parameters. In these experiments, we determined the power, measured the spectrum of pulsed microwave radiation, and monitored the total current and working voltage of the magnetron (the signal envelopes were used to calculate the total energy per pulse). The parameters of radiation were measured using amplitude detectors and a tunable narrow-band filter.

Operation of the microwave radiation source was studied in three variants: (i) magnetron with uncoupled cavities; (ii) magnetron with waveguide-coupled cavi-
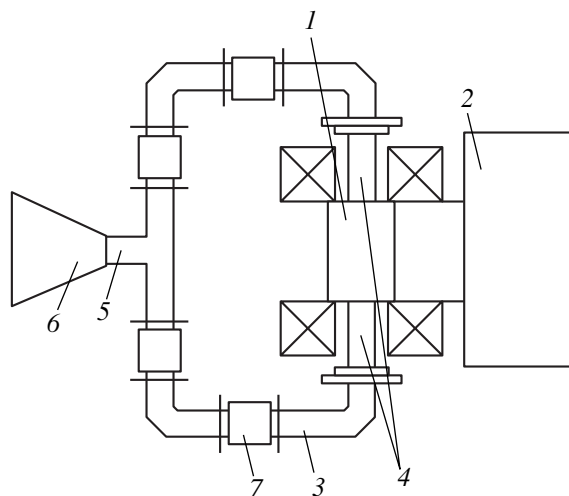

Fig. 1. Schematic diagram of the experimental setup (see the text for explanations).

ties and symmetric radiator arrangement; and (iii) magnetron with waveguide-coupled cavities and antisymmetric radiator arrangement. The latter antisymmetric configuration was obtained by displacing the waveguide H-tee by 90° (electrical angle for the working magnetron wavelength) relative to the electrical symmetry axis of the coupling waveguide. In the two configurations with coupled cavities, we have determined the total electrical length of the coupling circuit. Using these data, it was possible to set various phase-shifts of the interacting signals. Thus, the coupling circuit contains a common dissipative load element and has a configuration obeying the principles of multioscillator system design [5–7].

In the relativistic magnetron under consideration, the main competing oscillations are the π and $2\pi/3$ modes. The stable π mode exists in a certain range of magnetic fields (0.3–0.5 T), outside which the $2\pi/3$ mode (0.25–0.3 T) and the corresponding (–1)st harmonic (0.5–0.54 T) are excited. Simultaneous excitation of the competing modes is possible at the boundary (0.5 T) of the mode stability interval. With respect to the azimuth, oscillations of the π mode in the opposite cavities are in phase, while the $2\pi/3$ modes are out of phase. This accounts for the summation of oscillations in the common load for the π modes in the symmetric configuration, and their subtraction in the antisymmetric configuration. In contrast, the $2\pi/3$ modes are subtracted in the symmetric (and added—in antisymmetric) configuration [9]. Using these properties of the system, it is possible to unambiguously identify the working oscillation mode.

The experimental results are presented in Figs. 2–4. Envelopes of the microwave pulses of the magnetron operating with uncoupled cavities (Fig. 2a) in the working range of magnetic fields possess characteristic irregular shapes reflecting instability of the oscillation process. The level of radiation power at each output is ~80 MW at a total energy of ~6 J per pulse. Coupling the cavities in a symmetric configuration at an optimum waveguide pathlength significantly changes the pulse shape (Fig. 2b). The envelopes of the microwave signals become smooth, which is evidence of a more stable magnetron operation. The output power increases to reach ~200 MW, and the pulse energy grows up to ~9 J. This power level corresponds to the regime of summation for the π mode excitation. Upon going to the antisymmetric configuration, the output power drops to ~(7–8) MW, and the energy per pulse, to ~0.5 J (Fig. 2c). Thus, in the latter scheme, oscillations excited in the opposite cavities are subtracted, which unambiguously indicates that the magnetron operates in the π mode.

The effect of the total electrical pathlength of the coupling circuit on the mode stability was most clearly pronounced in the antisymmetric configuration. Figure 3 shows a change in the relative numbers of realizations N_π and $N_{2\pi/3}$ of the corresponding modes in the series of
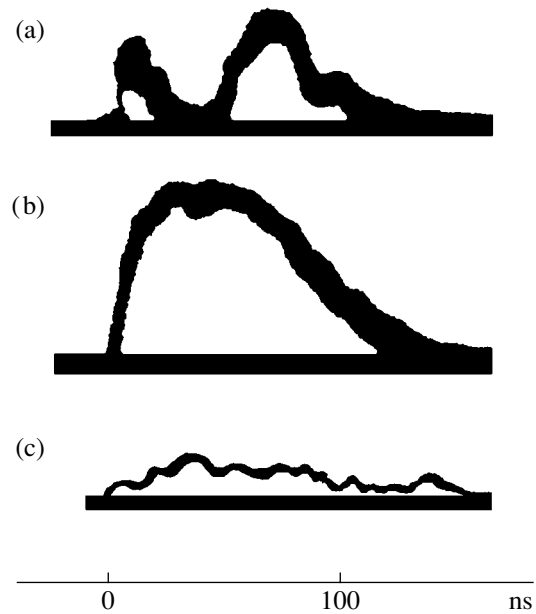

Fig. 2. Oscillograms of the microwave radiation pulses (see the text for explanations).
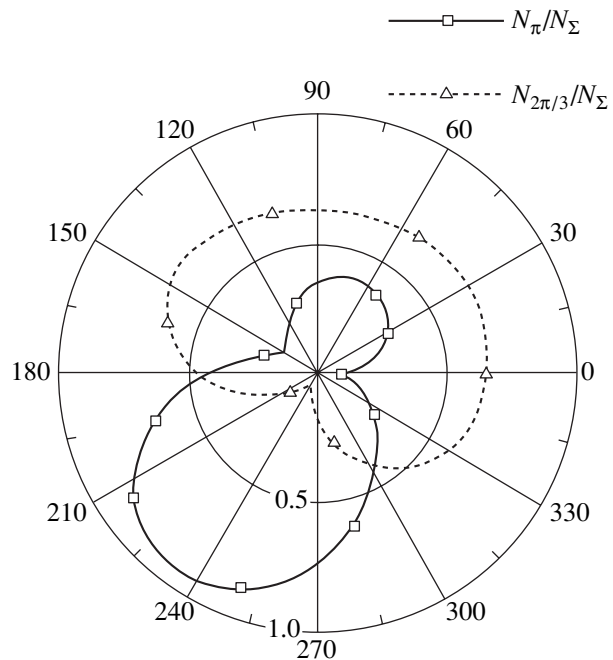

Fig. 3. Angular diagram of the π versus $2\pi/3$ mode competition.

$N_\Sigma \approx 50$ pulses, depending on the total electrical pathlength Θ_Σ of the external coupling circuit at a magnetic induction of $B \approx 0.5$ T. As can be seen, the external coupling provides for an optimum interaction of the π modes (and nonoptimum interaction of the $2\pi/3$ modes) in the angular interval $\Delta\Theta_\Sigma \approx (210–270)°$ (measured relative to certain initial value). Outside this

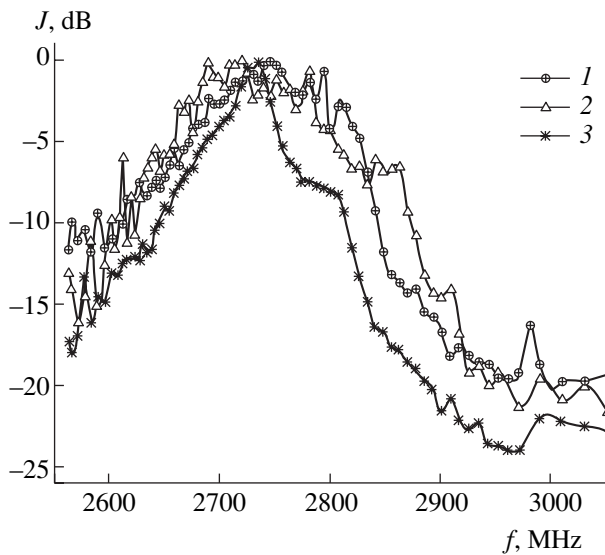**Fig. 4.** Spectral characteristics of microwave radiation pulses.

significantly influences the spectral and energy characteristics of the oscillation process. An original configuration of the coupling circuit is proposed, based on the scheme with common dissipative elements, which significantly increases the output microwave radiation signal parameters. It can be expected that, using a coupling channel with many radiators, it will be possible to create stable, superhigh-power directive radiation sources.

angular interval, the excitation of modes first becomes equiprobable and then changes in favor of the $2\pi/3$ modes.

The waveguide coupling effect is also manifested in the spectral characteristics of radiation. Indeed, the magnetron with uncoupled cavities is characterized by an emission bandwidth of about 4.5% on a –3 dB level (Fig. 4, curve *1*). Coupling the cavities at a nearly optimum waveguide pathlength significantly reduces (to about 1%) the spectral bandwidth (Fig. 4, curve *2*). In other cases (i.e., for a nonoptimum coupling), the bandwidth at the –3 dB level amounts to ~5% or above (Fig. 4, curve *3*).

Thus, the results of our investigations show that the external coupling of cavities in a relativistic magnetron

REFERENCES

1. I. I. Vintizenko, A. S. Sulakshin, L. F. Chernogalova, *et al.*, Pis'ma Zh. Tekh. Fiz. **9**, 482 (1983) [Sov. Tech. Phys. Lett. **9**, 208 (1983)].
2. I. Schnitzer, A. Rosenberg, C. Leibovitz, *et al.*, Proc. SPIE **2843**, 101 (1995).
3. S. A. Kitsanov, A. I. Klimov, S. D. Korovin, *et al.*, *Proceedings of the 1st Int. Congr. on Radiation Physics, High-Current Electronics, and Modification of Materials* (Tomsk, 2000), Vol. 2, p. 423.
4. S. N. Vladimirov, A. S. Maĭdanovskiĭ, and S. S. Novikov, in *Nonlinear Oscillations in Multifrequency Autooscillation Systems* (Izd. Tomsk. Univ., Tomsk, 1993).
5. S. S. Novikov, S. A. Maĭdanovskiĭ, and S. A. Sulakshin, Proc. SPIE **2843**, 293 (1996).
6. S. S. Novikov, Proc. SPIE **3158**, 260 (1997).
7. S. S. Novikov and A. I. Zarevich, *Proceedings of the 1st Int. Congr. on Radiation Physics, High-Current Electronics, and Modification of Materials* (Tomsk, 2000), Vol. 2, p. 466.
8. L. D. Butakov, I. I. Vintizenko, V. I. Gusel'nikov, *et al.*, Pis'ma Zh. Tekh. Fiz. **26** (13), 66 (2000) [Tech. Phys. Lett. **26**, 571 (2000)].
9. RF Patent No. 2190281, cl. H01 J 25/50; I. I. Vintizenko, A. I. Zarevich, and S. S. Novikov, RF Patent Application No. 2001 128 794 (25.10.2001), Byull. Izobret., No. 27 (2002).

Translated by P. Pozdeev

Magnetic Field Filamentation and Quasi-Acoustic–Gravity Waves in Hall Plasmas at Finite Gas-to-Magnetic Pressure Ratios

L. M. Alekseeva

Institute of Nuclear Physics, Moscow State University, Moscow, 119992 Russia
e-mail: a.getling@ru.net
Received November 12, 2002

Abstract—The Hall effect in a plasma flow orthogonal to the magnetic field and invariable in the magnetic field direction can give rise to filamentation of the magnetic flux, splitting it into narrow flux tubes (filaments). This process is due to particular features of the magnetic field generation process in Hall plasmas. The analytical results obtained previously for sharply nonuniform perturbations of the smoothly varying flows of such plasmas are here extended to arbitrary gas-to-magnetic pressure ratios β. The revealed phenomena can be manifested both in laboratory plasmas and under natural conditions (on the Sun). © 2003 MAIK "Nauka/Interperiodica".

The emergence of sharp gradients of physical quantities and the rapid development of a small-scale instability in Hall plasmas was first revealed in numerical simulations of the plasma flows in channels, by solving MHD equations with the Hall effect included (see [1] for a review):

$$\rho \frac{d\mathbf{v}}{dt} = -\nabla \mathscr{P} + \mathbf{j} \times \mathbf{H}, \quad \mathscr{P} = c^2 \rho, \quad \frac{\partial \rho}{\partial t} = -(\nabla \cdot \rho \mathbf{v}),$$
$$\mathbf{j} = \nabla \times \mathbf{H}, \quad (\nabla \cdot \mathbf{H}) = 0, \tag{1}$$

$$\frac{\partial \mathbf{H}}{\partial t} = -\nabla \times \mathbf{E}, \quad \mathbf{E} = \nu \mathbf{j} - \mathbf{v} \times \mathbf{H} + \frac{\xi}{\rho}\left(\mathbf{j} \times \mathbf{H} - \frac{\nabla \mathscr{P}}{2}\right). \tag{2}$$

Here, the magnetic field strength $\mathbf{H}$ and the plasma density ρ are measured in units of their values H_* and ρ_* at a certain reference point; the plasma velocity $\mathbf{v}$ and pressure p, in units of the Alfvén speed and the magnetic pressure at this point, respectively; and distances, in units of the characteristic scale L of the plasma density variation (in the case of a channel, L is the channel length). The equations contain three constants: the exchange parameter $\xi = \hat{c}\, m_i/(eL\sqrt{4\pi\rho_*})$ characterizing the Hall effect, the magnetic viscosity $\nu = \hat{c}^2/(2\pi\lambda_* L v_*)$, and the gas-to-magnetic pressure ratio $\beta = 2c^2$ (where c is the gasdynamic speed of sound, m_i is the ion mass, $\hat{c}$ is the speed of light, and $(-e)$ is the electron charge); the plasma conductivity λ_* is constant, since the plasma is assumed to be isothermal; note also that $\xi/\nu = \omega_e \tau_e$.

Let the plasma flow be everywhere orthogonal to the magnetic field $\mathbf{H}$ directed along the z axis of some Cartesian coordinate system, and let all physical quantities be z-independent. The equation of magnetic field dynamics

$$\frac{\partial \mathbf{H}}{\partial t} = \nu \Delta \mathbf{H} + \nabla \times (\mathbf{v} \times \mathbf{H}) + \xi \nabla \frac{1}{\rho} \times \nabla \frac{H^2}{2} \tag{3}$$

obtained from (2) forms, in combination with Eq. (1), a system for determining the vector $\Pi(x, y, t) = (\rho, \mathbf{v}, H)$. The structure of Eq. (3) indicates that, along with the usual magnetic field generation related to the motion of a conductive medium across $\mathbf{H}$ (the term $\nabla \times (\mathbf{v} \times \mathbf{H})$), an additional, ξ-conditioned field generation takes place in a Hall plasma. This is due to the presence of a density gradient normal to ∇H (see the last term of the equation).[1] This additional Hall generation is obviously stronger where the field H varies more sharply.

---

[1] The magnetic field generation appears to be of a dual origin only if the plasma is treated as a one-fluid medium featuring the Hall effect: it is such a medium that is described by the system of equations (1) and (2) for $\Pi = (\rho, \mathbf{v}, H)$. This system can be obtained from the equations for a two-component plasma consisting of an electron and an ion conductive "fluid," under the easy and natural assumptions that $m_e/m_i \longrightarrow 0$ and $n_i \longrightarrow n_e$. Then, the mean ion velocity proves to be the velocity of the medium $\mathbf{v}_i = \mathbf{v}$, while the velocity of the electron fluid $\mathbf{v}_e$ and the quantities that appear in Eqs. (1) and (2) are related by the equation $\mathbf{v}_e = \mathbf{v} - \xi \mathbf{j}/\rho$. If this relationship is taken into account in (2), Eq. (3) describing the dynamics of $\mathbf{H}$ assumes the form $\partial \mathbf{H}/\partial t = \nu \Delta \mathbf{H} + \nabla \times (\mathbf{v}_e \times \mathbf{H})$ (frequently cited in the literature on Hall plasmas with $\nu = 0$ as evidence for magnetic field lines being frozen in electrons). Therefore, the motion of a conductor—electron fluid—across $\mathbf{H}$ is in fact the only reason for the magnetic field generation. However, this statement does not help us in making particular inferences concerning the behavior of the plasma, since supplementing $(\rho, \mathbf{v}, H)$ with another unknown function $\mathbf{v}_e$ makes the system of equations (1) and (2) nonclosed and requires solving a more sophisticated system of MHD equations for two-component plasmas. We will continue dealing with the convenient and compact system of Eqs. (1) and (2) and, accordingly, with the equation of generation in the form (3). Note also that the role of noncollinear $\nabla \mathscr{P}$ and ∇H was discussed in [1] in the context of the evolutionary properties of the equations.

H, arb. units
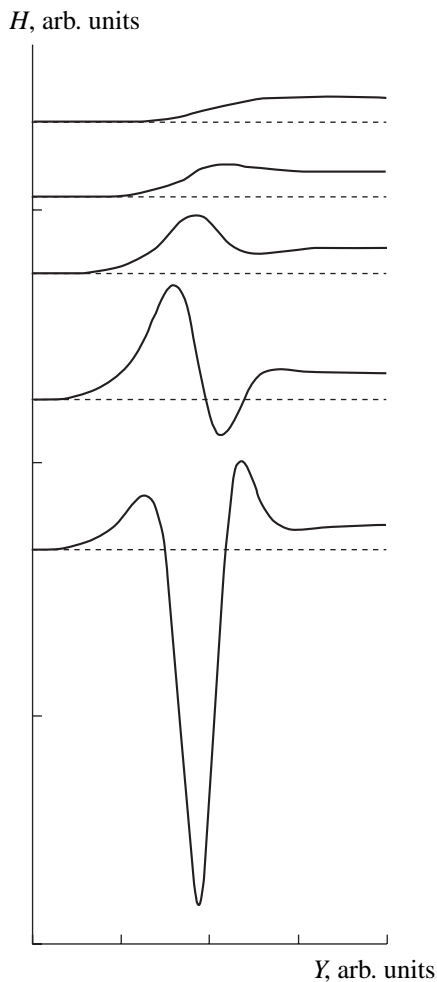
Evolution of a magnetic field with a spatially localized gradient. A time sequence of graphs is arranged from top to bottom. The horizontal dashed straight lines correspond to the H value on the left from the gradient localization region.

Y, arb. units

It is interesting to consider the evolution of a localized ∇H. This can readily be illustrated in the case where the magnetic field does not affect the gasdynamic parameters of the plasma. (A kinematic approach of this sort is frequently used in MHD dynamo theories, which consider the regular self-excitation of magnetic fields in planetary cores and in stars.) Assume that the known vector $\nabla \rho$ is constant over a certain flow region and introduce a right-handed local Cartesian coordinate system (X, Y, z) with the X axis parallel to $\nabla \rho$. Let $\partial/\partial Y$ be nonzero at the initial time only within a certain Y interval (see figure). The Hall generation of the magnetic field due to the density gradient will result in steepening of the H profile (for the moment, we digress from the normal generation of **H** due to the velocity **v**). The larger $|\nabla H|$, the more intense the generation process. As a result, the self-excitation of a finely structured but strong magnetic field will take place in the region where the seed gradient ∇H is localized. In other words, the magnetic flux will become

progressively more filamented, being split into small-scale flux tubes (filaments) with (generally) strongly differing characteristic **H** values (in particular, these values can even exceed the initial magnetic field, neighboring tubes may contain oppositely directed magnetic field lines, etc.). However, the reduction of the magnetic field scale enhances dissipation, and the flow will settle down to a steady state at a certain stage of the splitting process; this means that filamentation will no longer proceed. In the general, nonkinematic case, the plasma in the region of self-excitation of ∇H will be squeezed into the flux tubes with a relatively weak H. (Possibly, the finely structured patterns observed over the solar photosphere are due to these properties of the Hall plasma sandwiched between the dense MHD plasma and the overlying collisionless plasma.)

Assuming that the well-established flow is stationary, we can derive an expression for the small characteristic scale of filamentation from the very structure of Eqs. (1) and (3); specifically, the thickness of a filament is γ^{-1}, where

$$\gamma = -\frac{\xi}{\nu c^2}\frac{H}{\rho^2}\frac{\partial}{\partial l}\left(c^2\rho + \frac{H^2}{2}\right) \gg 1 \qquad (4)$$

($\partial/\partial l$ being the derivative along the streamline) [2–4].

A steady-state solution to the system of equations (1) and (3) for $c \ll 1$ was found [5–7] to have the form $\Pi(x, y, t) = \Pi^0(x, y) + \tilde{\Pi}(x, y, t)$, where $\tilde{\Pi}(x, y, t) \ll \Pi^0$ represents linear acoustic waves running at the speed c against the background of the given flow Π^0 smoothly varying in space; in a coordinate system (x, y, z) with a streamwise x axis, we have $v_y^0/v_x^0 \sim \delta \ll 1$ for this flow. It turned out that $\tilde{\rho}$ obeys an equation formally coinciding with the well-known equation for atmospheric acoustic–gravity waves [8], and that the quantity γ^{-1} determined by formula (4) in terms of the components of Π^0 plays the role of the scale height of the atmosphere (since Π^0 is a smoothly varying flow, we can assume in (4) that $\partial/\partial l = \partial/\partial x$; we also consider γ to be so large that $\gamma\delta \gg 1$; moreover, we adopt the relationships $\xi \gg c \gg \delta$). Similar to the case of upward traveling atmospheric waves, the wave amplitude $\tilde{\Pi}$ in accelerated flows Π^0 grows rapidly as the wave travels counter to the y axis. The formulas can be simplified if an isomagnetic, iso-Bernoullian solution I^0 to Eqs. (1) and (3) for $\partial/\partial t = \xi = \nu = 0$ is used as Π^0: for the flow I^0, we then have $H^0 = \rho^0$, and, in addition, the principal terms ρ_0 and γ_0 in the expansions of ρ^0 and γ in powers of δ are y-independent. Thus, the function $\tilde{\rho}$ assumes the form

$$\tilde{\rho} = \chi \exp\left(\frac{\xi}{\nu\beta}\rho'_{0x}y\right)\exp[i(ky + \omega t)], \quad k^2\beta = 2\omega^2 \quad (5)$$

(here, the dispersion equation is written for sufficiently high frequencies ω; $\chi(x)$ is an amplitude factor, and the

prime denotes differentiation with respect to the variable indicated in the subscript).

In the same manner, we will now find a solution for the more general case of an arbitrary $c^2 = \beta/2$. The system of equations (1) and (3) then reduces to the equations[2]

$$\tilde{\rho}''_{\tau\tau} = \tilde{\rho}''_{qq} + \mu \tilde{H}''_{qq}, \quad (1 + \mu)\tilde{H}'_q + \tilde{H} = \tilde{\rho}, \qquad (6)$$

where $q = \gamma y$, $\tau = c\gamma t$, and $\mu = H^0 c^{-2}$.

In the particular case of $\Pi^0 = I^0$, solutions to Eqs. (6) in the variables q and τ have the form of plane waves with a real frequency and a complex wavevector. The imaginary part of the wavevector increases in absolute value with the frequency and finally exhibits saturation, whereby formula (5) with a real k proves to be valid for $\tilde{\rho}$ even at an arbitrary β. Again, it represents waves with sharp gradients in space [let us recall that, for $\beta \gtrsim 1$, we have $\xi/\nu \gg 1$ by virtue of formula (4)]. Thus, a moving, either laboratory or natural, Hall plasma is a medium in which waves with acoustic properties (quasi-acoustic–gravity waves) arise at various β. As the waves propa-

gate, they can grow rapidly in amplitude and, therefore, easily reach a nonlinear regime. In this context, it is worth noting the recently observed oscillations in an outer region of the Sun—the transition region between the chromosphere and corona—which can best be identified with nonlinear acoustic waves (see [9] for a review).

---

[2] The choice of the amplitude $\tilde{\Pi} \ll \Pi^0$ must ensure that both the zeroth-order terms of the equations and the terms nonlinear in $\tilde{\Pi}$ are small compared to the linear ones. A sufficient condition to satisfy the latter requirement is $\tilde{H} \ll \min(c^2, \gamma^{-1}\delta^{-1})$. The zeroth terms depend on the structure of Π^0. When deriving (6), we considered separately two situations: flows with $\omega_e \tau_e \gg 1$ for which $\partial H^0/\partial y \lesssim 1$, and arbitrarily magnetized flows for which, however, the magnetic field is weakly nonuniform ($\partial H^0/\partial y \sim \delta$); the latter class includes I^0, for which the range of possible amplitudes $\tilde{H}$ is especially wide (since I^0 does not contribute to the zeroth term of Eq. (3), which reflects the Hall effect).

REFERENCES

1. K. V. Brushlinskiĭ and A. I. Morozov, in *Reviews of Plasma Physics*, Ed. by M. A. Leontovich (Atomizdat, Moscow, 1974; Consultants Bureau, New York, 1980), Vol. 8, pp. 88–163.

2. L. M. Alekseeva, Pis'ma Zh. Tekh. Fiz. **15** (10), 1 (1989) [Sov. Tech. Phys. Lett. **15**, 371 (1989)].

3. L. M. Alekseeva, Dokl. Akad. Nauk SSSR **310**, 567 (1990) [Sov. Phys. Dokl. **35**, 51 (1990)].

4. L. M. Alekseeva, J. Plasma Phys. **61**, 671 (1999).

5. L. M. Alekseeva, Pis'ma Zh. Tekh. Fiz. **17** (13), 6 (1991) [Sov. Tech. Phys. Lett. **17**, 461 (1991)].

6. L. M. Alekseeva, Pis'ma Zh. Tekh. Fiz. **19** (5), 34 (1993) [Tech. Phys. Lett. **19**, 145 (1993)].

7. L. M. Alekseeva, Laser Particle Beams **15**, 65 (1997).

8. H. Lamb, *Hydrodynamics*, 6th ed. (Cambridge University Press, Cambridge, 1932; Gos. Izd. Tekhn.–Teor. Lit., Moscow, 1947).

9. B. Fleck, P. Brekke, S. Haugan, S., *et al.*, ESA Bull., No. 102, 2000.

Translated by A. Getling

Photoinduced Lens Dynamics
Near the Optical Confinement Threshold
in Extrinsic Semiconductors

A. I. Sidorov

Institute of Laser Physics, St. Petersburg, Russia
Received October 23, 2002

Abstract—Spatial dynamics of a negative photoinduced lens in a semiconductor with deep impurity levels has been numerically modeled. A relation between the axial profile of the dynamic lens and the onset of self-defocusing leading to the optical confinement. © *2003 MAIK "Nauka/Interperiodica"*.

Nonlinear optical limiters are employed for protecting the organs of vision and photodetectors from overloading (dazzling) and damage by intense laser radiation [1–3, 8, 9]. In addition, such devices are also used for controlling the amplitude and shape of laser pulses in optical data processing systems. An effective mechanism of the optical confinement is offered by the phenomenon of laser radiation self-defocusing in semiconductors [1–3]. According to this mechanism, the radiation defocusing is caused by the photoproduction of nonequilibrium charge carriers that leads to a change in the effective refractive index of the semiconductor. Recently [3], it was demonstrated that the energy threshold of confinement under the conditions of extrinsic absorption can be as low as a few picojoules—three orders of magnitude lower than that observed under the conditions of two-photon absorption [1, 2]. Since the extrinsic absorption is a one-photon process, a dynamic lens appears before the onset of confinement. Therefore, it is important to study the dynamics of a negative photoinduced lens formation near the confinement threshold and to determine the factors accounting for the development of self-defocusing and the radiation confinement.

The experimental data reported in [3] showed that the confinement effect in extrinsic semiconductors is observed at a radiation intensity level significantly lower than that corresponding to saturation of the extrinsic and two-photon absorption or that leading to the development of thermal effects. At a low radiation intensity, the refractive index profile is also weakly affected by the cascade transitions. Moreover, for $\Delta E < h\nu < E_g$ (where ΔE is the impurity ionization threshold and E_g is the semiconductor bandgap width), we can neglect the one-photon interband absorption as well. Under these conditions, we can simplify description of the carrier photoproduction process and take into

account only the electron transitions from impurity centers to the conduction band [4]:

$$\frac{\partial N}{\partial \tau} + N^2 VS - D\frac{\partial^2 N}{\partial x^2} - \frac{\alpha_0(K-N)}{h\nu K}I(x) = 0. \quad (1)$$

Here, N is the nonequilibrium carrier density, K is the concentration of impurity centers, V is the carrier velocity, S is the probability of impurity recombination, D is the coefficient of diffusion of nonequilibrium carriers, α_0 is the linear absorption coefficient, and $I(x)$ is the incident radiation intensity.

The refractive index of a semiconductor, being a function of the carrier density, can be expressed as

$$n = n_0 + n_1, \quad n_1 = -\sum_i \frac{e^2 N_i}{n_0 \varepsilon_0 m_i \omega^2}, \quad (2)$$

where n_0 is the linear refractive index, m is the effective mass of charge carriers, ω is the radiation frequency, and subscript i indicates the carrier type.

For a low-intensity Gaussian beam, a spatial profile of the electron density (and that of a nonlinear additive to the linear refractive index) is close to Gaussian, while the absolute value of n_1 is small. Under these conditions, the propagation of radiation in the nonlinear medium can be described using the so-called "aberration-free" approximation [5, 6], whereby the beam retains the Gaussian shape. According to this model, a thick nonlinear medium is represented as a sequence of thin nonlinear lenses with focal distances depending on the axial nonlinear additive $n_1(x = 0)$ to the refractive index [6]:

$$f_m = \frac{a w_m^2}{4 n_{1m}(0) L}. \quad (3)$$

Here, m is the lens number, w is the beam radius, and L is the distance between lenses ($L \ll (a w_m^2 / 4 |n_{1m}|^{1/2})$). The transmission of a Gaussian beam through this system can be described in terms of the ABCD matrices [6, 7].
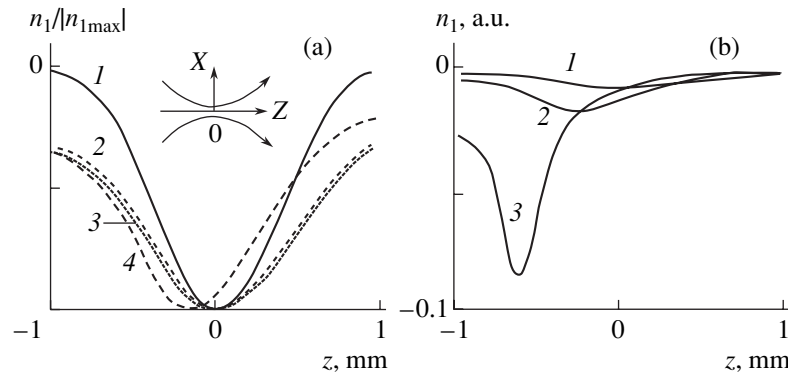
Fig. 1. Axial profiles of a dynamic lens calculated for various incident radiation energies: (a) $E = 10^{-14}$ (*1*), 10^{-12} (2), 5×10^{-12} (3), and 10^{-11} J (4); (b) $E = 10^{-11}$ (*1*), 10^{-10} (2), 5×10^{-9} (3). The inset shows the Gaussian beam geometry in a medium.

We have numerically modeled a 2-mm-thick layer of GaAs transmitting a laser beam with the parameters $\lambda = 1.06~\mu m$, $\tau = 2$ ns, and $w_0 = 0.015$ mm (the Gaussian beam neck radius). The results of numerical calculations for a low incident radiation energy ($0 < E < 10^{-12}$ J) showed that a thick negative lens, symmetric relative to the neck center ($z = 0$), is formed in the direction of the z axis (Fig. 1a). In this energy interval, the lens does not influence the beam parameters and no radiation defocusing takes place. At $E_{thr} \approx 5 \times 10^{-12}$ J, there appears an asymmetry in the axial profile of n_1: the minimum of $n_1(z)$ shifts towards the incident beam (Fig. 1a). This asymmetry in $n_1(z)$ reflects a difference between the lens properties in the left and right parts of the semiconductor plate caused by the radiation self-action. Indeed, the left part of the lens (situated in front of the neck) plays an active role in forming the spatial distribution of the radiation intensity, thus affecting the right-hand part of the lens (situated behind the neck), whereas the reverse action is absent.

Let us determine the conditions under which the lens begins to produce a defocusing effect. The longitudinal neck size (Δz_0) for $w_0 = 0.015$ mm is about 0.7 mm. As can be seen from Fig. 2a, the lens thickness Δz (determined at half maximum of the axial profile of n_1) increases with the incident energy up to about ~1.4 mm

(which corresponds to $2\Delta z_0$). The energy at which this level is attained corresponds to the appearance of asymmetry in the axial profile of n_1 and to the onset of defocusing. Thus, we may conclude that the left, active part of the dynamic lens begins to influence the beam passage through the nonlinear medium when $\Delta z \approx 2\Delta z_0$. In the radiation confinement regime ($E > E_{thr}$), n_1 grows in magnitude and the lens asymmetry increases (Fig. 1b). The region featuring strong variation of the refractive index shifts leftward (towards the incident beam) and the lens thickness Δz decreases (Fig. 2a).

Figure 2b shows a calculated plot of the output radiation energy past a diaphragm situated 50 mm behind the nonlinear medium versus the relative incident beam energy. The energy corresponding to the radiation confinement onset ($E_{in} = E_{thr}$) coincides with that leading to the appearance of asymmetry in the $n_1(z)$ profile.

The results presented above can be used for optimization of the optical characteristics of radiation limiters and for the development of low-threshold optical switches.

REFERENCES

1. T. F. Boggess, A. L. Smirl, S. C. Moss, *et al.*, IEEE J. Quantum Electron. **QE**-21, 488 (1985).
2. E. W. Van Stryland, Y. Y. Wu, D. J. Hagan, *et al.*, J. Opt. Soc. Am. B **5**, 1980 (1988).
3. I. V. Bagrov, A. P. Zhevlakov, A. I. Sidorov, *et al.*, Opt. Zh. **69** (2), 15 (2002).
4. A. I. Sidorov, Opt. Zh. **69** (1), 7 (2002).
5. A. M. Goncharenko, *Gaussian Light Beams* (Nauka i Tekhnika, Minsk, 1977).
6. M. Sheik-Bahae, A. A. Said, D. J. Hagan, *et al.*, Opt. Eng. **30**, 1228 (1991).
7. Yu. A. Anan'ev, *Optical Cavities and Laser Beams* (Nauka, Moscow, 1990).
8. R. C. Hollins, Nonlinear Optics **27** (1–4), 1 (2001).
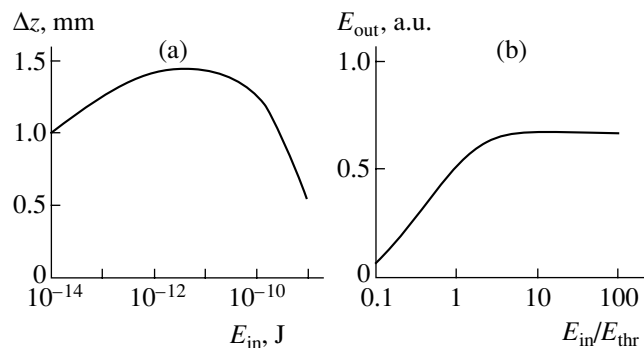9. J. D. Swalen and F. Kajzar, Nonlinear Optics **27** (1–4), 13 (2001).

Fig. 2. Plots of (a) the dynamic lens thickness versus incident radiation energy and (b) the output radiation energy past the limiter versus the relative incident beam energy.

Translated by P. Pozdeev

Three-Dimensional Structure of the Cloud of a Carbon Pellet Evaporated in Plasma of Wendelstein 7-AS Stellarator

B. V. Kuteev[a], V. Yu. Sergeev[a], V. A. Belopol'sky[a],
V. M. Timokhin[a],*, and R. Burhenn[b]

[a] *St. Petersburg State Technical University, St. Petersburg, Russia*
[b] *Max Planck Institut fur Plasmaphysik, EURATOM Ass., D-85748 Garching, Germany*
* *e-mail: timokhin@phtf.stu.neva.ru*
Received September 26, 2002

Abstract—Experiments performed on a Wendelstein 7-AS stellarator revealed asymmetry of the cloud of an ablating carbon pellet. The cloud is elongated in the direction of large radius toward stronger fields, that is, opposite to the direction expected due to the toroidal drift. In order to study the effect in more detail, the three-dimensional structure of the cloud was analyzed by computer tomography. The results confirmed asymmetry of the cloud. This asymmetry is related to a drift flow existing in the plasma and directed along large radius toward stronger fields. The drift velocity is numerically estimated at ~300 m/s. © 2003 MAIK "Nauka/Interperiodica".

The injection of pellets is widely used in investigations of controlled thermonuclear fusion reactions for discharge control and high-temperature plasma diagnostics [1]. An important diagnostic application of pellet injection is the investigation of impurity drift flows in the plasma column. Useful information about such drifts can be obtained by analyzing the spatial structure of clouds formed during pellet ablation [2].

Here we report the first experimental results on the synchronized high-speed bidirectional photography of the clouds of carbon pellets evaporated in the plasma of a Wendelstein 7-AS stellarator (W7-AS). The W7-AS setup and the impurity pellet injection experiment were described in detail elsewhere [3]. The spatiotemporal dynamics of pellet evaporation and the shape of the cloud of evaporated matter were monitored by several high-speed CCD cameras, a video camera, and a wide-aperture photodetector. The interference filters placed in front of all these detectors had a 10-nm-wide transmission band centered at 720 nm (corresponding to CII line). The emission from the cloud was monitored from below, at an angle of about 45° relative to the pellet trajectory (bottom view), and from the rear side, along the pellet trajectory (back view). The exposure duration was 5 μs.

The experiments yielded a base of instantaneous photographs of about thirty discharges. A cloud typically appears as an ellipsoid elongated in the direction of magnetic field. Depending on the local plasma parameters, the cloud dimensions and the degree of elongations varied within broad limits: the cloud size along the field was 0.8–3.0 cm, and that in the transverse direction, 0.5–1.5 cm.

Let us consider peculiarities of the cloud structure observed in the typical shot #49982 (Fig. 1). In the photographs presented in Figs. 1a and 1b, the magnetic
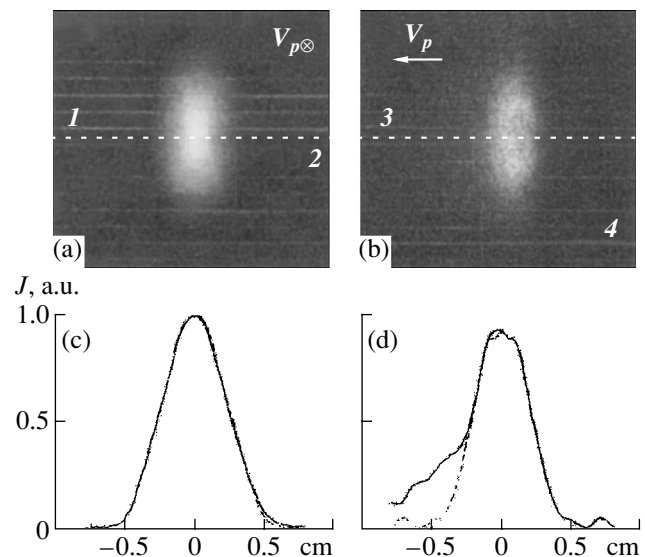

Fig. 1. Typical photographs of a cloud: (a) bottom view; (b) back view; (*1*) top; (*2*) bottom; (*3*) center; (*4*) periphery; (c, d) the corresponding projected intensity profiles for the central part of the cloud (shot #49982).

field is directed bottom to top and the pellet velocity vector is indicated by the arrow (the pellet is situated at the center of the cloud). Note that the cloud appears as symmetric in the back view (Fig. 1a), whereas the bottom view reveals a certain asymmetry relative to the center. This asymmetry is more clearly manifested by the intensity profile in Fig. 1d, where the dashed line (drawn for illustration) represents the mirror-symmetric case. In the intensity profile corresponding to the back view (Fig. 1c), the asymmetry is manifested as well, although it is much less pronounced than in the back view. This cloud structure is typical: it was observed for a number of shots and was more pronounced for greater clouds. The asymmetry observed in the radial direction can be explained neither by special features of the detection system geometry nor by bending of the cloud together with the magnetic surface. This asymmetry is indicative of a radial drift in the secondary cloud plasma toward the center of the plasma.

For a deeper insight into this phenomenon, it was of interest to study the three-dimensional (3D) pattern of the emission intensity distribution over the cloud of evaporated matter. Using well-developed tomographic methods, it is possible to judge the 3D distribution of emission sources by analyzing the corresponding projections [4]. However, tomographic techniques were not used in the analysis of pellet clouds.

The snap-shots obtained using CCD cameras represent projections of the emission from plasma in the corresponding directions. A significant simplification admitted by the given system consists in the 3D to 2D problem reduction by studying N cross sections selected in the direction of magnetic field B. The 2D arrays of emission intensity monitored from two directions must be represented by N pairs of vectors determining the intensity distribution in the corresponding planes. Taking into account that the asymmetry is small, we can use the model of distribution reconstructed in the form of a system of deformed circles [5]. In this case, the local emission intensity is expressed as

$$g(r, \theta) = g_0(r) + rg_1(r)\sin\theta + rg_2(r)\cos\theta, \quad (1)$$

where $g_0(r)$ describes a system of isolines in the form of concentric circles; $g_1(r)$ and $g_2(r)$ are the projections of perturbations on the x and y axes, respectively (for detail, see [5, 6]).

Figure 2 shows an example of reconstructed intensity distribution in the cloud cross section in the direction across the magnetic field. The image corresponds approximately to the middle of the cloud in the direction of the magnetic field. The parameters of plasma in this shot were as follows: central electron temperature, $T_e(0) = 2.6$ keV; central electron density, $n_e(0) = 2 \times$
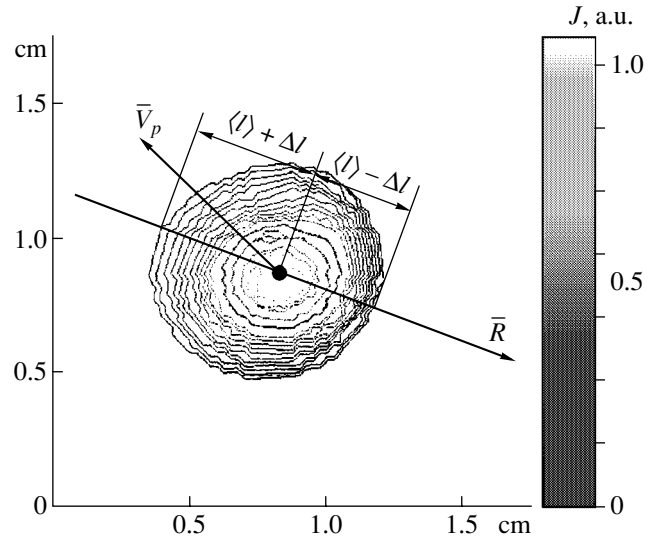

Fig. 2. Typical reconstructed intensity distribution in the central cross section of a cloud (shot #49982).

10^{13} cm^{-3}; ECR heating power, $R_{ECRH} = 900$ kW. The spherical pellet with a diameter of $d_p = 0.4$ mm was injected at a velocity of $V_p = 250$ m/s. In Fig. 2, the magnetic field lines are perpendicular to the figure plane. The directions of the pellet velocity and the large radius of the setup are indicated by arrows.

As can be seen from the reconstructed pattern of the emission distribution, the cloud is spatially asymmetric. The asymmetry is most pronounced for the isolines of low intensity (below 10% of maximum). The cloud is asymmetric in the direction of large radius, being elongated toward high-field side. The characteristic structure does not change from one to another cross section along the magnetic field direction.

Based on the analysis of the emission intensity distribution, one can estimate the drift velocity by the formula

$$V_{dr} \sim \frac{\Delta l}{\langle l \rangle} \frac{\langle l \rangle}{\tau_{ion}}, \quad (2)$$

where $\Delta l \cong 0.06$ cm is the difference of cloud dimensions along and across the large radius, $\langle l \rangle \cong 0.14$ cm is the average cloud size across the magnetic field, $\langle l \rangle/\tau_{ion}$ is the velocity of cloud expansion across the magnetic field state, and $\tau_{ion} \cong 2$ μs is the time of carbon ionization to C^{2+} [7]. The resulting evaluation of the drift velocity is ~300 m/s. The drift direction differs from that observed in the experiments on ASDEX Upgrade tokamak [8], where the plasma of the hydrogen pellet cloud drifts toward low-field side. The physical mechanisms of the observed phenomenon are still unclear.

REFERENCES

1. B. V. Kuteev, P. T. Lang, S. Sudo, *et al.*, Fusion Technol. **26**, 938 (1994).

2. S. M. Egorov, B. V. Kuteev, and V. A. Rozhanskiĭ, Pis'ma Zh. Tekh. Fiz. **13**, 569 (1987) [Sov. Tech. Phys. Lett. **13**, 235 (1987)].

3. L. Ledl, R. Burhenn, V. Sergeev, *et al.*, Earth Planet. Sci. **23J**, 1477 (1999).

4. V. V. Pikalov and T. S. Mel'nikova, *Plasma Tomography* (Nauka, Novosibirsk, 1995).

5. V. V. Pikalov and N. G. Preobrazhenskiĭ, *Reconstructive Tomography in Plasma Gasdynamics and Physics* (Nauka, Novosibirsk, 1987).

6. B. V. Kuteev and M. V. Ovsishcher, Earth Planet. Sci. **4**, 241 (1991).

7. K. L. Bell *et al.*, J. Phys. Chem. Ref. Data, No. 12, 891 (1983).

8. H. W. Muller, K. Buchl, M. Kaufmann, *et al.*, Phys. Rev. Lett. **83**, 2199 (1999).

Translated by P. Pozdeev

Elementary Processes Involved in the Interaction of a Solid with a Bunch of Active Gas Particles

V. F. Kharlamov, I. A. Makushev, A. V. Barmin, T. S. Rogozhina, K. M. Anufriev, and M. I. Bykovskiĭ

Orel State Technical University, Orel, Russia
e-mail: khar@ostu.ru
Revised manuscript received November 13, 2002

Abstract—We propose a new method for investigating processes at the solid–gas interface, which is based on the interaction of the solid surface with a bunch of active species carried by a gas. Using this method, the radical recombination luminescence (RRL) kinetics in crystalline phosphors (CaO–Mn, ZnS–Tm, and ZnS–Cu) excited by a bunch of hydrogen atoms was studied during a time interval of 0.1 s at a temporal resolution of 10 ms. From these RRL measurements, data on the stages of the heterogeneous reaction $H + H \longrightarrow H_2$ were obtained. It was found that the RRL intensity of a ZnS–Cu phosphor decreases with increasing surface electron excitation level. The phenomenon of the total light yield accumulation in ZnS–Cu was observed, which is explained by ionization of the surface electron states. © *2003 MAIK "Nauka/Interperiodica"*.

The mechanisms of heterogeneous chemical processes are conventionally studied by admitting a gas mixture into an evacuated reactor chamber with a given catalyst and monitoring the reaction kinetics. The temporal resolution of this method, based essentially on the relaxation measurements, is determined by the characteristic time of the buildup of the concentration of active particles in the gas phase over the solid surface and typically amounts to $\Delta t = 2.5$ s [1]. In this letter, we propose a new technique that improves the temporal resolution by at least two orders of magnitude.

Consider a reactor through which a gas mixture is continuously pumped under a pressure of P_1, and let an additional portion (bunch) of reactive molecules from a supplementary volume with a pressure of P_2 ($P_2 > P_1$) to be introduced into the gas flow. For the time τ during which the bunch travels from the supplementary volume to the sample, the diffusion spreading of this bunch in the gas flow can be estimated using the following formula:

$$n(\tau)n_0^{-1} = \Phi[L(D\tau)^{-1/2}].$$

Here, n_0 is the initial concentration of molecules in the bunch, $n(\tau)$ is the concentration of these molecules at the time τ, Φ is the probability integral, D is the coefficient of diffusion in the gas flow, $L = vt_g$ is the initial bunch size, v is the gas flow velocity, and t_g is the time during which the additional portion is introduced into the flow. For example, at a gas flow rate of $v \geq 10$ m/s, we have $\tau \leq 10^{-2}$–10^{-1} s. Assuming that $L \geq 1$ m, we obtain $n(\tau)/n_0 \approx 1$, which implies that the diffusion spreading of the bunch is negligibly small. For a bunch interacting with a solid surface, the temporal resolution

Δt of the proposed method of relaxation measurements, as determined by the buildup of the concentration of molecules over the catalyst surface, is determined by the conditions of the bunch formation.

In our experiments, a gas (hydrogen with an impurity content of 5×10^{-3}%) was continuously pumped at a pressure of 70 Pa trough a setup (Fig. 1) comprising discharge tube *1*, capillary *2*, discharge tube *3*, and reactor *4* containing sample *5* deposited onto a metal substrate. The substrate can be heated by passing an
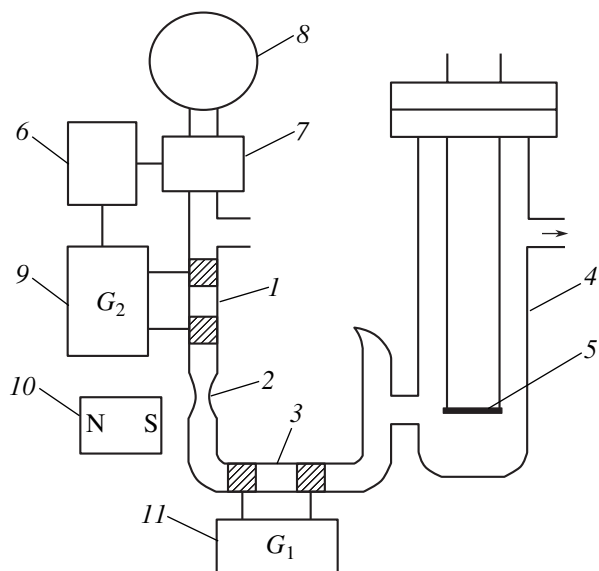

Fig. 1. Schematic diagram of the experimental setup (see the text for explanations).
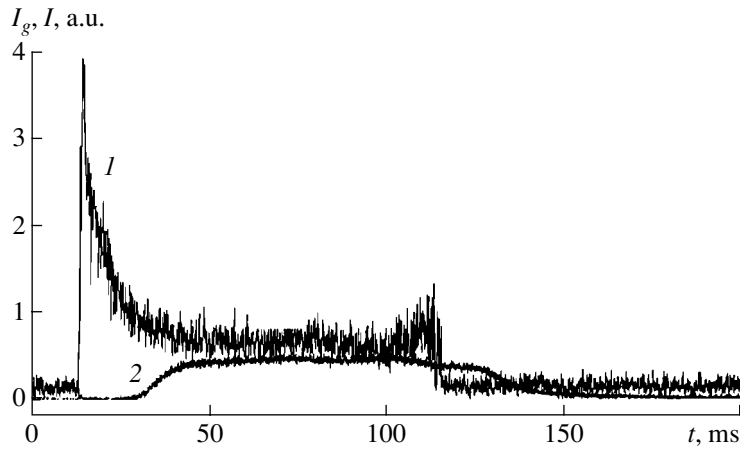
Fig. 2. Time variation of (*1*) the intensity of emission from atomic hydrogen in the discharge tube and (*2*) the RRL intensity of a CaO–Mn phosphor at $T = 509$ K under the action of an atomic hydrogen bunch with $n \approx 10^{15}$ cm^{-3}.

electric current, and the temperature can be measured with a thermocouple. An electronic control device *6* generated a current pulse that opened electromagnetic valve *7* for a period of 0.8 s, during which an additional portion of a gas was admitted into the system from supplementary volume *8* filled with hydrogen at a pressure of 10^4 Pa. Simultaneously, the control device *6* generated a rectangular voltage pulse (with a duration controlled from 20 to 200 ms) applied to the control grid of an electron tube of a high-frequency oscillator *9*. The oscillator generated a pulse of sinusoidal voltage with a frequency of 40 MHz, which initiated a pulsed capacitive gas discharge of controlled power (0.05–1 kW) in tube *1*. This discharge produced dissociation of H$_2$ molecules, thus forming a bunch of hydrogen atoms. Capillary *2* and magnet *10* are necessary for bounding the discharge. During the diffusion from discharge tube *1* to reactor *4*, the excited particles (having traveled a distance of $l = 1$ m) participated in $\sim 10^4$ collisions in the gas phase, lost the excess energy, and passed into ground electron and vibrational states. In order to determine the concentration of hydrogen atoms in the discharge plasma in tube *1* (in relative units, as described in [2]), we measured the intensity I_g of the line with $\lambda = 487$ nm (separated with an UM-2 monochromator) in the emission spectrum of hydrogen.

A fine crystalline phosphor CaO–Mn ($10^{-2}\%$), ZnS–Tm ($10^{-2}\%$), or ZnS–Cu (FKP-03 phosphor) with a specific surface of $S \sim 1$ m^2/g was deposited onto metal substrate *5*. According to the proposed method, we measured the intensity of the radical recombination luminescence (RRL) in the phosphor, induced in the course of the heterogeneous reaction H + H $\longrightarrow$ H$_2$ in the bunch of hydrogen atoms interacting with the sample surface. The RRL intensity I and the intensity of emission I_g from hydrogen atoms in the plasma were measured with the aid of two photomultipliers of the FEU-85A type. The output currents of these photode-

tectors, proportional to I or I_g, were processed by analog-to-digital converters and electronically measured every 12 μs. The data were fed into a computer, which simultaneously measured the kinetic curves of $I(t)$ and $I_g(t)$, where t is the current time. The control experiments were performed using a steady-state flow of hydrogen atoms generated by an RF discharge in tube *3* initiated by 30-W oscillator *11* operating at a frequency of 40 MHz. Measured by a thermal probe, the concentration of hydrogen atoms in this flow over the sample surface was $n = 10^{14}$ cm^{-3}.

The interaction of atomic hydrogen with crystalline phosphors is accompanied by energetic yield of adsorbed molecules and atoms (H$_2$O, O$_2$, CO, O, Na, Ca, Zn) from the sample surface [3–5] and by sputtering components of the phosphor powder [6]. For this reason, each sample prior to measurements was trained at $T = 350$ K in the atmosphere of atomic hydrogen for 2 h. This pretreatment provided for a deep cleaning of the sample surface (similar to the ion etching) and ensured its stability in the atomic hydrogen atmosphere during measurements. Using published data [7, 8], we monitored the state of the sample surface by the RRL intensity, spectrum, and persistence time. The control experiments showed that the interaction of high-density H bunches ($n \approx 10^{15}$ cm^{-3}) with the phosphors studied did not change the state of the sample surface, as was evidenced by the stable characteristics of RRL excited in a steady-state flow of hydrogen ($n = 10^{14}$ cm^{-3}).

The $I(t)$ profile measured during the interaction of a hydrogen bunch with a CaO–Mn phosphor has a nearly rectangular shape (Fig. 2, curve *2*). This $I(t)$ curve is shifted relative to $I_g(t)$ (curve *1*) by a time equal to that required for the H bunch to travel from a discharge tube to the reactor (17 ms). Owing to the relation $I = \eta J(n)$ (where η is a coefficient, J is the heterogeneous reaction rate, and n is the concentration of hydrogen in the gas), the $I(t)$ curve reflects the shape $n(t)$ of the atomic

bunch traveling in the reactor. According to the shape of the front of profile *2*, the temporal resolution of this method is $\Delta t \approx 10$ ms. Under the same conditions, for a constant pressure in the flow of H atoms created after initiation of the steady-state discharge in tube *3*, we obtained $\Delta t = 0.2$ s. This twenty-fold compression of the front of the H bunch is provided by introducing an additional portion (bunch) of hydrogen into discharge tube *1*, which sharply increases the velocity of motion of the atomic-molecular hydrogen mixture.

As the pulsed discharge power increases at a constant pulse duration, the amplitude I_m of the RRL pulse from CaO–Mn as a function of the H bunch density grows approximately by a quadratic law (Fig. 3). The reliability of the $I_m \sim n^2$ approximation, checked by least squares, was $R^2 = 0.72$ (at $T = 345$, curve *1*) and 0.83 (at $T = 518$ K, curve *2*). Depending on the pulsed discharge power, the ratio of I_m to I^* (the intensity of RRL excited for a steady-state hydrogen flow) varied within 2–50. These data indicate that the maximum concentration of hydrogen in the bunch under our experimental conditions reached $n \approx 10^{15}$ cm^{-3}.

An atomic hydrogen bunch contains $N_g = \pi r^2 v t_g n \sim 10^{20}$ atoms ($r = 5$ cm is the radius of a cylindrical reactor, $v = 10^2$ m/s is the gas flow velocity, $t_g = 0.1$ s is the time of bunch passage through the reactor (Fig. 2), and $n \approx 10^{15}$ cm^{-3}). During the time t_g, the number of atoms recombining on the phosphor surface is $N_r = 0.25 n v_a \gamma t_g m S \sim 10^{18}$ ($v_a = 2.5 \times 10^3$ m/s is the average velocity of the thermal motion of H atoms in the medium, $\gamma = 10^{-3}$ is the heterogeneous recombination of the surface of ZnS and CaO based phosphors [9], and $m = 10^{-2}$ g is the amount of phosphor deposited onto the substrate). The number of hydrogen atoms chemisorbed on the phosphor surface over the time t_g is $N_a \approx 0.25 n v_a t_g m S \alpha$ (α is the sticking coefficient for the chemisorption of atomic hydrogen). For the CaO–Mn and ZnS–Cu(Co, Cl) phosphors with the same prehistory (the same pretreatment in atomic hydrogen), it was reported (for $T = 295$ K and $n = 5 \times 10^{13}$ cm^{-3}) that $\alpha = 3 \times 10^{-5}$ for CaO and $\alpha = 10^{-6}$ for ZnS [6]. Using these values, we obtain an estimate of $N_a \sim 10^{15}$–10^{16}. Note that the inequality $N_a + N_r \ll N_g$ is valid. Therefore, the process of atomic hydrogen adsorption and recombination on the sample surface does not significantly change the density of H atoms in the gas medium.

According to the results of adsorption measurements performed using the piezoquartz microbalance technique [10], the interaction of an H bunch with the CaO–Mn surface leads to an increase in the concentration of chemisorbed atoms (the maximum surface coverage amounts to $N_{\max} \approx 0.25 n v_a t_g \alpha \sim 10^{14}$ cm^{-2}). If the chemisorbed hydrogen atoms were participating in the heterogeneous recombination process responsible for the RRL excitation (via Eley–Rideal or Langmuir–Hinschelwood mechanisms), we could expect that $I \approx Bt +$
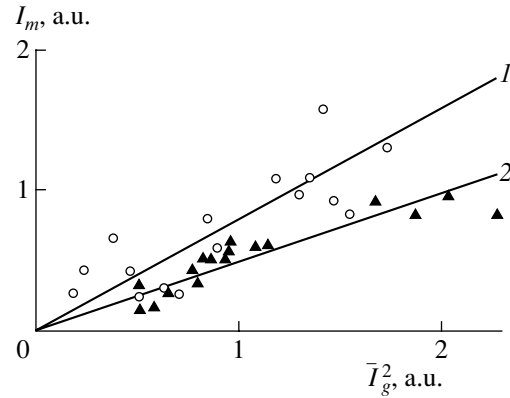

Fig. 3. Plots of the amplitude I_m of the RRL pulse from a CaO–Mn phosphor at $T = 345$ (*1*) and 518 K (*2*) versus the square value of I_g (averaged over the discharge time).

Ct^2, where $I = \eta J = anN + bN^2$, $N \sim t$, and B, C, a, and b are coefficients. However, this condition is not satisfied (Fig. 2); moreover, the rectangular shape of the $I(t)$ profile is retained for various densities of H bunches, $n = 10^{14}$–10^{15} cm^{-3}. Since the rate of a reaction responsible for the RRL excitation is independent of the concentration of chemisorbed atoms, the process must proceed via the recombination of physically adsorbed hydrogen atoms [10]. Validity of the condition $I_m \sim n^2$ (Fig. 3) implies that the rate of desorption of the physically adsorbed atoms is high as compared to the rate of their mutual recombination.

The RRL of a ZnS–Cu phosphor observed as small H bunch densities exhibits the same behavior as that observed for the CaO–Mn system. However, as the atomic hydrogen concentration n becomes large, the interaction of H bunches with ZnS–Cu gives rise to two emission peaks: the first peak (RRL) appears when the bunch enters the reactor and the other peak (afterglow) arises when the bunch leaves the reactor. A decrease in the gas flow rate leads to an increase in the full width at half maximum (FWHM) of these peaks. With increasing temperature of the phosphor (within 295 K $\leq T \leq$ 473 K), the former peak (RRL) shifts rightward (increasing delay relative to the pulsed discharge initiation) and the FWHM grows. The second peak shifts leftward and its FWHM decreases (Fig. 4). No such peculiarities in the $I(t)$ curves were observed for CaO–Mn and ZnS–Tm phosphors studied under the same conditions. When an H bunch is added to a steady-state flow of atomic hydrogen, the RRL intensity of ZnS–Cu decreases, while that of ZnS–Tm and CaO–Mn phosphors increases (during the bunch passage through the reactor).

The above results can be interpreted as follows. The RRL excitation by H atoms in zinc sulfide phosphors proceeds according to the electron–hole pair injection from the surface to bulk of the solid [8]. The heterogeneous reaction H + H $\longrightarrow$ H$_2$ is also accompanied by

I_g, I, a.u.
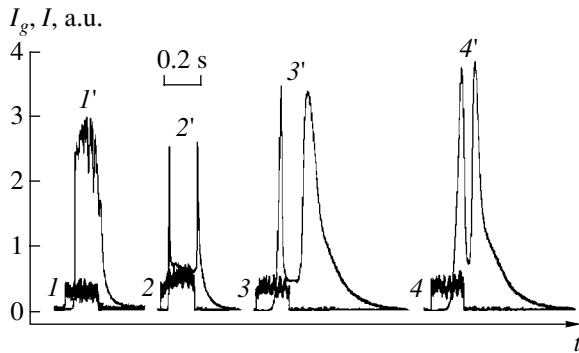

0.2 s

Fig. 4. Time variation of (*1–4*) the intensity of emission from atomic hydrogen in the discharge tube at $P_2 = 10^4$ (*1, 2*) and 7×10^3 Pa (*3, 4*) and (*1'–4'*) the RRL intensity of a ZnS–Cu phosphor under the action of an atomic hydrogen bunch of (*1'*) small and (*2'–4'*) large density at $T = 295$ (*1'–3'*) and 473 K (*4'*).

the appearance of a positive surface charge due to ionization of the surface electron states in the course of this interaction [11, 12]. The surface charging leads to the formation of a potential barrier for electrons diffusing from the surface into bulk upon the RRL excitation. This results in an increasing rate of the nonradiative electron–hole recombination on the surface defects of the crystal lattice. The probability of a conduction electron surmounting the potential barrier and diffusing from the surface into bulk exponentially decreases with increasing surface charge. Instead, an increasing electron excitation level at the surface leads to a superlinear growth in intensity of the nonradiative electron–hole recombination on the surface, which results in the rapid RRL quenching after the first pulse of emission from the phosphor. This is also accompanied by a total light yield stored in the form of bulk charges representing the barrier-separated electrons and holes, which accounts for the afterglow pulse. The total light yield nonlinearly depends on the surface charge determining the nonradiative electron–hole recombination probability (Fig. 4). The photoexcited samples of FKP-03 phosphor exhibited prolonged afterglow due to the presence of bulk electron traps situated 0.18, 0.26, and 0.4 eV above the conduction band bottom [7]. By trapping electrons, these centers hinder neutralization of the positive surface charge, thus providing for the appearance of phenomena described above. In the ZnS–Tm and CaO–Mn phosphors, containing no such traps, the surface charge formed under the same conditions is neutralized by the conduction electrons and, hence, no nonlinear effects take place during the RRL excitation.

Thus, the proposed method of monitoring, based on the interaction of a bunch of active species with the sold surface, provides information both about the mechanism of a heterogeneous chemical reaction and about the accompanying electron processes on the surface.

REFERENCES

1. S. L. Kiperman and N. A. Gaĭdaĭ, Kinet. Katal. **40**, 705 (1999).

2. V. V. Zaĭtsev, Opt. Spektrosk. **72** (4), 859 (1992) [Opt. Spectrosc. **72**, 462 (1992)].

3. L. Yu. Frolenkova, V. F. Kharlamov, T. S. Rogozhina, *et al.*, Kondens. Sredy Mezhfazn. Gran. **3** (1), 49 (2001).

4. V. F. Kharlamov, L. Yu. Frolenkova, and T. S. Rogozhina, Zh. Tekh. Fiz. **71** (10), 90 (2001) [Tech. Phys. **46**, 1294 (2001)].

5. V. F. Kharlamov, Izv. Vyssh. Uchebn. Zaved., Fiz., No. 2, 125 (1977).

6. Sh. L. Izmaĭlov and V. F. Kharlamov, Kinet. Katal. **23**, 1179 (1982).

7. F. F. Vol'kenshteĭn, A. N. Gorban', and V. A. Sokolov, *Radical Recombination Luminescence of Semiconductors* (Nauka, Moscow, 1976).

8. M. D. Nurzhanov and V. F. Kharlamov, Zh. Prikl. Spektrosk. **38**, 585 (1983).

9. V. V. Styrov, Kinet. Katal. **9**, 124 (1968).

10. V. F. Kharlamov, T. S. Rogozhina, A. V. Barmin, *et al.*, Pis'ma Zh. Tekh. Fiz. **28** (13), 67 (2002) [Tech. Phys. Lett. **28**, 564 (2002)].

11. V. F. Kharlamov, Kinet. Katal. **20**, 946 (1979).

12. V. V. Styrov and V. M. Tolmachev, Dokl. Akad. Nauk SSSR **218**, 1150 (1974).

Translated by P. Pozdeev

On the Internal Nonlinear Resonance of Capillary-Gravitational Waves on the Charged Surface of a Deep Viscous Liquid

D. F. Belonozhko and A. I. Grigor'ev*

Yaroslavl State University, Yaroslavl, Russia
* e-mail: grig@uniyar.ac.ru
Received September 20, 2002; in final form, December 3, 2002

Abstract—An analytical expression for the profile of a periodic wave of finite amplitude on the surface of a deep viscous conducting liquid is obtained for the first time. The formula admits the transition to a limiting case of the ideal liquid. It is shown that the position of an internal nonlinear resonance of these capillary-gravitational waves depends neither on the medium viscosity nor on the surface charging. It is established that, during the resonance interaction, the energy is pumped from longwave capillary-gravitational oscillations with the wave-number $k_* \equiv \sqrt{\rho g / 2\gamma}$ to shortwave oscillations with $k_0 \equiv \sqrt{2\rho g / \gamma}$. © 2003 MAIK "Nauka/Interperiodica".

Introduction. The investigation of nonlinear waves in a deep viscous liquid provides a key to understanding a number of phenomena important in applications. The existing notions about such phenomena are restricted to information that can be gained within the framework of a linear model of motion of the free liquid surface. These phenomena include instability of the liquid surface with respect to elastic stresses [1] and with respect to inactive surfactants contained in the medium [2] and instability of oscillations of a charged liquid surface at a final rate of the electric charge redistribution on this surface [3]. Since all these phenomena are determined by the balance of viscous stresses on the free surface and stresses of a certain other nature, the behavior of such systems principally cannot be studied using nonviscous liquid approximations.

Recently [4], we proposed the model of a nonlinear periodic wave propagating over the surface of a deep viscous liquid. This letter presents a natural generalization of the model to the case of such a liquid with charged free surface.

Formulation of the problem. Consider an incompressible Newtonian liquid with the density ρ and the kinematic viscosity ν, occupying the half-space $z \leq 0$ of a Cartesian coordinate system $Oxyz$. Let the surface $z = 0$ coincide with the free liquid surface and the Oz axis point upward. The external medium, representing an ideal insulator with a permittivity of ε, produces the pressure p_0 upon the liquid surface. The liquid is ideally conducting and bears a homogeneously distributed surface charge, such that the electric field above a distorted surface tends to homogeneous with the strength $E_0 \mathbf{e}_z$ in the limit of $z \longrightarrow \infty$. Our aim is to describe the profile of a wave propagating over the free liquid surface.

Let $u = u(x, z, t)$ and $v = v(x, z, t)$ be the horizontal and vertical components of the velocity field of the liquid (for simplicity, these fields are assumed to be independent of the y coordinate); $\mathbf{e}_x$ and $\mathbf{e}_z$ will denote the unit vectors of the Ox and Oz axes, respectively. The required analytical expression for the wave profile $\xi = \xi(x, t)$ describing the deviation of the free liquid surface from the equilibrium shape $z = 0$, the velocity field $\mathbf{U} = u\mathbf{e}_x + v\mathbf{e}_z$, and the electric potential Φ over the liquid surface must satisfy the following boundary- and initial-value problem:

$$z > \xi: \ \Delta\Phi = 0;$$

$$z < \xi: \ \partial_t \mathbf{U} + \mathrm{rot}(\mathbf{U}) \times \mathbf{U} = -\mathrm{grad}\left(\frac{p}{\rho} + \frac{U^2}{2} + gz\right) + \nu \cdot \Delta\mathbf{U};$$

$$\mathrm{div}\,\mathbf{U} = 0;$$

$$z = \xi: \ \partial_t \xi + u\partial_x \xi = v;$$

$$p - p_0 - 2\rho\nu\mathbf{n} \cdot ((\mathbf{n} \cdot \nabla)\mathbf{U}) + \frac{\varepsilon}{8\pi}(\nabla\Phi)^2 = \gamma\,\mathrm{div}\,\mathbf{n};$$

$$\boldsymbol{\tau} \cdot ((\mathbf{n} \cdot \nabla)\mathbf{U}) + \mathbf{n} \cdot ((\boldsymbol{\tau} \cdot \nabla)\mathbf{U}) = 0; \quad \Phi = 0;$$

$$z \longrightarrow \infty: \ \nabla\Phi \longrightarrow -\mathbf{E}_0;$$

$$z \longrightarrow -\infty: \ \mathbf{U} \longrightarrow 0;$$

$$t = 0: \ \xi = F(x);$$

$$z \leq \xi: \ \mathbf{U} = \mathbf{U}^0 = \mathbf{U}^0(x, z) = u^0(x, z)\mathbf{e}_x + v^0(x, z)\mathbf{e}_z,$$

where t is the time; p is the pressure inside the liquid; ∂_t and ∂_x denote the derivatives with respect to time and coordinate; and $\boldsymbol{\tau}$ and $\mathbf{n}$ are the unit vectors of the tangent and normal to the surface, respectively.
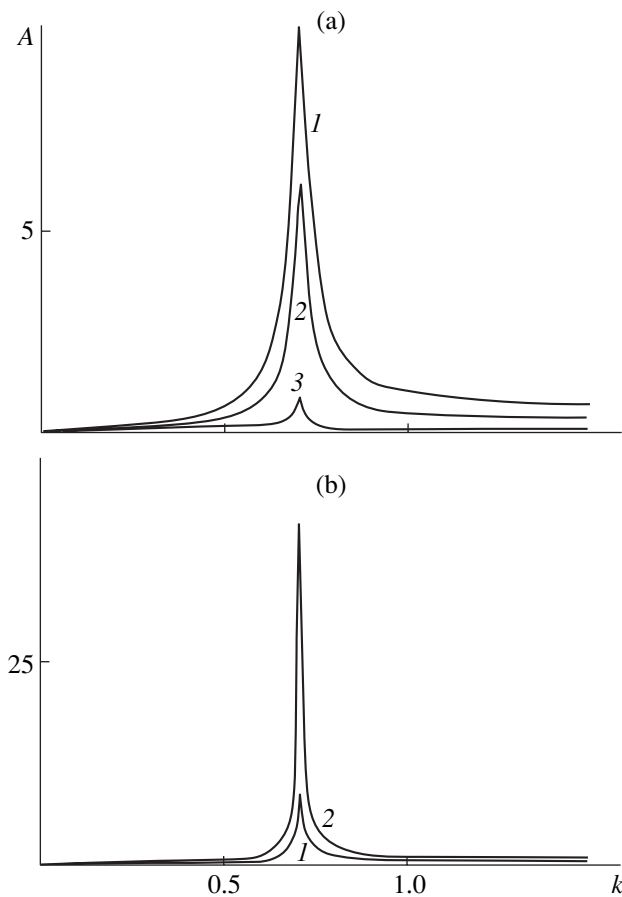
Fig. 1. Plots of the dimensionless amplitude A of the second-order term in the wave profile versus the dimensionless wavenumber k for $\nu = 10^{-2}$ and various values of the parameter W: (a) $W = 0$ (*1*), 0.5 (*2*), and 1 (*3*); (b) $W = 1.5$ (*1*) and 2 (*2*).

Solution of the problem. Previously [4], we determined the shape of a nonlinear capillary-gravitational wave on an uncharged surface of a viscous liquid in the second-order approximation in amplitude. By the same token, we readily obtain the following expression for the profile of a periodic, nonlinear capillary-gravitational wave on the homogeneously charged surface of a deep conducting viscous liquid in the same approximation:

$$\xi = a\cos[\mathrm{Im}(S)t - kx] + a^2(\mathrm{Re}(\Lambda)\cos[2(\mathrm{Im}(S)t - kx)]$$
$$- \mathrm{Im}(\Lambda)\sin[2(\mathrm{Im}(S)t - kx)])\exp[2\mathrm{Re}(S)t]. \quad (1)$$

Here, S is the complex frequency determined by solving the known dispersion equation for capillary-gravitational waves on the charged surface of a viscous liquid [5, 6]; the expression for the coefficient Λ differs from an analogous value obtained in [4] only by a term accounting for the charge on the free liquid surface (this extremely cumbersome formula is not presented here).

An interesting feature of the above expression describing the profile of a periodic, nonlinear capillary-

gravitational wave on the charged surface is that the term quadratic in the wave amplitude has a resonance character. This circumstance is especially clearly manifested upon transition to the ideal liquid ($\nu \longrightarrow 0$), whereby Eq. (1) significantly simplifies to acquire the form

$$\xi = a\cos(kx - \omega_0 t) + a^2 A_0 \cos(2kx - 2\omega_0 t);$$

$$\omega_0^2 = \frac{k}{\rho}\left(\rho g + \gamma k^2 - k\frac{\varepsilon E_0^2}{4\pi}\right); \quad (2)$$

$$A_0 = \frac{k(\rho g + \gamma k^2 - k\varepsilon E_0^2/2\pi)}{2(\rho g - 2\gamma k^2)}.$$

For $E_0 = 0$, this expression coincides with the solution obtained by Nayfeh [7] for the profile of a nonlinear wave on the surface of the ideal uncharged liquid.

As can be seen from expression (2), the term of the second order of smallness added to the wave amplitude has opposite signs for $k < k_* \equiv \sqrt{\rho g/(2\gamma)}$ and $k > k_*$. Indeed, the A_0 value is positive for the long waves with $k < k_*$ (gravitational branch), and it is negative for the short waves with $k > k_*$ (capillary branch). At $k = k_*$, the system exhibits an internal nonlinear resonance of the three-mode interaction of capillary-gravitational waves [4, 5], whereby the amplitude of the second-order term tends to infinity. The behavior of solution (2) near the point $k = k_*$ was thoroughly studied in [7]. An analysis of the wave profile at $k = k_*$ for a charged surface of the deep viscous liquid described by expression (1) showed that the position of this resonance remains unchanged when $\nu \neq 0$, but the amplitude of the second-order additive in the vicinity of the resonance point is finite.

Discussion. Figure 1 shows the absolute value $A = \sqrt{\mathrm{Re}(\Lambda)^2 + \mathrm{Im}(\Lambda)^2}$ of the amplitude of the second-order term in the wave profile (1), plotted in the dimensionless variables ($\rho = \gamma = g = 1$) as a function of the wavenumber k for $\nu = 10^{-2}$ and various values of the Tonks–Frenkel parameter $W = \varepsilon E_0^2/4\pi\sqrt{\rho g\gamma}$. The latter dimensionless quantity characterizes stability of the liquid surface with respect to the surface charge: the surface becomes unstable for $W \geq 2$ [8]. As can be seen, the absolute value of A decreases with increasing W at small values of this parameter ($W < 1$, Fig. 1a) and then rapidly grows with W (for $W > 1$, Fig. 1b). This behavior of the amplitude is also retained for the ideal liquid, as can be readily seen from the analytical expression (2): the coefficient A_0 passes through zero and changes the sign at $W = 1$.

As was noted above, the presence of viscosity and electric charge does not change the position of the internal nonlinear resonance, which is still observed at $k = k_*$ for $\nu \neq 0$ and $W \neq 0$. In the second-order approxima-
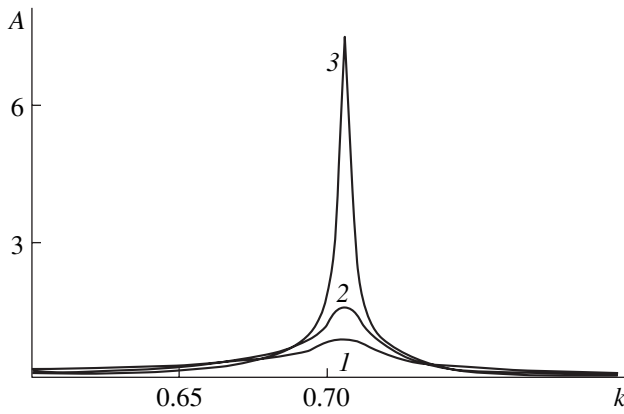
Fig. 2. Plots of A versus k for $W = 1$ and various values of the dimensionless viscosity: $\nu = 10^{-2}$ (*1*), 5×10^{-3} (*2*), and 10^{-3} (*3*).

physical pattern of instability development in the system under study.

Figure 2, plotted in accordance with Eq. (1), illustrates the obvious effect of viscosity on the second-order correction to the wave amplitude.

Conclusion. The position of an internal nonlinear resonance of the capillary-gravitational waves on the free surface of a viscous liquid depends neither on the viscosity of this liquid nor on the presence of charge on the liquid surface. During the resonance interaction of modes, energy is pumped from longwave capillary-gravitational waves with the wavenumber $k_* \equiv \sqrt{\rho g / 2\gamma}$ to shorter waves with $k_0 \equiv \sqrt{2\rho g / \gamma}$.

tion under consideration, by the resonance interaction we imply a three-mode interaction between the three capillary-gravitational waves propagating in the same direction, the wavenumbers and frequencies of which obey the conditions $k_1 + k_2 = k_3$ and $\omega_1 + \omega_2 = \omega_3$ [9] (in the dimensionless variables adopted, $\omega^2 = k + k^3 - Wk^2$). Note that, for the nonlinear capillary-gravitational waves on the charged liquid surface under consideration, the interaction conditions formulated in [9] are satisfied for any values of the parameter W up to the critical level ($W_{cr} = k + k^{-1}$) corresponding to $2k_* = k_0$ and $2\omega_* = \omega_0$. This is the so-called degenerate resonance, whereby a wave with the wavenumber $k_* \equiv \sqrt{\rho g / 2\gamma}$ doubly interacts with and gives energy to the wave with $k_0 \equiv \sqrt{2\rho g / \gamma}$.

The above features in behavior of the capillary-gravitational waves on the charged liquid surface imply, in particular, that the amplitudes of waves exhibiting nonlinear interaction in a small vicinity of the wavenumber $k = k_0$ exceed the amplitudes of waves with $k \ll k_0$ and $k \gg k_0$. According to [10–12], as the electrostatic field strength E_0 at the liquid surface increases, the waves with $k \approx k_0$ become advantageous in realization of the tendency to lose stability with respect to the surface charge (i.e., these waves are characterized by greater increments of instability at the initial time [12]), and, hence, the growth of these waves determines the

REFERENCES

1. S. O. Shiryaeva, A. I. Grigor'ev, and V. A. Koromyslov, Pis'ma Zh. Tekh. Fiz. **22** (4), 89 (1996) [Tech. Phys. Lett. **22**, 173 (1996)].
2. S. O. Shiryaeva, D. F. Belonozhko, and A. I. Grigor'ev, Zh. Tekh. Fiz. **68** (2), 22 (1998) [Tech. Phys. **43**, 151 (1998)].
3. D. F. Belonozhko and A. I. Grigor'ev, Pis'ma Zh. Tekh. Fiz. **25** (22), 1 (1999) [Tech. Phys. Lett. **25**, 884 (1999)].
4. D. F. Belonozhko, A. I. Grigor'ev, and S. O. Shiryaeva, Pis'ma Zh. Tekh. Fiz. **28** (19), 1 (2002) [Tech. Phys. Lett. **28**, 795 (2002)].
5. I. N. Aliev and A. V. Filippov, Magn. Gidrodin., No. 4, 94 (1989).
6. A. I. Grigor'ev, O. A. Grigor'ev, and S. O. Shiryaeva, Zh. Tekh. Fiz. **62** (9), 12 (1992) [Sov. Phys. Tech. Phys. **37**, 904 (1992)].
7. A. H. Nayfeh, J. Fluid Mech. **40**, 671 (1970).
8. Ya. I. Frenkel, Zh. Éksp. Teor. Fiz. **6** (4), 348 (1936).
9. M. O. Phillips, in *Nonlinear Waves*, Ed. by S. Leibovich and A. R. Seebass (Cornell University Press, Ithaca, 1974; Mir, Moscow, 1977).
10. S. O. Shiryaeva, Zh. Tekh. Fiz. **68** (9), 9 (1998) [Tech. Phys. **43**, 1019 (1998)].
11. S. O. Shiryaeva, A. I. Grigor'ev, and D. F. Belonozhko, Zh. Tekh. Fiz. **69** (1), 15 (1999) [Tech. Phys. **44**, 12 (1999)].
12. S. O. Shiryaeva, Zh. Tekh. Fiz. **70** (9), 30 (2000) [Tech. Phys. **45**, 1128 (2000)].

Translated by P. Pozdeev

Mass Transfer and Doping
during Electrolyte–Plasma Treatment of Cast Iron

A. D. Pogrebnjak[a,d,]*, O. P. Kul'ment'eva[a], A. P. Kobzev[b],
Yu. N. Tyurin[c,]**, S. I. Golovenko[c], and A. G. Boiko[a]

[a] *Institute of Surface Modification, Sumy, Ukraine*
* e-mail: apogrebnjak@simp.sumy.ua
[b] *Joint Institute for Nuclear Research, Dubna, Moscow oblast, 141980 Russia*
[c] *Paton Institute of Electric Welding, National Academy of Sciences of Ukraine, Kiev, Ukraine*
** e-mail: ytyurin@paton.kiev.ua
[d] *Sumy State University, Sumy, Ukraine*
Revised manuscript received November 22, 2002

Abstract—The surface and subsurface layers of cast iron articles upon electrolyte–plasma treatment (EPT) were studied for the first time by a combination of methods, including Rutherford backscattering, elastic recoil detection analysis, X-ray diffraction, optical metallography, and microhardness measurements. It was found that tungsten and copper ions are incorporated into the surface layers of the metal. Total thickness of an EPT-hardened layer is about 3 mm, the maximum hardness (up to 7000 MPa) being observed at a depth from 1 to 2.5 mm. The X-ray diffraction analysis (i) shows that the EPT-hardened layer comprises a mixture of α and γ phases, (ii) indicates the formation of a fine-grained martensite structure with high dislocation density (above 10^{12} cm^{-2}) and an oxide (FeO) phase, and (iii) reveals mass transfer involving the doping elements (W and Cu). © 2003 MAIK "Nauka/Interperiodica".

The electrolyte–plasma treatment (EPT) of metals is an effective method of surface hardening now extensively implemented in industry. The main advantages of this process are high efficiency (reaching up to 85%) [1, 2], significant thickness of the hardened layer (up to 10 mm) [2], and relatively simple technology involving no toxic electrolytes and compounds. Despite the wide practical application of EPT, the course of physical processes (such as mass transfer and doping) involved in this treatment are still insufficiently studied. It should be noted that, besides hardening, the EPT technology can be used for the surface cleaning and microoxidation. In recent years, the interest in such applications has considerably increased [1–6].

The EPT technology is based on a high-rate of heating of a metal processed, while the article contacts with an aqueous electrolyte solution and is a cathode or anode relative to this medium. During the EPT process, the metal surface is periodically heated and cooled as a result of variation of the electric potential in the layer of plasma generated between the liquid electrode (electrolyte) and the article surface (e.g., cathode). This is provided by a nozzle with perforated metal grid (anode), having the diameter D_a, placed into the electrolyte (Fig. 1), through which an electrolyte stream of length H is supplied to the surface area processed. In the immediate vicinity of the metal surface, there appears a thin plasma layer (with the thickness h) possessing an increased ohmic resistance. In this layer, the electric

energy supplied is converted into the energy of multiple microarcs [7].

The conductivity of electrolyte between the grid anode and the plasma layer has both electrostatic and hydrodynamic components [8], which reduces the resistive losses (Q_R). The energy is mostly converted into heat, and the plasma layer heats the cathode surface (Q_c). The dissipated energy (Q_d) is low, because the plasma layer thickness h is relatively small as compared to the heated area size determined by the nozzle
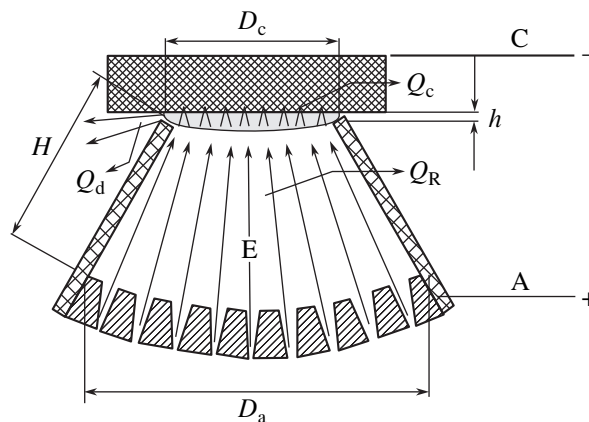

Fig. 1. A schematic diagram of the EPT process and geometry: (A) anode; (C) cathode; (E) electrolyte (see the text for explanations).

output diameter D_c. Depending on the D_a/D_c and h/H ratios and the electrical parameters, the EPT technology allows the surface heating and cooling rates to be controlled within 20–500 K/s. In these regimes, the article surface can be treated at a maximum calculated specific power of 10^3–10^4 W/cm^2.

Our experiments were performed with copper and tungsten anodes. The electrolyte was a 12% aqueous Na_2CO_3 solution. The processed objects represented cast iron sleeves for diesel engines. The treatment was effected on the inner sleeve surface. In the first stage, the sleeves were processed for 10 h in the electrolyte with a copper anode. This treatment was accompanied by partial consumption of the anode material, whereby the anode mass was reduced by 15.6 g. Then a tungsten anode was installed and the treatment was continued by the following scheme. The heating was initiated by applying a potential of 320 V for 3 s, after which the potential was switched to 200 V for 5 s (whereby the specific heating power changed from 1.6×10^4 to 0.6×10^4 W/cm^2). After a 30-s heating with five switching cycles, the electric potential was turned off and the heated metal layer was cooled in the electrolyte flow. After this processing, the cast iron article was cut into pieces, and these samples were characterized by various methods.

The elemental composition of the source layer was studied by methods of Rutherford backscattering (RBS) and proton elastic recoil detection analysis (ERDA). Figures 2 and 3 show typical RBS spectra (measured with helium ions) and ERDA curves, respectively, for the same sample of cast iron upon EPT with changed cathodes. As can be seen, the RBS spectrum (Fig. 2) shows (besides iron) the peaks of tungsten and copper, while the ERDA curve (Fig. 3) reveals the presence of oxygen and carbon (arrows in the figures indicate kinematic limits of the corresponding elements). We have also studied the depth–concentration profiles of all these elements. The results of data processing showed that the uppermost surface layer contains an insignificant amount of W (about 0.3 at. %), while the concentration of Cu reaches 6 at. %. At the same time, the subsurface layer is characterized by a high content of oxygen (about 68 at. %) and a reduced concentration of carbon (4.7 at. %). Note that the oxide layer extends only down to a depth of about 2.5 μm. The content of carbon exhibits rather small variations with depth, being 4.7 at.% near the surface and 4.1 at.% at a depth of 12 μm.

The results of a metallographic examination showed that the EPT-hardened surface layer represents a ferrite–perlite mixture with a large content of cementite. The processed material clearly reveals three regions representing a zone of intense structural transformations, a heat-affected zone, and the substrate. The first zone exhibits a fine-grained martensite structure and shows evidence of the cast iron whitening and the
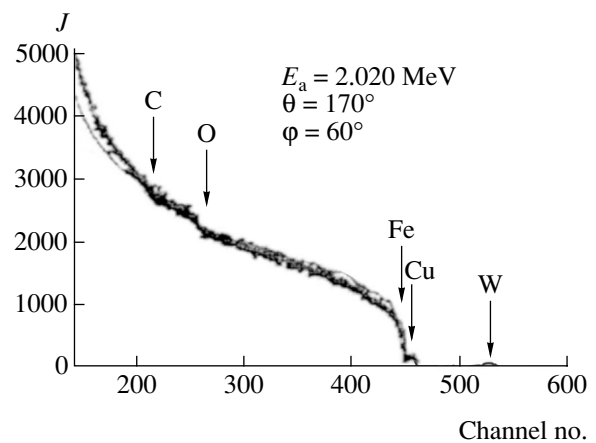

Fig. 2. A typical RBS spectrum of helium ions for a cast iron article upon EPT with changed cathodes.
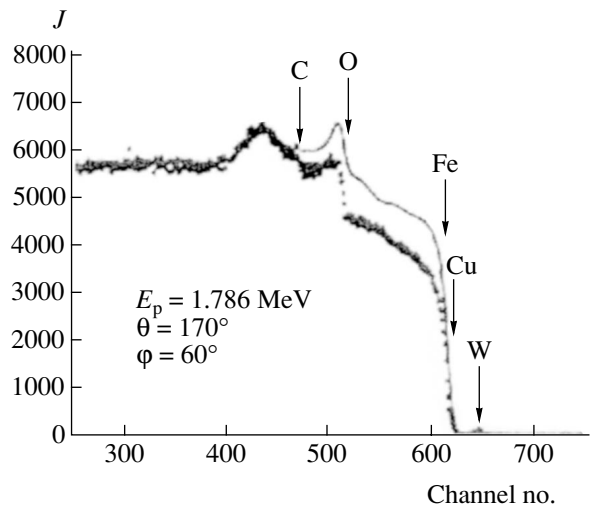

Fig. 3. A proton ERDA spectrum of the same sample as in Fig. 2.

flaked graphite formation. This can be explained by saturation of the material with carbon liberated at elevated temperatures from the electrolyte as a result of Na_2CO_3 decomposition.

An especially important factor determining the character of structural transformations during EPT is the periodic temperature rise (caused by application of an increased potential), whereby the metal is heated above the $\alpha \longrightarrow \gamma$ phase transition temperature (which is on the order of 800°C [9]). Subsequent rapid cooling fixes the iron-based α and γ phases formed in the processed material layer. A transition layer comprises the structures of two types: a fine-grained structure characteristic of the heat-affected zone and a coarse-grained structure typical of the substrate.

The data of X-ray diffraction (XRD) showed (see the table) that, before EPT, the cast iron represented virtually entirely the α phase (ferrite with the lattice

X-ray diffraction parameters of the cast iron samples before and after EPT

Sample state	Phase composition	$\langle a \rangle$, nm	f, %	L_{ev}, Å	ρ, 10^{11} cm^{-2}
Before EPT	α-Fe	0.2867	100	261.2	5.538
After EPT	α-Fe	0.2857	29	128.7	19.65
	γ-Fe	0.3588	11	342	
	Cu	0.3627	46	169.4	
	FeO	0.4295	14	291.2	

parameter $a_{av} = 2.866$ Å, which coincides with the value $a_0 = 2.864$ Å reported for α-Fe [10]). After EPT, the XRD analysis revealed some new phases, including Fe-based γ phase, copper, and FeO. As can be seen from the table, EPT is accompanied by the $\alpha \longrightarrow \gamma$ phase transition. A considerable amount (up to 15%) of FeO can be related to oxidation processes accelerated by the contact with electrolyte heated in the plasma layer.

Figure 4 shows a microhardness profile of a cast iron sample upon EPT. As can be seen from these data, the microhardness in the subsurface layer shows a three-fold increase. The maximum level (7000 MPa) is attained at a depth from 1.2 to 2.5 mm, the total thickness of the hardened layer being about 3 mm. It should be noted that the profile exhibits local minima and maxima, which are probably explained by the presence of fine-grained martensite inclusions and coarse-grained substrate material. This periodicity can be related to the periodic increase and decrease in the heating power during EPT.

The XRD data indicated that EPT leads to a decrease in the grain size and a sharp increase in the density of dislocations (above 10^{12} cm^{-2}), which also favors an increase in the hardness of an EPT-modified surface layer.
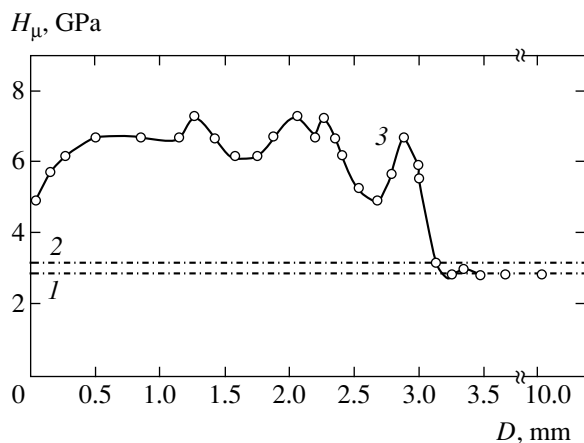
It is worth specially noting that the plasma flow initiates a directed mass transfer of doping elements from both anode and electrolyte, as evidenced by XRD and RBS data. By mass transfer, we imply the directed transport of substance in the external or internal field [11]. In the case under consideration, this transport (directed inward the solid along the electric field lines) involves both heavy (Cu and W) and lighter (C and O) elements. The effects of the heating source and the presence of hydrogen in the boundary layer (not specially studied here) were analyzed in [12]. We believe that the surface mass transfer in the course of EPT proceeds both in the regime of evaporation–condensation and in the form of diffusion in a vapor–plasma layer at the cast iron surface. Estimated from ERDA data, the diffusion coefficients of elements involved in this process amount to 8×10^{-6} cm^2/s (copper) and $\approx 10^{-8}$ cm^2/s (tungsten).

Thus, we have demonstrated that the electrolyte–plasma treatment of cast iron articles produces hardening of the surface layer with a thickness of up to 3 mm. This layer consists of three regions having different structures. The subsurface layer has a fine-grained martensite structure and possesses high microhardness (about three times that of the substrate). In addition to hardening, the surface layer of a cast iron article can be doped with elements of the anode material and with those contained in or added to the electrolyte.

H_μ, GPa

Fig. 4. A typical microhardness–depth profile measured in the cross section of a cast iron article upon EPT: (*1*) perlite (initial sample); (*2*) ferrite (initial sample); (*3*) after EPT.

REFERENCES

1. A. I. Yerokhin, X. Nie, A. Leyland, *et al.*, Surf. Coat. Technol. **122**, 73 (1999).

2. Yu. N. Tyurin and A. D. Pogrebnjak, Surf. Coat. Technol. **142**–**144**, 293 (2001).

3. Yu. N. Tyurin and A. D. Pogrebnjak, in *Trudy OTTOM 2000* (Kharkov. Fiz.-Tekhn. Inst., Kharkov, 2000), pp. 87–95.

4. Yu. N. Tyurin and A. D. Pogrebnjak, Zh. Tekh. Fiz. **72** (11), 119 (2002) [Tech. Phys. **47**, 1463 (2002)].

5. Ya. Z. Yasnegorodskiǐ, *Automatic Heating in Electrolyte* (Oborongiz, Moscow, 1947).

6. G. A. Ostroumov, *Interaction of Electric and Hydrodynamic Fields* (Nauka, Moscow, 1979).

7. Yu. P. Raizer, *The Physics of Gas Discharge* (Fizmatlit, Moscow, 1992).

8. K. N. Eretnev and S. V. Lebedev, *Heating and Cleaning of Metal Surfaces in Electrolyte: Practical Application* (Lipetsk, 1997).

9. V. K. Fedyukin, *Thermocyclic Processing of Steel and Cast Iron* (St. Petersburg, 1997).

10. S. S. Gorelik, L. N. Rastorguev, and Yu. A. Skakov, *X-ray Diffraction and Metallographic Analysis: Applications* (Metallurgiya, Moscow, 1970).

11. *Solid State Physics: Encyclopedic Dictionary*, Ed. by V. G. Bar'yakhtar (Naukova Dumka, Kiev, 1996), Vol. 1, p. 531.

12. V. G. Bar'yakhtar, Yu. M. Buravlev, V. P. Shevchenko, *et al.*, in *Trudy OTTOM 2000* (Kharkov. Fiz.-Tekhn. Inst., Kharkov, 2000), pp. 155–161.

Translated by P. Pozdeev

Predicting the Piezoelectric Response
of Novel Anisotropic 1–2 Type Composites

S. V. Glushanin and V. Yu. Topolov*

Rostov State University, Rostov-on-Don, Russia

* e-mail: topolov@phys.rsu.ru

Received November 22, 2002

Abstract—A model of the 1–2 type piezoelectric composite comprising zig-zag ferroelectric piezoactive ceramic inclusions in a passive polymer matrix is proposed. The orientational and concentrational profiles of the piezoelectric coefficients d_{3j}^* and g_{3j}^*, calculated for various sets of parameters characterizing the composite microstructure are presented. It is demonstrated that the proposed microstructure favors nonmonotonic and alternating-sign behavior of d_{3j}^* and g_{3j}^*. Therefore, the piezoelectric anisotropy and sensitivity of the given 1−2 type composite can be varied within broad limits. © 2003 MAIK "Nauka/Interperiodica".

Progress in the physics of active dielectrics requires the development of methods for creating new heterogeneous materials with desired parameters. An important place belongs to piezoelectric composites, which are more effective than numerous ferroelectric piezoactive ceramic (FEPC) crystals [1, 2]. The piezoelectric composites find application in acoustics, solid state electronics, piezoelectric technology, and medical equipment. One of the main advantages of two-component piezoceramic composites is their high piezoelectric sensitivity, which was studied for materials of the connectivity types 1–3 [3–7], 2–2 [8], and 1–1 [9]. As for the efficiency of 1–2 type materials, the question is still open because of (i) the variety of the possible schemes [11, 12] of the continuous distribution of components in one or two axes of the rectangular coordinate system $(X_1 X_2 X_3)$ and (ii) the complexity of the corresponding procedures used for averaging the physical properties of components with allowance for their physicomechanical interaction.

The purpose of this study was to analyze features of the piezoelectric response and determine advantages of the 1–2 type FEPC based composites.

The idea of using 1–2 type piezoelectric composites with zig-zag FEPC elements is related to the wide occurrence of zig-zag domain walls in ferroelectric and analogous crystals (e.g., of the $Gd_2(MoO_4)_3$ type), which are used as elements in various acoustoelectronic and electromechanical devices [13]. It is important to note that recently [6, 7] 1–2 type piezoelectric composites were used to study the role of rodlike FEPC inclusions oriented at various angles with respect to the polarization axis.

The proposed 1–2 type piezoelectric composite comprises FEPC plates dispersed in a polymer matrix so that their planes (parallel to the OX_2 axis) are rotated clockwise or counterclockwise by an angle φ relative to the polarization axis (OX_3), thus forming a zig-zag pattern (Fig. 1). The volume concentration of FEPC plates $t = |OA|/|OB| = |LR|/|LP|$ varies so as to obey the condition $|KM| < |KN|$, which implies that the polymer component is continuous (doubly connected) in the MN interval along the OX_2 and OX_3 axes, while the FEPC component is continuous (singly connected) in the KM interval along the OX_2 axis. For equal thicknesses of the layers with the plates rotated by the angle $\pm\varphi$ ($|OK| < |KL|$), the volume concentration of FEPC satisfies the condition

$$0 < t < 1 - 0.5\cot\varphi. \tag{1}$$

Violation of condition (1) in the region of $t < 1$ leads to the 1–1 type connectivity. Note that, in contrast to other piezoelectric composites of the 1–β types [3–7, 9, 10, 12], the parameters of microstructure of the system under consideration are determined by the rotation angle varied within the interval $\text{arccot}2 < \varphi < 90°$.

In order to determine the effective elastic, piezoelectric, and dielectric properties of the proposed 1–2 type piezoelectric composite, we will first average the electromechanical constants of the components with respect to concentration t and then average the electromechanical constants of layers of the $KLPN$ and $OKNB$ types with equal thicknesses $|OK| = |KL|$ (Fig. 1). For each separate layer with a connectivity of the 2–2 type, the averaging can be performed as described in [14] using a rotated coordinate system $(X_1' X_2' X_3')$ or $(X_1'' X_2'' X_3'')$, where $OX_3' \perp LS$ and $OX_3'' \perp OS$. The boundary conditions for the electric and mechanical fields [8, 14] are set at $x_3' = $ const (for layers of the $KLPN$ type) and at $x_3'' = $ const (for layers of the $OKNB$
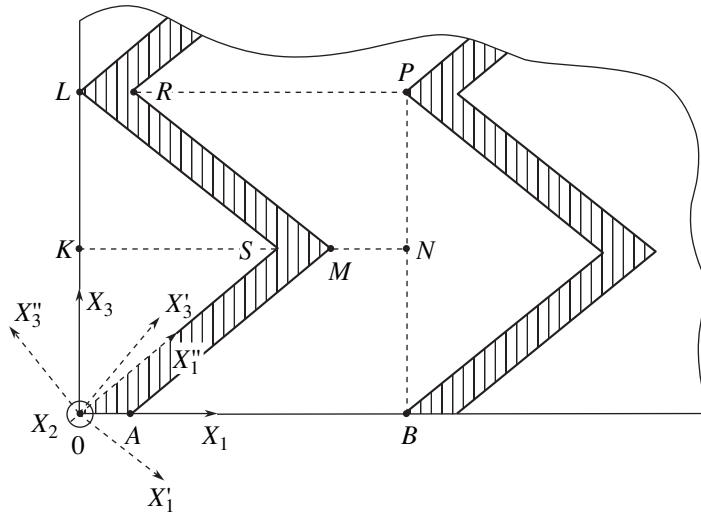
Fig. 1. A schematic diagram showing the cross section of a 1–2 piezoelectric composite structure with the X_1OX_3 plane. Cross-hatched regions indicate the FEPC plates ($\angle KSL = \angle KSO = \varphi$ is the angle of rotation; $|OB| = |OL|$ is the identity period of the composite structure).

type). The obtained sets of electromechanical constants of these layers are averaged with respect to the sample thickness with an allowance for the boundary condition at $x_3 =$ const. As a result, all components of the tensors of elastic compliance (s_{ab}^{*E}), piezoelectric moduli (d_{ij}^{*}), and permittivity ($\varepsilon_{pp}^{*\sigma}$) for 1–2 piezoelectric composites of the FEPC–polymer type are determined in the $(X_1X_2X_3)$ coordinate system as functions of the set of parameters (φ, t).

An analysis of the orientational and concentrational profiles of the effective electromechanical properties calculated as described above shows that the 1–2 type piezoelectric composite structure presented in Fig. 1 belongs to the point symmetry group $mm2$. This implies that the composite is characterized by nonzero piezoelectric coefficients $d_{3j}^{*}(\varphi, t)$, $e_{3j}^{*}(\varphi, t)$, $g_{3j}^{*}(\varphi, t)$, and $h_{3j}^{*}(\varphi, t)$ along the polarization axis OX_3 ($j = 1, 2, 3$). Figure 2 shows the plots of $d_{31}^{*}(\varphi, t)$ and $g_{3j}^{*}(\varphi, t)$ calculated using the room temperature electromechanical constants of a FEPC [PKR-7M ceramics based on Pb(Zr, Ti)O$_3$ (PZT)] and a polymer matrix (araldite) [15]; $d_{3j}^{*}(\varphi, t)$ with $j = 2$ and 3 can be determined using the relation $d_{3j}^{*} = g_{3j}^{*}d_{31}^{*}/g_{31}^{*}$.

A special feature of the electromechanical characteristics of the 1–2 piezoelectric composites is their nonmonotonic and alternating-sign behavior (Figs. 2a, 2b, 2d). Using the equalities $g_{31}^{*} = 0$, $g_{33}^{*} = 0$ or $d_{31}^{*} = 0$, $d_{33}^{*} = 0$ (related to a certain orientation of FEPC plates relative to the OX_3 axis and to the influence of the polymer component on the internal field along the OX_1 axis), it is possible to vary the piezoelectric anisotropy

$g_{33}^{*}/g_{31}^{*} = d_{33}^{*}/d_{31}^{*}$ within broad limits by means of rather small changes in the parameters (φ, t) at a relatively small anisotropy in the piezoelectric moduli of PKR-7M ($d_{33}/d_{31} \approx -2$) [15]. On the other hand, the condition $\mathrm{sgn}\,d_{32}^{*} = \mathrm{sgn}\,g_{32}^{*} < 0$ in the entire range of parameters (φ, t) (Fig. 2c) is explained by continuity of the FEPC component along the OX_2 axis. For $\varphi \gtrsim 58°$, $\mathrm{sgn}\,d_{31}^{*} = \mathrm{sgn}\,d_{31} < 0$ and $\mathrm{sgn}\,g_{33}^{*} = \mathrm{sgn}\,g_{33} > 0$, irrespective of t. In this respect, the given 1–2 piezoelectric composite is close to the PZT-based 2–2 type composite studied by Grekhov *et al.* [8].

The behavior of piezoelectric coefficients $g_{3j}^{*}(\varphi, t) = d_{3j}^{*}(\varphi, t)/\varepsilon_{33}^{*\sigma}(\varphi, t)$ is strongly affected by the orientation of the FEPC plates. Variation of the plate rotation angle φ leads to significant changes the local values of $\max[g_{3j}^{*}(\varphi, t)]$ ($j = 1, 3$) and $\min[g_{32}^{*}(\varphi, t)]$ within a narrow concentration interval $0 < t < 0.1$ (Figs. 2b–2d). For $t \ll 1$, the permittivity $\varepsilon_{33}^{*\sigma}$ of the piezoelectric composite is one to three orders of magnitude lower than that ($\varepsilon_{33}^{\sigma}$) of FEPC, while the moduli of derivatives $|\partial d_{3j}^{*}/\partial t|$ reach maximum values. In addition, an increase in the angle φ most significantly influences the piezoelectric coefficient $g_{31}^{*}(\varphi, t)$ (Fig. 2b), which is related both to the action of the polymer component and to a change in the balance between d_{3j} values of the FEPC component. This balance plays a determining role in the behavior of $d_{3j}^{*}(\varphi, t)$ and can lead to various combinations of the piezoelectric coefficients (e.g., $\mathrm{sgn}\,g_{31}^{*} = -\mathrm{sgn}\,g_{32}^{*} = -\mathrm{sgn}\,g_{33}^{*} > 0$ or $\mathrm{sgn}\,g_{31}^{*} = $
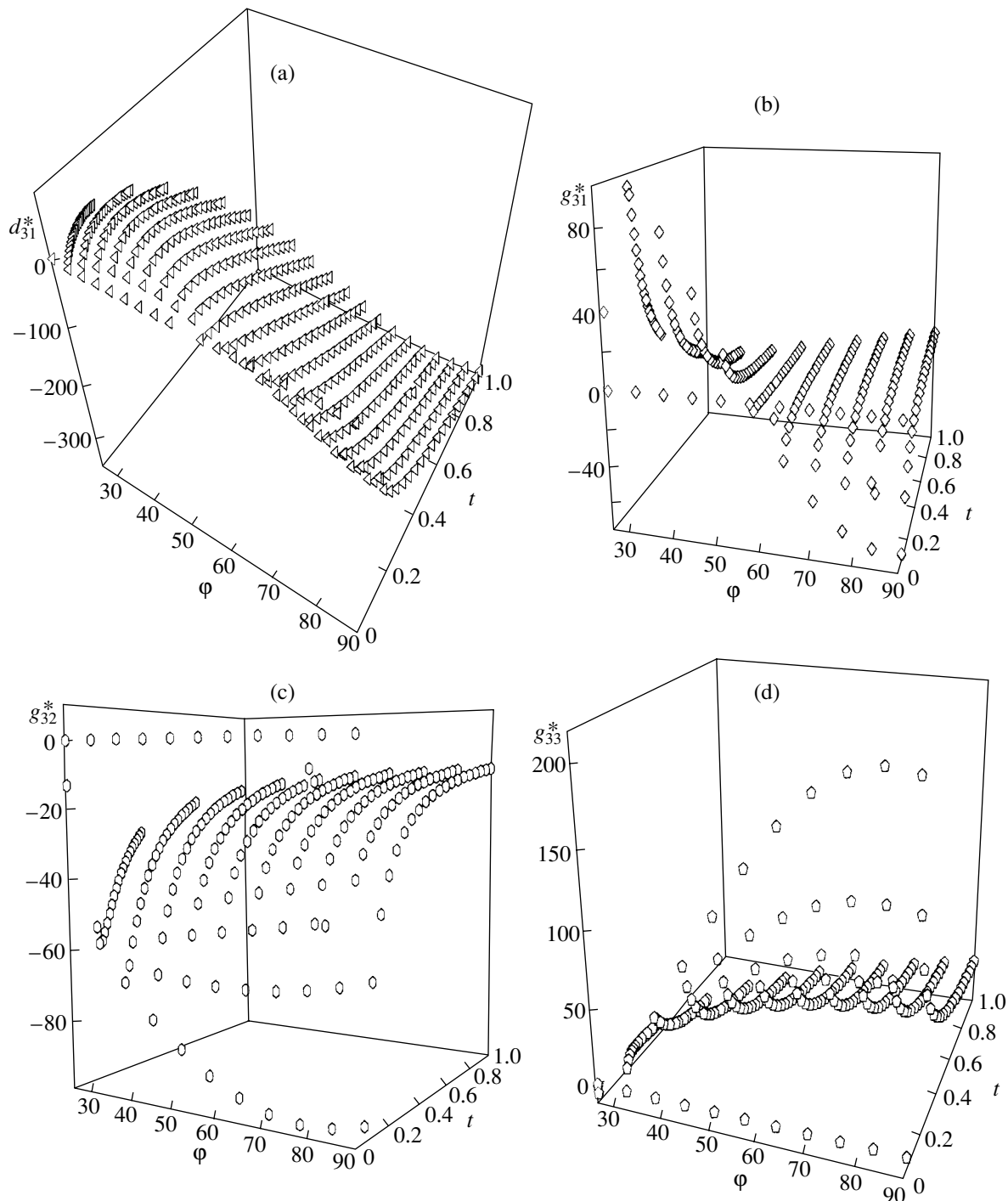
Fig. 2. Orientational and concentrational profiles of the piezoelectric coefficients calculated for a 1–2 composite of the FEPC–polymer (PKR-7M–araldite) type: (a) d_{31}^* (φ, t) [pC/N]; (b) g_{31}^* (φ, t); (c) g_{32}^* (φ, t); (d) g_{33}^* (φ, t) [mV m/N].

$-\mathrm{sgn}\, g_{32}^* = \mathrm{sgn}\, g_{33}^* > 0$ as in Figs. 2b–2d) previously observed neither in FEPC [1, 15] nor in the two-component piezoelectric composites [3, 4, 6–10]. The calculated values of $\max|g_{3j}^*(\varphi, t)|$ exceed by more than ten times the $|g_{3j}|$ values of PKR-7M, which is evidence of considerable advantages of the proposed 1–2 type

piezoelectric composite structure offering highly sensitive anisotropic material.

Thus, the results of our investigation of the piezoelectric response of 1–2 piezoelectric composites of the FEPC–polymer type show a nontrivial behavior of the effective piezoelectric coefficients $d_{3j}^*(\varphi, t)$ and $g_{3j}^*(\varphi, t)$

and their anisotropy in the permissible region of parameters (φ, t). The presence of zig-zag FEPC inclusions (accounting for the *mm*2 symmetry) is the main factor determining the piezoelectric properties and their anisotropy in the proposed 1–2 composites. An analysis of the system with 1–2 connectivity reveals new possibilities for the practical use of electromechanical properties of low-symmetry piezoelectric composites.

REFERENCES

1. K. Uchino, *Piezoelectric Actuators and Ultrasonic Motors* (Kluwer Acad. Publ., Boston, 1997).
2. A. Safari, Mater. Res. Innov. **2** (5), 263 (1999).
3. A. A. Grekov, S. O. Kramarov, and A. A. Kuprienko, Mech. Kompozit. Mater., No. 1, 62 (1989).
4. J. Bennett and G. Hayward, IEEE Trans. Ultrason. Ferroelectr. Freq. Contr. **43**, 98 (1996).
5. V. Yu. Topolov and A. V. Turik, Pis'ma Zh. Tekh. Fiz. **27** (2), 84 (2001) [Tech. Phys. Lett. **27**, 81 (2001)].
6. C.-W. Nan and G. J. Weng, J. Appl. Phys. **88**, 416 (2000).
7. C.-W. Nan, L. Liu, D. Guo, and L. Li, J. Phys. D: Appl. Phys. **33**, 2977 (2000).
8. A. A. Grekov, S. O. Kramarov, and A. A. Kuprienko, Ferroelectrics **76**, 43 (1987).
9. S. V. Glushanin and V. Yu. Topolov, Pis'ma Zh. Tekh. Fiz. **27** (15), 15 (2001) [Tech. Phys. Lett. **27**, 626 (2001)].
10. S. V. Glushanin and V. Yu. Topolov, J. Phys. D: Appl. Phys. **34**, 2518 (2001).
11. R. E. Newnham, D. P. Skinner, and L. E. Cross, Mater. Res. Bull. **13** (5), 525 (1978).
12. V. Yu. Topolov and S. V. Glushanin, J. Phys. D: Appl. Phys. **35**, 2008 (2002).
13. A. N. Alekseev, Izv. Ross. Akad. Nauk, Ser. Fiz. **57** (6), 92 (1993).
14. E. Akcakaya and G. W. Farnell, J. Appl. Phys. **64**, 4469 (1988).
15. V. Yu. Topolov and A. V. Turik, Zh. Tekh. Fiz. **71** (9), 26 (2001) [Tech. Phys. **46**, 1093 (2001)].

Translated by P. Pozdeev

Current Passage in a Vacuum Diode with Field- and Laser-Controlled Ferroelectric Cathode

Yu. V. Korobkin*, I. V. Romanov, A. A. Rupasov, and A. S. Shikanov

Lebedev Institute of Physics, Russian Academy of Sciences, Moscow, Russia
* e-mail: korobkin@sci.lebedev.ru
Received November 18, 2002

Abstract—We present the results of experimental investigation of a planar vacuum diode with field- and laser-controlled ferroelectric cathode based on prepolarized ceramics of the TsTS-23 (TsTS-19) grade. The diode current passes when the spontaneous polarization vector is oriented both toward the anode and in the opposite direction. It is established that an increase in the laser power density on the ceramic surface leads to a decrease in the diode current pulse duration. The maximum currents achieved in a field-controlled diode exceed the Langmuir current values by two to three orders of magnitude. The current pulse characteristics are determined by the mutual orientation of the polarization vector and the control electric field. © 2003 MAIK "Nauka/Interperiodica".

An important problem in particle acceleration and X-ray technology is related to the development of long-lived controlled emission cathodes capable of forming high-power electron beams with currents above 1 kA. One possible solution is offered by the laser plasma cathode [1], which is well known and widely used in X-ray sources. An advantage of this cathode over those of the explosive electron emission type is the ability to operate at any accelerating voltage, which is a critical condition for the obtaining of high-contrast characteristic X-ray lines. Unfortunately, the current of an electron beam ejected from a laser plasma expanding in the interelectrode gap is limited by the space charge and did not exceed 100 A [1]. One of the favorable methods of increasing the beam current is to increase the emission area, which is readily achieved by using ferroelectric cathodes. Physical models explaining the phenomenon of electron emission from ferroelectric (FE) materials are based on the notion of the change in spontaneous polarization under the action of either an electric field or laser radiation (for detailed description see, e.g., [2, 3]).

This study aimed at determining the optimum method for controlling the electron emission from FE cathodes, with a view to subsequent application in a pulsed characteristic X-ray line source. Here, we report on the results of two series of experiments. In the first series, we studied the current passage in a diode with a ferroelectric cathode controlled by applied high-voltage pulses; in the other series of experiments, the cathode was controlled by nanosecond pulses of the second-harmonic radiation of a neodymium laser.

The diode studied in our experiments had a cathode in the form of prepolarized FE disks made of TsTS-23 (TsTS-19) type ceramics with a thickness of 2 mm and a diameter of 40 mm. Both sides of the disk were coated

with perforated silver films (electrodes), to which the control high-voltage pulses were applied. The area of the metal-free FE cathode surface facing the anode was about 3 cm^2. The measurements were performed in a vacuum of 2×10^{-5} Torr. The cathode was controlled by rectangular negative voltage pulses with an amplitude of up to –10 kV and a duration of 25–125 ns, generated by a scheme developed for an arbitrary nonreflecting load [4]. The voltage was switched by a nitrogen-filled gap with laser-initiated discharge. The emitted electrons were collected with an anode having the form of a copper plate with an area of 3 cm^2, occurring at a positive voltage of 17 kV and grounded via a 5 nF capacitor. The diode current was measured in a low-inductance frequency-independent 1.7 Ω shunt in the collector circuit. The measurements were performed using a Lecroy Model 9350A oscillograph with a bandwidth of 500 MHz. In the first series of experiments, the collector–ceramic cathode distance was 2 cm.

In the course of our measurements, it was established that the diode current passes both when the pulsed electric field **E** is antiparallel with the spontaneous polarization vector **P** and when the two vectors are parallel. The ceramic disk was oriented with respect to the collector so that the polarization vector was either directed toward the collector (position 1) or pointed in the opposite direction (position 2). In the former case (FE ceramic cathode in position 1), the current pulse front virtually coincided with the high-voltage pulse front, and the current pulse amplitude for the external field opposite to the polarization vector was more than twice as large as the amplitude for the parallel field orientation (Figs. 1a and 1b). With the ceramic cathode in position 2, a delay between the applied voltage and diode current pulses reached ≈800 ns, while the current
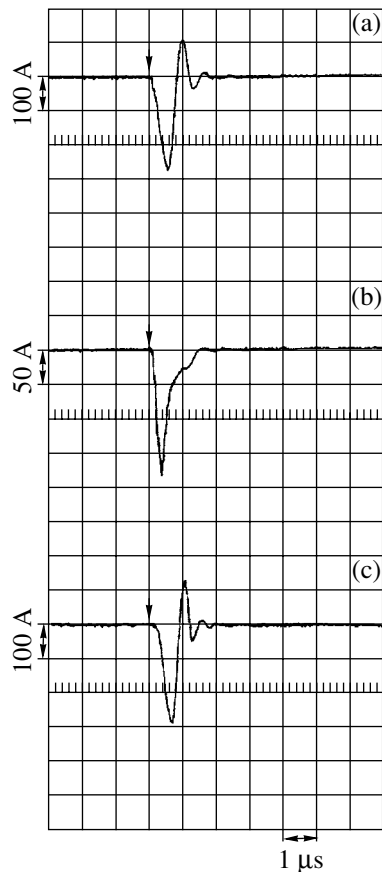
Fig. 1. Oscillograms of the diode current pulses observed for the FE ceramic cathode oriented with its spontaneous polarization vector **P** toward the collector: (a, b) diode current controlled by 25-ns voltage pulses with the external field antiparallel and parallel to **P**, respectively; (c) diode current controlled by laser pulses. Arrows indicate the moments of the pulse action upon the FE cathode.

Fig. 2. Oscillograms of the diode current pulses observed for the FE ceramic cathode oriented with its spontaneous polarization vector **P** outward the collector: (a, b) diode current controlled by 25-ns voltage pulses with the external field antiparallel and parallel to **P**, respectively; (c) diode current controlled by laser pulses. Arrows indicate the moments of the pulse action upon the FE cathode.

pulse amplitude was always greater than that observed in position 1 (Figs. 2a and 2b). The maximum diode current, obtained for the applied field parallel to the polarization vector (Fig. 2b), amounted to 2.4 kA.

Irrespective of the high-voltage control pulse duration (within the time interval indicated above), the diode current pulse width remained constant. It should be noted that, for all superpositions of the **P** and **E** vectors and the cathode orientation (positions 1 and 2), the current pulse duration was relatively large (≈350 ns). Evidently, the observed current amplitudes are two orders of magnitude greater than the values calculated by the nonmodified Langmuir 3/2 power law. This is indicative of the presence of additional acceleration mechanisms in the system. These may include (i) the normal electric field component enhancement (up to 10^9 V/cm) at the FE surface in the course of repolarization [5], (ii) plasma formation due to near-surface discharges [6] caused by the local repolarization accompanied by a significant field enhancement near the electrodes, and (iii) electric breakdowns at the triple
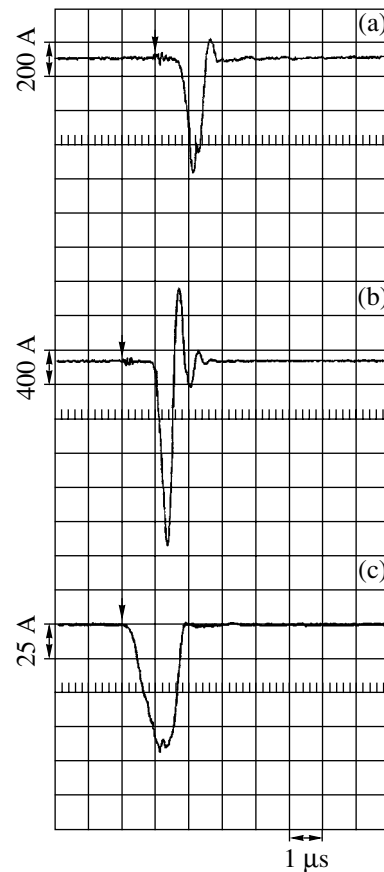
(metal–dielectric–vacuum) contact points according to the Bugaev–Mesyats model [7], caused by an increase in the tangential field component (up to 10^5 V/cm). When a high-voltage pulse was applied to the FE cathode, we observed a visible emission from the disk surface both in the presence and in the absence of external electric field. At a nonzero anode potential, emission was also observed from the anode surface and increased in intensity with the applied voltage. In our opinion, the emission from electrode surfaces is evidence of the plasma formation that predominantly accounts for the high diode currents observed.

We have also studied the dependence of the diode current on the geometry of control metal electrodes deposited onto the cathode surface. For this purpose, we have used the ceramic disks with electrodes representing either a lattice with 1×1 mm squares or a pattern of 2-mm-wide stripes spaced by 2 mm gaps (both patterns being closed with a band along the ceramic edge) (the values of current amplitude reported in this paper refer to the latter electrode configuration). In the

case of a cathode with the lattice electrodes, application of the control voltage was accompanied by the lattice–ceramic surface breakdowns at various sites. In the case of stripe electrodes, the whole cathode surface exhibited visible emission. In both cases, the aforementioned general trends in the diode current behavior were the same, except for the current amplitude values, which were one and a half times greater for the diode structure with stripe electrodes.

It is still incompletely clear what mechanism is responsible for the large time delay between the applied voltage and diode current pulses for the ceramic cathode in position 2. This effect is probably related to inertial FE repolarization and delayed plasma formation at the ceramic surface. The results of investigation of this delay effect by methods of plasma diagnostics with sufficient temporal resolution will be presented in a separate publication.

In the second series of experiments, the FE cathode operation was controlled by pulses of the second-harmonic radiation of a neodymium-doped phosphate glass laser operating at a wavelength of 0.527 μm, a pulse duration of 3 ns, and an energy of up to 1 J. In order to eliminate the laser-induced plasma formation, the second-harmonic radiation power density I at the ceramic surface was limited (not to exceed 2×10^7 W/cm^2). The angle of the laser beam incidence onto the sample surface was 45° and the cathode–collector distance was 4 cm. The diode current was measured for two orientations of the ceramic disk, with the spontaneous polarization vector directed either toward the cathode (opposite to the laser radiation propagation direction) or in the opposite direction (the electrode on the ceramic surface facing the collector was grounded). In both cases, no delay between the applied voltage and the diode current pulses was observed, but the current pulse in the former case had a greater amplitude (by a factor above three) and a shorter duration (by a factor of 2.5) as compared to the latter case (Figs. 1c, 2c). In this series of experiments, the maximum current amplitude was 300 A at a laser power density of 10^7 W/cm^2 on the ceramic surface.

The diode current pulse duration decreased with increasing laser radiation intensity. As the laser power density I increased from 3×10^6 to 10^7 W/cm^2, the current pulse width decreased from 700 to 400 ns in the former case and from 1.8 to 1.1 μs in the latter one. At the same time, the current amplitude remained virtually unchanged with increasing laser power. Such large values of the current pulse amplitude and duration indicate that photoemission does not produce a determining contribution to the current transfer in the diode studied. The dominating mechanisms are apparently the same as in the case of the field-controlled cathode (except for the dielectric state being changed due to the laser-induced pyroeffect). On the other hand, the assumption of plasma formation at the FE cathode surface under the

laser action should be verified by examination of the cathode surface under soft X-ray irradiation. Recently [8], we studied the electron emission from a monodomain crystal of lithium niobate (LiNbO$_3$) with Fe and Mg additives under analogous experimental conditions (about 40% of laser radiation was absorbed in the bulk of the sample). In that case, the current pulse amplitude and duration were 100 A and 400 ns, respectively, but no plasma formation was observed at the crystal surface.

Based on the experimental statistics, it should be noted that no visible decrease in the level of emission was observed in the course of sequential action of high-voltage pulses or laser radiation upon the FE ceramics. This is evidence that the system returns to the initial state.

Thus, the results of our investigation showed that maximum currents are obtained in the diode with a field-controlled ferroelectric cathode. The current transfer in such diodes is related to the electron emission from the plasma of discharges initiated at the surface of the FE cathode, the state of which changes under the action of control voltage pulses. The current pulse characteristics are determined by the method of cathode control, diode geometry, and control electrode configuration. It can be expected that, using FE plates of large areas as cathodes in the X-ray source, it is possible to obtain electron beams of subnanosecond duration with a current above 1 kA, with the corresponding increase in the X-ray intensity and dose.

REFERENCES

1. A. A. Erokhin, A. S. Kishinets, Yu. V. Korobkin, *et al.*, Zh. Éksp. Teor. Fiz. **119**, 1151 (2001) [JETP **92**, 998 (2001)].
2. H. Riege, I. Boscolo, J. Handerek, *et al.,* J. Appl. Phys. **84**, 1602 (1998).
3. G. Rosenman, D. Shur, and Ya. E. Krasik, J. Appl. Phys. **88**, 6109 (2000).
4. D. I. Proskurovskiĭ and E. B. Yankelevich, Prib. Tekh. Éksp. **16** (5), 108 (1973).
5. J. D. Ivers, L. Schachter, J. A. Nation, *et al.,* J. Appl. Phys. **73**, 2667 (1993).
6. A. Dunaevsky, Ya. E. Krasik, and J. Felsteiner, J. Appl. Phys. **85**, 8464 (1999).
7. S. P. Bugaev and G. A. Mesyats, Dokl. Akad. Nauk SSSR **196** (2), 324 (1971) [Sov. Phys. Dokl. **16**, 41 (1971)].
8. Yu. V. Korobkin, I. V. Romanov, A. A. Rupasov, *et al.*, Kratk. Soobshch. Fiz., No. 11, 13 (2001).

Translated by P. Pozdeev

A Method for Determining the Transient Process Duration in Dynamic Systems in the Regime of Chaotic Oscillations

A. A. Koronovskiĭ[a,*], A. V. Starodubov[a], and A. E. Khramov[b,**]

[a] *Saratov State University, Saratov, Russia*
* e-mail: alkor@cas.ssu.runnet.ru
[b] *State Scientific Center "College", Saratov, Russia*
** e-mail: aeh@cas.ssu.runnet.ru
Received November 12, 2002

Abstract—We describe a method for determining the transient process duration in a standard two-dimensional dynamic system with discrete time (Eno map), occurring in the regime of chaotic oscillations. © *2003 MAIK "Nauka/Interperiodica"*.

In most investigations devoted to nonlinear dynamic systems exhibiting complicated behavior, the attention of researchers is concentrated on the established regimes (which can be both periodic and chaotic). The initial (transient) stage of the process studied is frequently considered as insignificant and rejected, the analysis being mostly devoted to determining the characteristics (attractor dimensions, Lyapunov exponents, etc.) of established oscillation regimes, bifurcations arising upon variation of the control parameters, scenarios of the transitions to chaos, and so on. However, the transient processes also obey certain laws [1] and sometimes can provide important information about the whole system and its dynamics [2].

In studying a transient process, an important point is to determine (to within a preset accuracy ε) the moment when this process comes to an end and the system attains (with the same precision ε) an asymptotic state. In cases when the asymptotic state of a dynamic system of finite dimension is periodic (immobile stable point, periodic cycle), there is a quite simple and sufficiently effective algorithm of determining the time instant corresponding to the system reaching this state [1, 3]. The essence of this method can be formulated as follows: for a dynamic system with discrete time, (i) each element of a periodic attractor composed of a finite small number of points is surrounded by a circle of radius ε and (ii) the time when the imaging point falls within one of these ε neighborhoods is monitored. (Note that any dynamic flow system of finite dimension can be reduced to a map by using the Poincaré section procedure [4, 5].) However, the above approach is inapplicable to dynamic systems occurring in a chaotic state. The main difficulty is related to the fact that the number of points belonging to the chaotic attractor is infinite. This leads to difficulties in determining the necessary number of attractor points by which the transient process duration will be evaluated: this number proves to be

very large and strongly depends on the accuracy ε with which the process duration has to be determined [3]. Accordingly, the time required for trials involving the attractor elements substantially increases.

This study aimed at the creating an effective method for determining the transient process duration in a standard two-dimensional dynamic system with discrete time,

$$\mathbf{x}_{n+1} = \mathbf{F}(\mathbf{x}_n), \tag{1}$$

occurring in a chaotic regime. We have selected a standard two-dimensional dynamic system with a discrete map of the type known as the Eno map [6, 7],

$$x_{n+1} = \lambda x_n(1 - x_n) + b y_n, \quad y_{n+1} = x_n, \tag{2}$$

where λ and b are the control parameters determining the oscillation mode. Below, we will consider the case of $\lambda = 2.5453$ and $b = 0.5188$, which corresponds to a chaotic oscillation regime in system (2).

By the transient process duration in a system with discrete time is implied an interval of K discrete time units, after the elapse of which the imaging point in the phase space attains an attractor to within a preset accuracy ε. In other words, for all $n > K$

$$\left\| \mathbf{x}_n - \mathbf{x}_j^0 \right\| < \varepsilon, \tag{3}$$

where $\mathbf{x}_n$ are the points of time series of the given dynamic system, $\mathbf{x}_j^0$ ($j = \overline{1, \ldots, M}$) are the elements of a chaotic attractor, and ε is the preset accuracy with which the transient process duration has to be determined. Formally speaking, a transient process is infinitely long: the imaging point asymptotically approaches the attractor as $t \longrightarrow \infty$, never reaching it for a finite time. On the other hand, regions corresponding to an established regime and the transient process can usually be separated in the time series obtained by the experiments under natural conditions and by
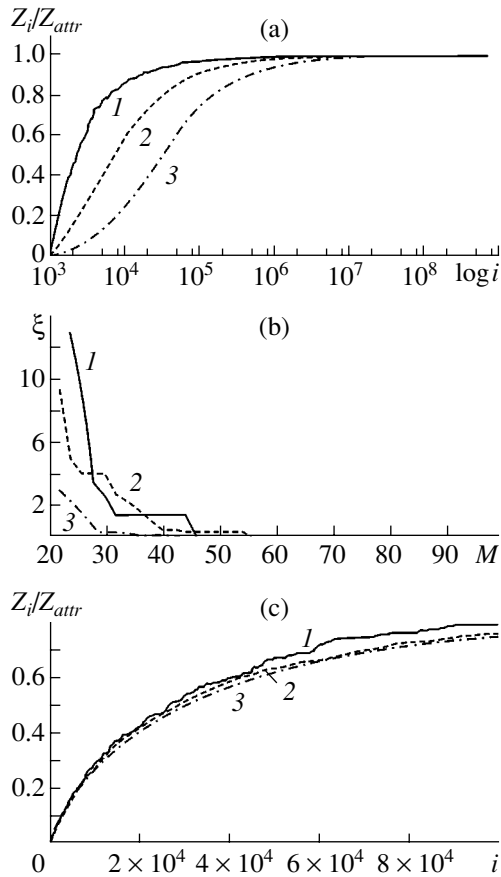
Fig. 1. Plots of (a) the number of attractor cells Z_i (normalized to the total number of cells Z_{attr} found for a preset accuracy ε) versus the number of iterations i, (b) percentage of errors ξ in determining the transient process duration versus the percentage M of attractor cells used for this determination, and (c) the normalized number of attractor cells Z_i versus the number of iterations (normalized to μ) for various values of the accuracy: $ε = 10^{-2}$ (*1*), $10^{-5/2}$ (*2*), and 10^{-3} (*3*). Control parameters: $λ = 2.5453$ and $b = 0.5188$. Initial conditions: $x_0 = 0.1$ and $y_0 = 0.1$.

numerical modeling of the behavior of various systems [8, 9]. The transient process duration depends on the control parameters, initial conditions, and the preset uncertainty ε within which the imaging point reaches the attractor.

The proposed method is essentially as follows: the region of initial conditions containing the attractor is covered with a lattice of period (step) ε. Then an initial condition $\mathbf{x}_0$ (i.e., an initial point in the attraction basin) is selected and the system (1) is iterated a sufficiently large number of times N (definitely greater than the maximum transient time duration $T_{\max}$). In the course of this iteration process, the imaging point travels over the lattice following the attractor and passing through various lattice cells. Beginning with the discrete time $i = T_{\max} + 1$, we count the number of cells visited by the imaging point during the iterative procedure. These

cells covering the attractor points $\mathbf{x}_j^0$ will be referred to as the attractor cells. After termination of the iterative procedure, we obtain a basis array of such attractor cells. Once the cells belonging to the attractor are known, the transient process duration can be determined as follows: if the initial point $\mathbf{x}_0$ falls within an attractor cell upon iteration for K discrete time units, the transient process duration determined for the given initial condition to within a preset accuracy ε is K. Obviously, correct determination of the transient process duration requires finding possibly large number of the attractor cells.

Since it is considered that, past the transient process of K discrete time units, the imaging point reaches a chaotic attractor, the condition (3) must be satisfied for all $i > K$. Theoretically, a situation is possible whereby the imaging point $\mathbf{x}_i$, approaching one of the chaotic attractor points $\mathbf{x}_j^0$ to a distance below ε upon the ith iteration, does not in fact reach the attractor: condition (3) fails to be valid upon the $(i + 1)$th iteration and no one point of the chaotic attractor falls within the ε neighborhood of point $\mathbf{x}_{i + 1}$. In this case, completion of the transient process is verified by checking the condition (3) for m sequential control points $\mathbf{x}_{i + 1}, \ldots, \mathbf{x}_{i + m}$. However, this verification procedure was shown [3] to be unnecessary, only significantly increasing the time required for correctly determining the transient process duration by trying a large number of points of the chaotic attractor.

In our study, the iterative procedure included $N = 5 \times 10^8$ steps and the maximum iterative process duration was $T_{\max} = 10^3$. Such a large number of iterations was necessary to provide for a more complete basis array, offering a good approximation to a true chaotic attractor and possessing all its essential properties. A numerical experiment showed that, for $ε = 10^{-2}$ and the corresponding number of iterations, the number of attractor cells is $Z_{attr} = 1228$; for $ε = 10^{-5/2}$, $Z_{attr} = 5622$; and for $ε = 10^{-3}$, $Z_{attr} = 25199$.

Now let us consider the dependence of the number of attractor cells Z_i on the number of accomplished iteration steps i for which the attractor cells were found at a given ε (Fig. 1a). As can be seen from the character of these curves, the rate of increase in the number of attractor cells is sufficiently large in the initial stage of the time series. As the number of iterations increases, this rate drops and eventually the curves exhibit saturation. This behavior indicates that further iteration process is inexpedient: new cells are very rarely (or not at all) added to the attractor. Obviously, the higher the accuracy (the lower the error) of determination of the transient process duration, the greater number of iterations i has to be performed in order to provide that the Z_i curve reaches the level of saturation for Z_{attr}.

Once it is known which cells on the (x, y) plane belong to the chaotic attractor, we can study the dependence of the transient process duration for the Eno map
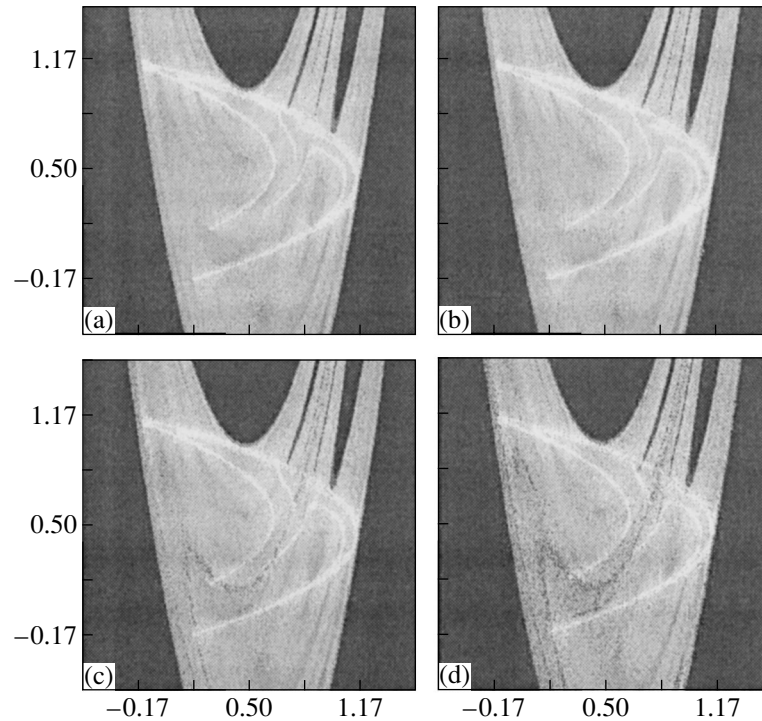
Fig. 2. Gray gradation maps showing the transient process duration as a function of the initial conditions for the Eno map (2), calculated using various numbers of the attractor cells $M = 100\%$ (a), 90% (b), 80% (c), and 60% (d) for the control parameters: $\lambda = 2.5453$ and $b = 0.5188$ and the accuracy $\varepsilon = 10^{-3}$. The maximum transient process duration is $T = 20$. Black areas correspond to the initial conditions from which the imaging point goes to infinity.

with various initial conditions (x_0, y_0) on the number of attractor cells Z_{attr} found. Figure 1b shows the plots of the percentage of errors in determining the transient process duration versus percentage M of the basis array cells used for this determination. Here, by errors are implied the situations when the transient process duration determined for the initial condition (x_0, y_0) using 100% of the basis array cells differs from that determined using only M [%] of such cells. The initial conditions were represented by an array of 10^3 random points (x, y). Obviously, the smaller the number of the attractor cells used for determining the transient process duration, the greater the percentage of errors. As can be seen from Fig. 1b, there is a certain value of $M < 100\%$, above which the number of errors in determining the transient process duration is minimal for all values of ε.

Figure 2 presents the maps of the transient process duration as a function of the initial conditions (x_0, y_0) plotted using the proposed method for various numbers of attractor cells. These maps were constructed as follows: each point of the (x, y) plane was considered as an initial condition, the system with this initial condition was characterized by the transient process duration, and the given point was painted with the corresponding color gradation. The greater the transient process duration, the darker the gray color gradation for this point. In this way, the chaotic attractor was painted white. As

can be seen from Fig. 2, a decrease in the number of basis array cells used for determining the transient process duration leads to the appearance of darker (or even black) points. This is explained by the fact that the transient process duration is incorrectly calculated for some initial conditions.

Thus, the above data indicate that the transient process duration can be determined using a fraction of the basis array cells, rather than the whole array. With this fraction, a relatively small number of iterations i can be accomplished. This number depends on the accuracy ε with which the transient process duration has to be determined. In connection with this, it is of interest to study the relation between the capacitive dimension D_0 of a chaotic attractor [10] and the number of iterations i of map (2) necessary for correctly determining the transient process duration to within a preset accuracy ε. In other words, the question is whether we can find, proceeding from the known attractor dimension D_0, a scaling factor that allows us to determine the number of iterations necessary for correctly calculating the transient process duration with a higher accuracy (or lower ε).

In order to elucidate the above question, we have calculated the attractor dimension and obtained $D_0 = 1.31$. For two values of the accuracy, ε_1 and ε_2 such that $\varepsilon_2 = \varepsilon_1/a$, the numbers of the attractor cells are $N_1(\varepsilon) \sim$

$\varepsilon_1^{-D_0}$ and $N_2(\varepsilon) \sim \varepsilon_2^{-D_0}$. Thus, the scaling factor is determined as $\mu = N_2/N_1 = (\varepsilon_2/\varepsilon_1)^{-D_0} = a^{D_0}$. For $a = \sqrt{10}$, we obtain $\mu = 10^{D_0/2} \approx 4.54$. Figure 1c shows the plots of Z_i/Z_{attr} for various values of ε, with the number of iterations normalized to the above scaling factor μ. As can be seen from Fig. 1c, the curves coincide with each other to within a rather high precision. Therefore, once the necessary number of iterations N_1 for correctly determining the transient process duration with a preset accuracy ε_1 is known, it is possible to calculate the value of necessary iterations N_2 for any other ε_2.

Thus, we have proposed an effective and rapid method for determining the transient process duration in a two-dimensional dynamic system with discrete time, occurring in the regime of chaotic oscillations. This approach is also applicable to systems with continuous time, which can be reduced to maps via the Poincaré section method.

REFERENCES

1. A. A. Koronovskiĭ, D. I. Trubetskov, A. E. Khramov, and A. E. Khramova, Dokl. Ross. Akad. Nauk **383** (3), 322 (2002) [Dokl. Phys. **47** (3), 181 (2002)].

2. B. P. Bezruchko, T. V. Dikanev, and D. A. Smirnov, Phys. Rev. E **64**, 036210 (2001).

3. A. A. Koronovskiĭ, A. V. Starodubov, and A. E. Khramov, Izv. Vyssh. Uchebn. Zaved., Prikl. Nelin. Dinam. **10** (4) (2002).

4. M. Henon, Physica D **5**, 412 (1982).

5. Z. Kaufmann and H. Lustfeld, Phys. Rev. E **64**, 055206(R) (2001).

6. M. Henon, Commun. Math. Phys. **50**, 69 (1976).

7. *Strange Attractors (A Collection of Papers)*, Ed. by Ya. G. Sinaĭ and L. P. Shil'nikov (Mir, Moscow, 1981).

8. I. M. Janosi and T. Tel, Phys. Rev. E **49**, 2756 (1994).

9. A. A. Koronovskiĭ, I. S. Rempen, D. I. Trubetskov, and A. E. Khramov, Izv. Ross. Akad. Nauk, Ser. Fiz. **66**, 1754 (2002).

10. S. P. Kuznetsov, *Dynamic Chaos* (Fizmatlit, Moscow, 2001).

Translated by P. Pozdeev

Absorption and Luminescence of Vanadium(IV) in a K_2O–Al_2O_3–P_2O_5 Glass System

I. M. Batyaev, S. V. Linnikov, and A. L. Lipatova

Herzen Pedagogical Institute, St. Petersburg, Russia
Revised manuscript received November 22, 2002

Abstract—Potassium aluminosilicate phosphate glass with the composition 30% K_2O–20% Al_2O_3–50% P_2O_5 (wt %) activated by tetravalent vanadium ions was synthesized and characterized with respect to physicochemical properties, including room temperature luminescence and absorption spectra. Based on the electronic absorption spectra, it is concluded that the glass contains oxovanadium ions. © *2003 MAIK "Nauka/Interperiodica".*

This study is a continuation of our investigation into the spectral and kinetic characteristics of luminescence of $3d$ group impurities in aluminum phosphate glasses, aluminosilicate phosphate glasses, and some other inorganic materials [1–9]. This interest is related to the use of glassy compositions doped with d and f elements in quantum electronics, optoelectronics, and fiber optics [10–11].

In recent years, extensive research was devoted to the properties of titanium(III) ion as a promising activator for new laser systems [1–9]. The purpose of our work was to study the properties of vanadium(IV) ions possessing an electron structure analogous to that of Ti^{3+}. Indeed, the electron structure of V^{4+} is isoelectron to that of Ti^{3+}. However, formal assignment of the absorption bands of V^{4+} to the transitions between levels of the $3d'$ configuration seems to be incorrect for the following reasons. All oxygen-containing complexes of V^{4+} contain, irrespective of the coordination number (6 or 5), VO groups with predominating V=O double bond (in all such complexes, one V–O bond is much shorter than the other) [11]. The most symmetric complex of vanadium (VOL_5) possesses a C_{4V} symmetry.

The glass was synthesized (at 1200°C in an inert atmosphere) from a preliminarily cooked charge with the composition 30% K_2O–20% Al_2O_3–50% P_2O_5 (wt %), to which vanadium(IV) oxide (VO_2) was added in an amount of 0.25 wt %. The charge was prepared from a mixture of potassium metaphosphate and aluminum phosphate, which was triturated and kept in a crucible at 1200–1250°C. The as-cooked glass was crushed, mixed with VO_2, and cooked again in an inert atmosphere in order to prevent the oxidation of vanadium(IV) into vanadium(V). The melt was poured into a steel mold (heated to ~300°C) and annealed at this temperature for several hours. This process yielded a potassium aluminum phosphate glass with the composition 23.7% K_2O–17.1% Al_2O_3–59.2% P_2O_5 (mol %)

containing 0.26 wt % VO_2. This glass possesses a green color, which is characteristic of vanadium(IV) compounds. The spectral measurements were performed on 10×20 mm plates with a thickness of 4–5 mm.

The electronic absorption spectra of glass samples were recorded on an SF-20 spectrophotometer. The luminescence spectra were measured using an SDL-1 spectrophotometer using a He–Ne laser (LGN-222, $\lambda_b = 630$ nm, $P = 55$ mV) as the excitation source. The luminescence decay kinetics in the samples excited with a pulsed nitrogen laser (LGI, $\lambda = 337$ nm, $\tau_{pulse} = 10$ ns) was measured using an oscillographic technique.

A comparative analysis of the electronic absorption spectra of our glass samples to the analogous published data allowed us to conclude that the system studied contains complex vanadium ions VO^{2+}. Thus, our spectral data are interpreted below based on the notion of oxovanadium ions present in potassium aluminum phosphate glasses [12–15].

The absorption spectrum of the glass composition studied (Fig. 1) contains a broad band with a maximum at 890 nm and a characteristic shoulder at 690 nm [15]. With allowance for the above assumption, the bands at 14490 and 11240 cm^{-1} are assigned to the electron transitions $e \longrightarrow b_1$ and $e \longrightarrow a_1$, respectively. We did not observe a band due to the third (expected) transition, probably because of its low intensity and overlap with the fundamental absorption band of the glass matrix. Apparently, this transition can be detected upon changing the matrix composition.

The glass samples studied exhibited intense luminescence in the region of 800–1000 nm (Fig. 2), which is related to the electron-vibrational transition $b_2 \longrightarrow e$. In samples with a vanadium(IV) oxide content of 0.25 wt %, the average emission duration was 12 ± 1 μs. The accuracy of these measurements (determined as the rms deviation for several measurements) did not exceed 10%.
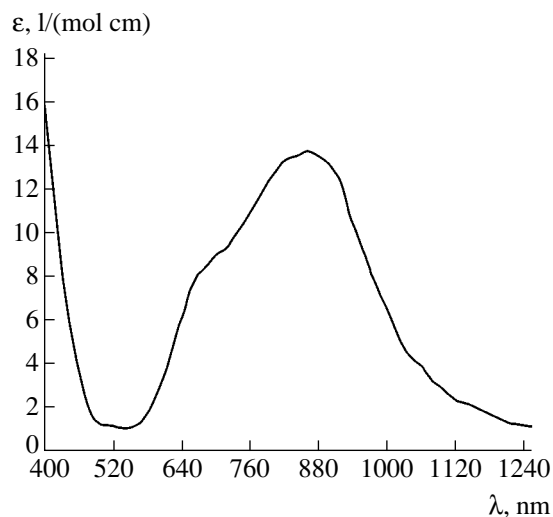
ε, l/(mol cm)

Fig. 1. A typical electronic absorption spectrum of the glass composition studied.
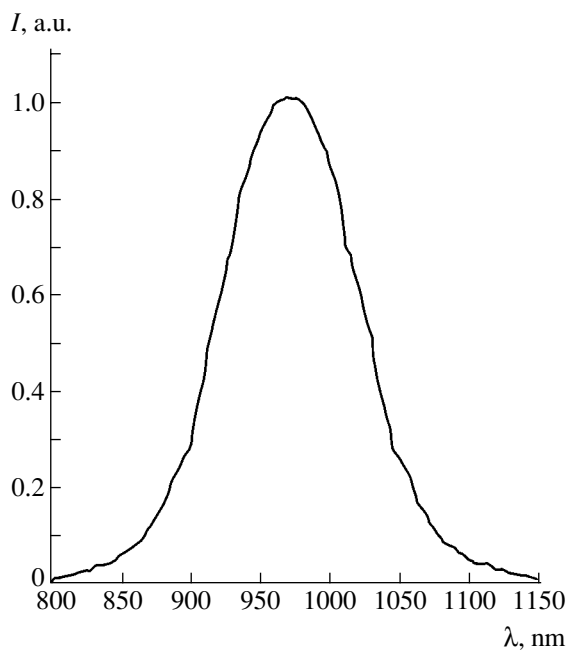
I, a.u.

Fig. 2. A typical laser-excited luminescence spectrum of the glass composition studied.

Thus, we have synthesized a potassium aluminum phosphate glass activated by tetravalent complex vanadium ions, studied the spectral and luminescent properties of this glass, and estimated the lifetime of the excited state. Our experiments show good prospects for using vanadium(IV) compounds as activators in tunable solid state lasers.

REFERENCES

1. I. M. Batyaev and S. B. Sukhanov, Opt. Spektrosk. **72** (6), 1367 (1992) [Opt. Spectrosc. **72**, 765 (1992)].
2. I. M. Batyaev and S. B. Sukhanov, Pis'ma Zh. Tekh. Fiz. **20** (10), 38 (1994) [Tech. Phys. Lett. **20**, 403 (1994)].
3. I. M. Batyaev and I. V. Golodova, Opt. Spektrosk. **77** (1), 81 (1994) [Opt. Spectrosc. **77**, 45 (1994)].
4. I. M. Batyaev and Yu. G. Kobezhikov, Pis'ma Zh. Tekh. Fiz. **22** (11), 81 (1996) [Tech. Phys. Lett. **22**, 472 (1996)].
5. I. M. Batyaev and E. B. Kleshchinov, Opt. Spektrosk. **81** (5), 823 (1996) [Opt. Spectrosc. **81**, 753 (1996)].
6. I. M. Batyaev and E. B. Kleshchinov, Pis'ma Zh. Tekh. Fiz. **22** (12), 34 (1996) [Tech. Phys. Lett. **22**, 494 (1996)].
7. I. M. Batyaev and E. B. Kleshchinov, Pis'ma Zh. Tekh. Fiz. **23** (21), 7 (1997) [Tech. Phys. Lett. **23**, 820 (1997)].
8. I. M. Batyaev and Yu. G. Kobezhikov, Opt. Spektrosk. **85** (1), 68 (1998) [Opt. Spectrosc. **85**, 60 (1998)].
9. I. M. Batyaev, A. M. Tinus, and E. B. Kleshchinov, Pis'ma Zh. Tekh. Fiz. **24** (3), 38 (1998) [Tech. Phys. Lett. **24**, 97 (1998)].
10. *Laser Handbook*, Ed. by A. M. Prokhorov (Sov. Radio, Moscow, 1978).
11. *The Physics and Spectroscopy of Laser Crystals,* Ed. by A. A. Kaminskii (Nauka, Moscow, 1986).
12. A. A. Platonov, *Mineral Coloration Nature* (Naukova Dumka, Kiev, 1976).
13. A. Lever, *Inorganic Electronic Spectroscopy* (Elsevier, Amsterdam, 1974; Mir, Moscow, 1987).
14. C. J. Balhausen and H. B. Gray, Inorg. Chem. **1**, 111 (1962).
15. I. M. Batyaev and S. V. Linnikov, Zh. Obsch. Khim. **68**, 1211 (1998).

Translated by P. Pozdeev

Use of a Pulsed Electron Beam for Air Cleaning from Methyl Methacrylate Vapor

A. N. Drachev, Yu. N. Novoselov*, and I. E. Filatov

Institute of Electrophysics, Ural Division, Russian Academy of Sciences, Yekaterinburg, Russia
* e-mail: nov@iep.uran.ru
Received November 25, 2002

Abstract—The results of experiments on methyl methacrylate (MMA) vapor decomposition in nitrogen–oxygen mixtures under the action of a pulsed electron beam are reported. It is established that there are two competitive mechanisms of MMA removal, with and without participation of active oxygen species. © *2003 MAIK "Nauka/Interperiodica".*

As is known, the production and processing of plastics are accompanied by considerable release of toxic organic compounds in amounts significantly above the corresponding minimum permissible concentration (MPC) levels. Monomers employed in the synthesis of plastics or formed upon their thermal degradation contain multiple bonds (i.e., belong to unsaturated compounds) and functional groups. Such compounds are extremely toxic on the one hand and highly reactive on the other. The latter circumstance allows us to use plasmachemical methods as a means of eliminating these products from waste gases of various technologies. For example, acrolein [1], styrene [2, 3], ethylene halogen derivatives [4], and some other compounds can be effectively, with relatively low energy consumption, removed under the action of electron beams.

One of the monomers dangerously contaminating industrial waste gases is methacrylic acid methyl ether (methyl methacrylate, MMA). This compound is involved in large-scale commercial production of organic glasses and is intensively evolved during the synthesis of related compositions. Considerable air contamination with MMA vapor takes place in the course of mechanical processing of MMA-based organic glasses, whereby the MMA concentration in air may significantly exceed the MPC level. Here, we report the results of experiments on MMA vapor removal from model gas mixtures under the action of a pulsed electron beam.

The experiments were performed on a setup analogous to that described previously [1]. The source of high-energy electrons was based on a nanosecond-pulsed electron accelerator of the RADAN type. The accelerator produced a beam of electrons with the following parameters: energy, 180 keV; current density, ~800 A/cm²; pulse duration (FWHM), 3 ns; output beam cross section, 1 cm²; pulse repetition rate, up to 10 s^{-1}. The reaction chamber, with a volume of 3000 cm^3, was filled with a model gas mixture to a pres-

sure of 1 atm. The electron pathlength was equal to the distance from the accelerator output window to the target (1 cm). Depending on the gas phase composition, the energy deposited by the electron beam was varied from 0.6 to 4.2 mJ per pulse, as determined by a standard dose meter.

The reaction chamber was equipped with a ventilator producing effective stirring of the gas mixture. The MMA content in the gas phase was monitored by a gas chromatograph (Tsvet-500) equipped with a plasma-ionization detector, ensuring a detection limit of 0.1 ppm. The error of the MMA concentration determination did not exceed 10 and 5% at a MMA concentration level of 10 and 1000 ppm, respectively. The samples for analysis were taken with a miniature pump driving the gas mixture via a contour including the reaction chamber and the chromatograph dose loop.

We have studied the dependence of the MMA content in a gas mixture inside the reaction chamber versus the number of radiation pulses (i.e., of the specific energy W deposited in the gas phase). Figure 1 shows the typical plots of $\ln(C_0/C)$ versus W (where C_0 and C are initial and current MMA concentrations) for various gases and gas mixtures. As can be seen, the experimental plots obtained for the initial MMA contents below 200 ppm (Fig. 1, curves *1–3*) can be approximated by straight lines, which corresponds to an exponential character of variation of the impurity concentration with the radiation energy W [J/l] deposited in the gas. Therefore, following [3], we can use the concept of the characteristic energy β according to the relation

$$\ln(C_0/C) = W/\beta. \qquad (1)$$

The physical meaning of coefficients β, given by the slope of curves *1–3*, is the amount of energy that has to be deposited in the gas in order to reduce the impurity concentration by a factor of e ($e = 2.718…$).
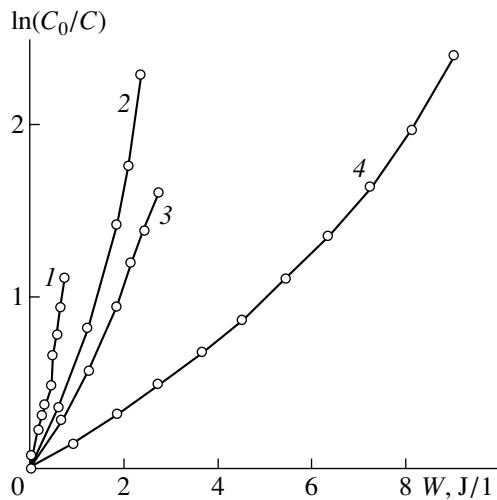
Fig. 1. The plots of $\ln(C_0/C)$ versus specific energy W deposited in the gas for different initial MMA impurity concentrations $C_0 = 200$ (*1–3*) and 900 ppm (*4*) in various gases: (*1*) helium; (*2*) 80% N_2–20% O_2; (*3*) nitrogen; (*4*) 80% N_2–20% O_2.
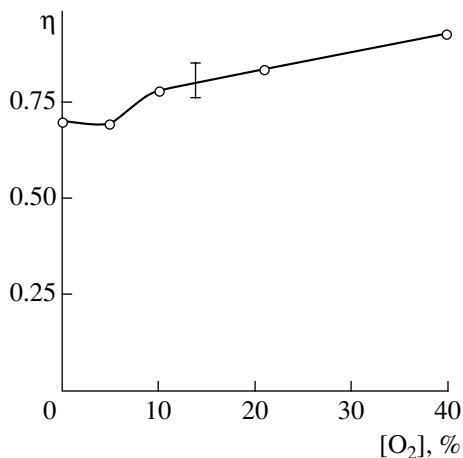

Fig. 2. The plots of MMA conversion η versus oxygen concentration $[O_2]$ in an N_2–O_2 mixture ($C_0 = 200$ ppm; $W = 2$ J/l).

We can also employ a formal approach that was developed previously for description of the conversion of styrene admixture in ionized air [3]. According to this, the *i*th process generated by a pulsed electron beam injected into a gas mixture produces a certain amount of the corresponding reagent R_i ($i = 1, 2, …, N$). In the general case, the equation describing variation of the concentration of various components (e.g., MMA) in the ionized gas mixture can be written as

$$\frac{dC}{dW} = -\sum_{i=1}^{N} k_i [R_i]^a C^b. \qquad (2)$$

Here, k_i is the coefficient characterizing the energy deposited in the *i*th process and a and b are the corre-

sponding reaction orders with respect to reagent R_i and MMA, respectively. When $C \ll [R_i]$, the parameter b tends to unity, and the product $k_i[R_i]$, to a constant (in this case, to $1/\beta$). For $b \approx 1$, we observe the first-order process of MMA elimination, which implies that the concentration of MMA molecules removed is proportional to the concentration of reagent R_i.

Increasing the initial MMA content to 900 ppm leads to nonlinearity of the $\ln(C_0/C)$ versus W plots (Fig. 1, curve *4*). In this case, the concentration of reagent R_i may also depend on C, whereby a considerable part of R_i is involved in the process of MMA binding. For a correct description, it is necessary to solve system of equations (2) taking into account the presence of various active reagents ($i > 1$) and the influence of MMA conversion products upon the process. The overall MMA binding reaction is dominated by processes of the (formally) second order, bi- and trimolecular reactions (i.e., $b \geq 2$), which modify the character of the $\ln(C_0/C)$ versus W plots.

Figure 2 shows a plot of the degree of MMA conversion $\eta = (C_0 - C)/C_0$ versus the oxygen concentration $[O_2]$. As can be seen, there are two characteristic regions on this curve. At small $[O_2]$ values, η does not exceed 70–75%; as the oxygen concentration increases above 5%, the efficiency of MMA removal grows to indicate that oxygen begins to determine the process of MMA elimination from the gas phase. The reason for this alteration in the behavior of the η versus $[O_2]$ plot is probably related to a change in the mechanism of MMA conversion. In the oxygen-free MMA mixtures with helium and nitrogen (Fig. 1, curves *1* and *2*), the impurity can be removed either under a direct action of the electron beam or due to reactions with active helium or nitrogen species R_i, the concentration of which is proportional to the energy deposited in the gas. In a nitrogen–oxygen mixture, the main reagents R_i are probably the active species formed from oxygen molecules under the beam action. This assumption is confirmed by the growth of η with the concentration of oxygen (Fig. 2).

The energy spent for removal of the impurity molecules can be estimated from the following relationship: $\varepsilon = W/q(C_0 - C)$ [eV per MMA molecule], where $q = 1.6 \times 10^{19}$ C is the electron charge. For the same specific energy W supplied to the gas, e.g., $W = 2$ J/l, this specific energy amounts to about 1.8 eV in the region of high initial MMA concentrations ($C_0 = 900$ ppm) and increases to $\varepsilon \sim 5$ eV when the initial MMA content is small ($C_0 = 200$ ppm). The growth in ε with decreasing concentration of removed impurity follows from the law of mass action (2). However, curve *2* in Fig. 1 (obtained at $C_0 = 200$ ppm and $W = 2$ J/l) corresponds to $\varepsilon \sim 3$ eV. Therefore, the energy efficiency of MMA removal from the gas phase depends on the system prehistory, which can be explained by inactivation of the reagent R_i species by MMA degradation products.

Thus, the above data are indicative of a relatively high efficiency of MMA impurity removal from contaminated air under the action of a pulsed electron beam. Elucidation of the particular mechanisms involved in the conversion of organic impurities in nonequilibrium plasmas is the subject for further investigation.

REFERENCES

1. Yu. N. Novoselov and I. E. Filatov, Pis'ma Zh. Tekh. Fiz. **24** (16), 35 (1998) [Tech. Phys. Lett. **24**, 638 (1998)].
2. G. A. Mesyats, Yu. N. Novoselov, and I. E. Filatov, Pis'ma Zh. Tekh. Fiz. **27** (19), 25 (2001) [Tech. Phys. Lett. **27**, 813 (2001)].
3. Yu. N. Novoselov and I. E. Filatov, Dokl. Ross. Akad. Nauk **382** (4), 1 (2002).
4. Y. H. Won, D. H. Han, T. Stuchinskaya, *et al.*, Radiat. Phys. Chem. **63**, 165 (2002).

Translated by P. Pozdeev

Forced Synchronization in a System with Unstable Cycle

A. P. Kuznetsov* and L. V. Tyuryukina

Saratov Branch, Institute of Radio Engineering and Electronics, Russian Academy of Sciences, Saratov, Russia
* e-mail: alkuz@sgu.ru
Received November 10, 2002

Abstract—The dynamics of a system with unstable limiting cycle under the action of a periodic sequence of delta pulses is considered. It is shown that stable quasiperiodic regimes and phase lock regimes (synchronization) can be observed within a narrow range of parameters of the external signal. © 2003 MAIK "Nauka/Interperiodica".

The phenomenon of synchronization, albeit known for a long time, still draws the attention of researchers. The classical case of synchronization consists in an external periodic (usually harmonic) signal acting upon an autooscillating system with a stable limiting cycle [1, 2]. In this case, frequency locking and quasiperiodic regimes are possible inside and outside the Arnold language, respectively, on the external signal frequency–amplitude plane. In phase space, these regimes are represented either by a stable torus (corresponding to a closed curve in the Poincaré cross section) or by the stable and saddle limiting cycles appearing on this torus upon crossing the language boundary.

Let us consider an alternative variant, whereby an unstable limiting cycle is realized in an autonomous system. At first glance, either unstable torus or unstable cycles can be expected in the phase space of this system in the presence of an external action. However, the nonlinear dynamics give many examples of phenomena related to the so-called problem of controlled chaos [3]. Within the framework of these notions, it is possible to study situations in which external actions can stabilize the initially unstable system. For example, an external signal acting upon a discrete system possessing an unstable cycle can lead to stabilization of this cycle, provided that the external signal is determined by elements of the unstable cycle. In this context, an interesting question is whether a pulsed action can lead to stabilization in a system with unstable limiting cycle and initiate stable synchronous and quasiperiodic regimes. We have established that such control is possible.

In order to demonstrate the possibility of induced synchronization, let us consider a system possessing an unstable limiting cycle, described by an equation of the Van der Pol–Duffing type and excited by a periodic sequence of δ-shaped pulses:

$$\ddot{x} + (\lambda - x^2)\dot{x} + x + \beta x^3 = B\sum \delta(t - nT). \quad (1)$$

Here, x is a dynamic variable, λ is a control parameter (at $\lambda = 0$, the system features a reverse Andronov–Hopf

bifurcation whereby an unstable focus at the origin becomes stable with separation of an unstable limiting cycle), T is the pulse repetition period, and B is the pulse amplitude.

In the autonomous case with positive λ, a system described by Eq. (1) possesses a stable immobile point and an unstable limiting cycle. The corresponding phase portrait is depicted in Fig. 1. Now let us switch on the external signal according to Eq. (1). Figure 2 shows a map of dynamic regimes on the $T–B$ plane of parameters for this differential equation with the control parameter $\lambda = 1.2$ and the phase nonlinearity (nonisochronicity) parameter $\beta = 1$. In the map of Fig. 2, white color corresponds to the regime of period 1; light gray, to the regime of period 2, and so on; and black color indicates quasiperiodic regimes and chaos (the runaway of trajectories is also indicated by gray tint). The cycle period is determined in the Poincaré cross sections separated by time intervals equal to the period T of the external action.
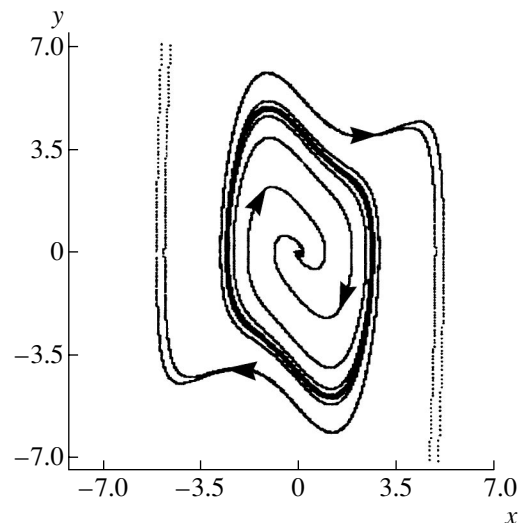

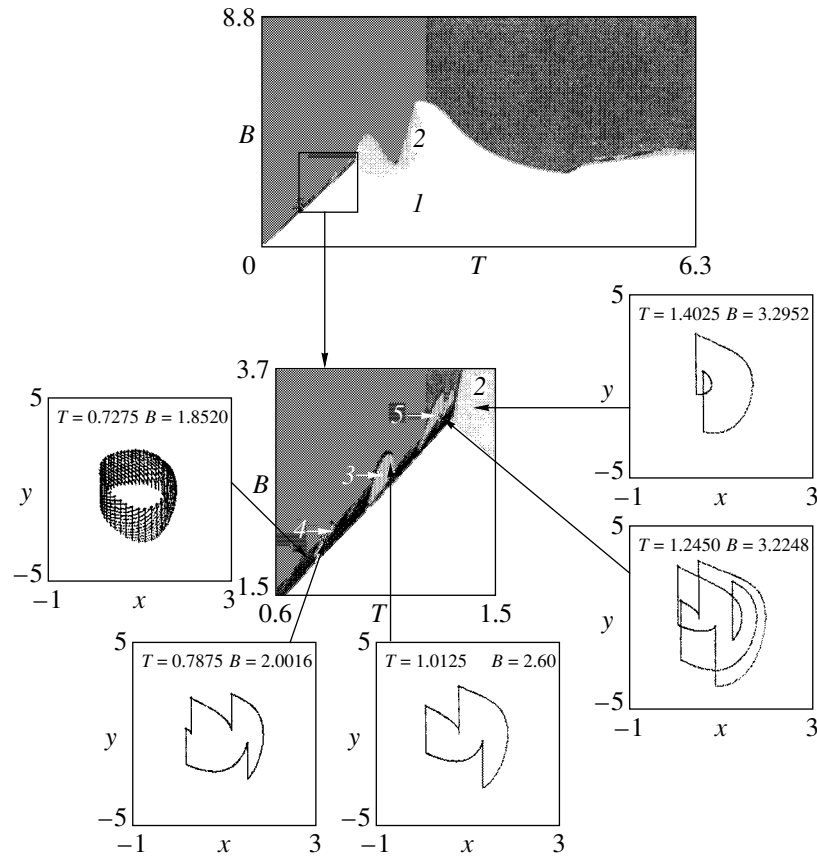**Fig. 1.** The phase portrait of an autonomous system.

Fig. 2. The map of dynamic regimes of the differential equation (1) on the plane of parameters B–T for $\lambda = 1.2$ and $\beta = 1.0$. The bottom inset shows the indicated fragment on a greater scale and the corresponding portraits of attractors.

As can be seen from Fig. 2, there are two extended regions, one corresponding to stable motion with period 1 and the other to the runaway of trajectories. This is quite a natural physical result: the external action of a small amplitude drives the imaging point to a stable focus, while the pulses of a large amplitude drive the system beyond the boundaries of unstable cycle (whereby the imaging point goes to infinity). At the same time, there is a very narrow band of stable synchronization regimes separating the two regions. This synchronization band is shown in greater detail in the bottom part of Fig. 2, where the corresponding map fragments are depicted on a greater scale. As can be seen, the band contains quasiperiodic regimes and synchronization domains with periods 2, 3, 4, 5, etc. These regimes are also characterized by the portraits of attractors. The trajectory moves in the vicinity of the unstable limiting cycle of the autonomous system, while the external pulsed signal returns the trajectory to this vicinity. Thus, the system actually features a control situation initiating stable quasiperiodic regimes and the synchronization regimes in the vicinity of an unstable limiting cycle.

REFERENCES

1. M. I. Rabinovich and D. I. Trubetskov, *Introduction to the Theory of Oscillations and Waves* (Nauka, Moscow, 1984).

2. A. Pikovsky, M. Rosenblum, and J. Kurths, *Synchronization* (Cambridge University Press, Cambridge, 2001).

3. S. P. Kuznetsov, *Dynamic Chaos* (Fizmatlit, Moscow, 2001).

Translated by P. Pozdeev

Numerical Investigation of the Supersonic Streamlining of a Body with Cavity in the Presence of Energy Supply in the Incident Gas Stream

L. A. Bazyma

Kharkov Aviation Institute, National Aerospace University, Kharkov, Ukraine
e-mail: bazima@htsc.kipt.kharkov.ua
Received November 18, 2002

Abstract—The effect of external energy supply on the stabilization of streamlining and a change in the aerodynamic drag of a hemispherical body with cavity was studied by numerical methods. © *2003 MAIK "Nauka/Interperiodica"*.

The results of experimental investigations [1–3] showed that an extended region of energy supply with a thermal wake behind is formed in a supersonic jet under the action of a high-power pulsed optical discharge. For a model body (cone, hemisphere) placed in the thermal wake at a distance equal to 1.0–4.0 body diameters from the focal plane of radiation of a CO_2 laser, the aerodynamic drag was decreased by a factor of up to two at the laser pulse repetition rate of 100 kHz [3]. In the interval of laser pulse repetition rates from 10 to 100 kHz and a radiation frequency of 100 kHz, the thermal wake was continuous [3].

The effect of a pulsed thermal source on the supersonic streamlining of a hemisphere was theoretically modeled in [4] using an explicit TVD method in the Chakravarty formulation [5, 6]. In the case of $M = 3$, $\gamma = 1.4$, and a constant bulk density of the energy supply, the aerodynamic load upon the body exhibited a decrease. A pulse repetition rate corresponding to a minimum drag was determined and it was concluded that the regime of pulsed energy supply can be more effective than a stationary regime [4].

An analysis of the results reported in [1–4, 7] shows that the pulse repetition rate, the power supplied to the stream, and the size of the energy supply zone may significantly influence both the pressure distribution over the model body surface and the regime of streamlining.

As is known, the supersonic streamlining of bodies with cavities in the front art is accompanied by pulsation [8, 9]. The possibility of stabilizing the flow by using a stream injected from the cavity bottom was considered previously [10]. In this study, the effect of external energy supply at a given bulk density on the stabilization of supersonic streamlining and a change in the aerodynamic drag of a hemispherical body with cylindrical cavity was modeled by numerical methods.

Let us consider the established (quasiperiodic) axisymmetric streamlining of a hemisphere with cylindrical cavity by a homogeneous supersonic stream of the ideal gas under the conditions $r_{cav}/R = 0.3$, $l_{cav}/R = 0.954$, and $l_{cav}/r_{cav} = 3.18$ (here, r_{cav} is the cavity radius, l_{cav} is the cavity length, and R is the radius of the hemisphere). A pulsed energy supply source begins to operate in the incident stream in front of the sphere at the initial time ($t = 0$).

In a cylindrical coordinate system, the equations of gasdynamics can be written as follows:

$$\frac{\partial \rho r}{\partial t} + \frac{\partial \rho u r}{\partial x} + \frac{\partial \rho v r}{\partial r} = 0, \tag{1}$$

$$\frac{\partial \rho u r}{\partial t} + \frac{\partial (p + \rho u^2) r}{\partial x} + \frac{\partial \rho u v r}{\partial r} = 0, \tag{2}$$

$$\frac{\partial \rho v r}{\partial t} + \frac{\partial \rho u v r}{\partial x} + \frac{\partial (p + \rho v^2) r}{\partial r} = p, \tag{3}$$

$$\frac{\partial \rho e r}{\partial t} + \frac{\partial \rho u (e + p/\rho) r}{\partial x} + \frac{\partial \rho v (e + p/\rho) r}{\partial r} = \rho q r, \tag{4}$$

where p is the pressure, ρ is the density, u and v are the velocity components in the x and r axes (the tangential component with respect to the φ angle is assumed to be zero), e is the total energy per unit mass of the gas, q is the energy supplied from the external source per unit mass of the gas, and t is the current time. The above system of equations is closed by the equation of state of the ideal gas:

$$p = (\gamma - 1) \rho e.$$

The energy supply was set as [4]

$$q = W(x, r) \sum_{n=1}^{\infty} \frac{1}{f} \delta \left(t - \frac{n}{f} \right),$$

where δ is the Dirac delta, f is the pulse repetition rate, and W is the average bulk density of the energy supply.

In contrast to [4], the latter quantity was taken in a modified form that allows various types of the thermal spot to be modeled:

$$W = W_0\left(\frac{p_\infty}{\rho_\infty}\right)^{3/2}\frac{1}{R}\exp\left(-\frac{k_1 r^2 + k_2(x - x_0)^2}{L^2}\right),$$

where W_0, k_1, and k_2 are some constants determining the supplied energy density and the thermal spot shape.

The system of equations (1)–(4) was solved by the Godunov method [11] on a 110×60 lattice with lattice site density increased at the model body surface, except for the cavity, where the lattice site distribution was set uniform. The calculations were performed using the same finite difference scheme of the first order as that employed in [10]. Let us introduce the following dimensionless variables:

$$r = \bar{r}R, \quad x = \bar{x}R, \quad t = \bar{t}R/a_\infty, \quad a = \bar{a}a_\infty,$$

$$u = \bar{u}a_\infty, \quad v = \bar{v}a_\infty,$$

$$\rho = \bar{\rho}\rho_\infty, \quad p = \bar{p}\rho_\infty a_\infty^2, \quad W = \bar{W}a_\infty^3/R,$$

where a_∞ is the incident stream velocity.

The initial data in calculations ignoring the energy supply corresponded to the dimensionless parameters of the incident stream:

$$p = p_\infty = 1/\gamma, \quad \rho = \rho_\infty = 1, \quad u = u_\infty = M_\infty,$$

$$v = 0,$$

where γ is the adiabate constant. Here and below, the bars above dimensionless quantities r, x, t, a, u, v, ρ, p, and W are omitted. The boundary conditions represent to the absence of percolation on the body surface and the conditions in the incident flow [11].

Calculations performed for the same parameters as in [4]: $M_\infty = 3$, $\gamma = 1.4$,

$$q = \gamma^{-3/2}W_0\exp\left(-\frac{k_1 r^2 + k_2(x - x_0)^2}{L^2}\right)\sum_{n=1}^{N}\frac{t_n}{n}\delta(t - t_n),$$

$x_0 = -3.5$, $L = 0.5$, $N = 10^2 f^1$, $t_n = nf^{-1}$ for various values of the pulse repetition rate ($1 \le f \le 5$), $k_2 = 1$, $k_1 = 1$ (for a spherical thermal spot) and $k_1 = 4$ (for an ellipsoidal spot), and W_0 in the range from 20 to 500.

The aerodynamic drag was averaged using the expression [4]

$$C(f) = \frac{1}{T}\int_{t_* - T}^{t_*} C_x dt,$$

where $T = 10/f$ and C_x is the current value of the drag:

$$C_x(t) = \frac{4}{\gamma M_\infty^2}\int_0^1 (\gamma p_s - 1)r dr.$$
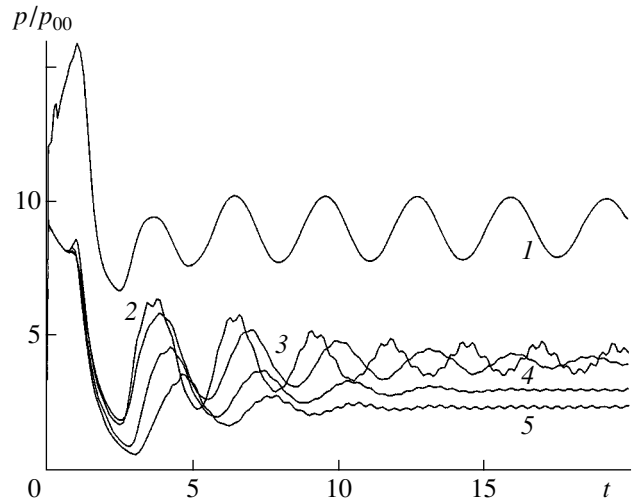
p/p_{00}

Fig. 1. Time variation of the pressure at the center of the cavity bottom (*1*) without and (*2–5*) with the energy supply: (*2*) $W_0 = 20$, $f = 2.5$, spherical thermal spot; (*3*) $W_0 = 20$, $f = 2.5$, ellipsoidal thermal spot; (*4*) $W_0 = 40$, $f = 2.5$, ellipsoidal thermal spot; (*5*) $W_0 = 80$, $f = 2.5$, ellipsoidal thermal spot.
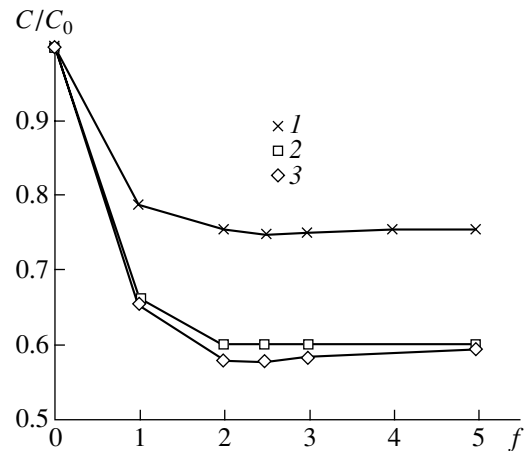

C/C_0

Fig. 2. Plots of the drag C/C_0 versus pulse repetition rate f: (*1*) $W_0 = 20$, ellipsoidal thermal spot; (*2*) $W_0 = 20$, spherical thermal spot; (*3*) $W_0 = 40$, ellipsoidal thermal spot.

Preliminarily, a solution was obtained for the case of a sphere with cylindrical cavity streamlined in the absence of energy supply. The time variation of the pressure at the center of the cavity bottom is presented in Fig. 1 (curve *1*). The character of pulsation and the Strouhal number Sh = 0.245 are close to the values obtained in [10] (Sh = $s/a_0 t^0$, t^0 is the oscillation period, and a_0 is the sound velocity at the drag temperature). In subsequent calculations, this distribution of parameters was used as the initial condition at $t = 0$ for the system with energy supply. A numerical solution was constructed for the time intervals $t_{n-1} < t < t_n$ and $1 \le n \le N$.

The results of calculations showed (Fig. 2) that (similarly to the case of hemisphere studied in [4]) a

minimum drag for the hemisphere with cavity is observed for a pulse repetition rate in the vicinity of $f \approx 2$ at $W_0 =$ const. The effect of the parameter W_0 on the drag behavior was more significant as compared to the influence of the thermal spot size ($C/C_0 \approx 0.58$, $W_0 = 40$, ellipsoidal spot; $C/C_0 \approx 0.59$, $W_0 = 20$, spherical spot; $C/C_0 \approx 0.75$, $W_0 = 20$, ellipsoidal spot; C_0 is the body drag in the absence of external energy supply). The further increase in the value of parameter W_0 showed that the drug variation acquires an asymptotic character (for an ellipsoidal spot, $f = 2.5$ and $W_0 = 500$ corresponds to $C/C_0 \approx 0.28$).

In addition, the thermal spot size and the W_0 value determine the amplitude of pressure pulsation in the cavity. As can be seen in Fig. 1 (curves *2–5*), the passage from spherical spot (curve *2*) to ellipsoidal (curve *3*) for the same $W_0 = 20$ leads to a more pronounced decay of the pressure pulsation amplitude in the cavity. At $W_0 = 40$, the ellipsoidal spot (curve *4*) corresponds to a minimum amplitude of pulsation in a quasiperiodic regime. The further increase in W_0 (curve *5*) results (at a sharper decay of the pressure pulsation) in some increase in the pulsation amplitude in the quasiperiodic regime.

The results described above show that an oscillating source of energy supply can be used as an affective means of acting upon pressure pulsation in the case of streamlined bodies with cavities.

REFERENCES

1. P. K. Tret'yakov, G. P. Grachev, A. I. Ivanchenko, *et al.*, Dokl. Ross. Akad. Nauk **336**, 466 (1994) [Phys. Dokl. **39**, 415 (1994)].

2. P. K. Tret'yakov, G. P. Garanin, G. N. Grachev, *et al.*, Dokl. Ross. Akad. Nauk **351**, 339 (1996) [Phys. Dokl. **41**, 566 (1996)].

3. R. G. Adegren, G. S. Elliot, D. D. Knight, *et al.,* AIAA Papers, No. 2001-0885 (2001).

4. S. V. Guvernyuk and A. B. Samoilov, Pis'ma Zh. Tekh. Fiz. **23** (9), 1 (1997) [Tech. Phys. Lett. **23**, 333 (1997)].

5. S. R. Chakravarthy and S. A. Osher, AIAA Papers, No. 85-0363 (1985).

6. S. R. Chakravarthy, AIAA Papers, No. 86-0243 (1986).

7. P. Yu. Georgievskiĭ and V. A. Levin, Pis'ma Zh. Tekh. Fiz. **14** (8), 684 (1988) [Sov. Tech. Phys. Lett. **14**, 303 (1988)].

8. A. N. Antonov and S. P. Shalaev, Izv. Akad. Nauk SSSR, Mekh. Zhidk. Gaza, No. 5, 180 (1979).

9. D. W. Laoodon, S. P. Schneider, and J. D. Schmisseur, J. Spacecraft Rockets **35** (5), 626 (1998).

10. L. A. Bazyma, Prikl. Mekh. Tekh. Fiz. **36** (3), 69 (1995).

11. S. K. Godunov, A. V. Zabrodin, M. Ya. Ivanov, *et al.*, in *Numerical Solution of Multidimensional Problems in Gasdynamics* (Nauka, Moscow, 1976).

Translated by P. Pozdeev

Optical Properties
of 2-(*p*-Prolinol)-5-nitropyridine–Fullerene System
in the Middle Infrared Range

N. V. Kamanina[a,*], M. O. Iskandarov[b], and A. A. Nikitichev[b]

[a] Vavilov Optical Institute, State Scientific Center of the Russian Federation, St. Petersburg, Russia
* e-mail: kamanin@ffm.ioffe.rssi.ru
[b] Institute of Laser Physics, St. Petersburg, Russia
Received November 22, 2002

Abstract—The optical properties of 2-(*p*-prolinol)-5-nitropyridine (PNP) sensitized with fullerene C_{60} have been studied in the middle IR range ($\lambda = 2940$ nm). It is shown that materials based on the PNP–fullerene system can be used for limiting laser radiation in this spectral range. © *2003 MAIK "Nauka/Interperiodica".*

Good prospects for using 2-(*p*-prolinol)-5-nitropyridine (PNP) in optoelectronics were demonstrated in [1–4], where the electrooptical characteristics of the PNP-based structures were studied, high values of the nonlinear permittivity were found, the possibility of harmonic generation was established, and the temperature dependence of relaxation times was determined. In particular, it was shown [3] that thin films of PNP-based organic compositions grown from melt are promising materials for obtaining optical waveguides. The results of comparative study of these materials and other analogous media by DSC and dielectric relaxation spectrometry were reported in [4].

Previously [5], nonlinear transmission in a PNP–fullerene system was studied in the visible spectral range ($\lambda = 532$ nm), some laws and mechanisms of the optical limitation of laser radiation were established, and it was pointed out that PNP-based organic systems sensitized with fullerenes can be used for optical attenuation purposes. Here, we report on the results of investigation of the nonlinear transmission of a PNP–C_{60} structure in the middle IR range ($\lambda = 2940$ nm) with a view to creating nonlinear absorbers of laser radiation in this spectral range.

The experiments were performed with the above photosensitive compositions in the form of 3% solutions in tetrachloroethane, which were sensitized by fullerene C_{60} added to a concentration of 0.1–3 wt %. The optical absorption measurements were performed for these solutions (in a 10-mm-thick cell) and related PNP-based thin films prepared using a nonphotosensitive polyimide (PI-81A) as the plasticizing agent increasing the film-forming properties of solutions (PNP/PI-81A concentration ratio, 2 : 1). The films were applied by centrifuging onto quartz substrates or onto BaF_2 substrates with preliminarily deposited conducting layers (necessary for the subsequent photoconductivity measurements). The sample film thicknesses was varied within 1–3 μm. For the comparative tests, we also prepared thin films of PI-81A and a composition of this polyimide containing 1 wt % of fullerene C_{60}.

The optical absorption spectra were measured on a Perkin-Elmer Lambda-9 spectrophotometer in a wavelength range from 200 to 3000 nm. The attenuation of laser radiation in the fullerene-containing media described above was studied using a single-pass scheme [6]. The radiation source was a pulsed Er^{3+}:YAG laser operating at a wavelength of 2940 nm and a pulse duration of 500 μs. The laser spot diameter on a sample was ~3.5 mm. We have measured the laser beam energy incident onto and transmitted through the sample. The incident radiation energy was varied with the aid of calibrated optical filters. The input and output signals were directly measured using laser radiation detectors.

Figure 1 shows the optical absorption spectrum of a thin fullerene-sensitized PNP film grown from a tetrachloroethane solution, in comparison to the spectra of pure and fullerene-containing PI-81A and fullerene-free PNP + PI-81A composition. As can be seen, the peak of absorption of a thin film of PNP sensitized with fullerene C_{60} is clearly detected close to the wavelength of the laser radiation employed ($\lambda = 2940$ nm).

Figure 2 shows the plots of output radiation energy density (W_{in}) versus input energy density (W_{in}) for the solutions and thin films of PNP sensitized with fullerene C_{60}. Here, the main plot *1* corresponds to the transmission of a 10-mm cell with PNP–1 wt % C_{60} solution, while curve *2* in the inset shows the transmission of a fullerene-sensitized PNP-based film. As can be seen, all the fullerene-containing media exhibit attenuation (4-fold for the solution and 1.5-fold for the film) of the laser beam at an incident energy density
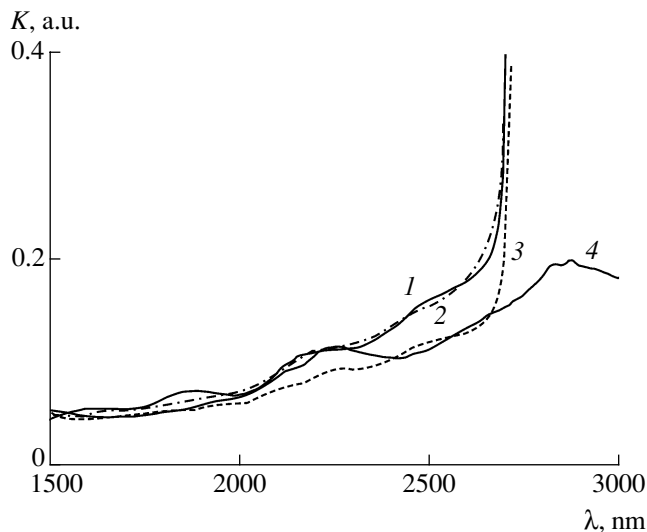
Fig. 1. The optical absorption spectra of thin films grown from tetrachloroethane solution: (*1*) pure polyimide (PI-81A); (*2*) PI-81A + 1 wt % C_{60}; (*3*) PNP + PI-81A; (*4*) PNP + 1 wt % C_{60} + PI-81A.
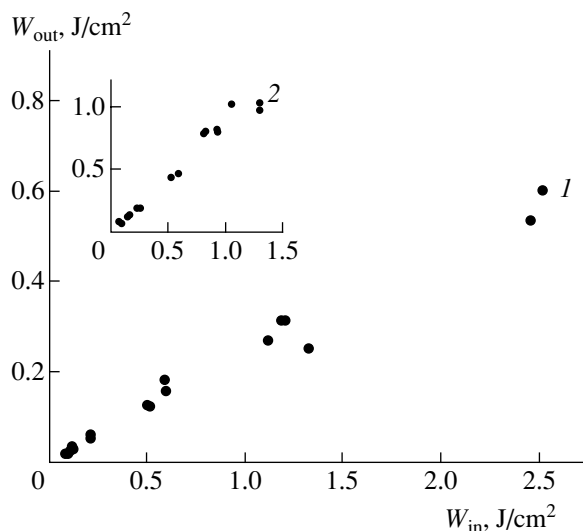

Fig. 2. The plots of output radiation energy density (W_{out}) versus input energy density (W_{in}) at $\lambda = 2940$ nm for (*1*) a solution of PNP + 1 wt % C_{60} and (*2*) a thin fullerene-containing film of the same composition (PNP to PI-81A plasticizer ratio, 2 : 1).

exceeding the level of 0.9–1 J/cm². It should be noted that the transmission of solutions in the interval of incident energy densities between ~1.5 and 2.5 J/cm² was measured using a laser spot size on the sample reduced to 1 mm with the aid of a condenser lens. Visual examination revealed no significant changes in the sample structure, although the laser-induced heating of the medium in the indicated range of incident energy densities must obviously lead to more pronounced aggregation of particles in fullerene solutions.

Therefore, the large degree of attenuation observed for the fullerene-containing PNP solution studied is probably related to the phenomenon of light-induced scattering, which is known to be pronounced for fullerene solutions in various solvents [7]. However, in addition to this phenomenon, it is necessary to take into account peculiarities in the spectral properties and molecular structure of PNP. Indeed, PNP molecules are structurally close to those of 2-cyclooctylamino-5-nitropyridine, the nonlinear optical properties of which were recently demonstrated in [8–10]. Both these organic molecules contain NO_2 acceptor groups bound to benzene rings. While isolated NO_2 molecules or radicals are characterized by an electron affinity energy of 2.3 eV, the electron affinity of an NO_2 group bound to a benzene ring is as low as 0.54 eV [11], which is less than one-fourth of the value for fullerene C_{60}. Thus, we may expect that the fullerene-containing PNP system may features complex formation between PNP matrix and fullerene molecules.

Data on the photoconductivity, obtained by measuring the current–voltage characteristics of fullerene-sensitized PNP films, also do not exclude this possibility. The characteristics of fullerene-free and C_{60}-sensitized PNP films are presented in the table. The current–voltage characteristics were measured using samples with the second electrode formed by depositing gold contacts onto the upper film surface. The contact area was varied so as to exclude the related error of photoconductivity measurements. As can be seen from these data, the fullerene-sensitized samples exhibit an almost tenfold increase in the photoconductivity as compared to that of the fullerene-free films.

Since the charge carriers can be delocalized upon transfer to the fullerene molecules [12], the very fact of increasing photoconductivity in the fullerene-sensitized samples can be indicative of the presence of free carriers. The optical absorption related to these carriers must be taken into account in analysis of the transmission of fullerene-containing media.

For the adequate interpretation of data, involving verification of the complex formation in the PNP–fullerene structure and making allowance for the additional absorption in this system due to this complexation process, it is necessary to perform quantum-chemical calculations aimed at determining the role of fullerene (donor versus acceptor) in organic structures of this type. However, even the first experimental results allow us to conclude that there are several mechanisms responsible for the optical attenuation of IR radiation in the structures studied.

For definiteness, let us estimate the probability of nonlinear effects in a PNP–fullerene structure exposed to laser radiation with an energy density of ~2.5 J/cm² and a laser pulse duration of 500 µs. As is known, realization of the high-frequency Kerr effect requires illumination intensity on a level of intraatomic electric field strength (E_{at}) of the given medium [13]. In partic-

Current–voltage characteristics of thin PNP films with and without fullerene C_{60}

Bias voltage, V	Current, A			
	Pure PNP		PNP + 1 wt % C_{60}	
	dark	light	dark	light
3	$\sim 10^{-12}$	0.2×10^{-11}	0.5×10^{-11}	0.8×10^{-11}
5	$\sim 10^{-12}$	0.4×10^{-11}	0.7×10^{-11}	0.93×10^{-11}
10	0.5×10^{-11}	0.9×10^{-11}	0.8×10^{-11}	1.2×10^{-11}
15	0.55×10^{-11}	0.92×10^{-11}	0.99×10^{-11}	2.0×10^{-11}
20	0.7×10^{-11}	0.95×10^{-11}	1.2×10^{-11}	0.37×10^{-10}
30	0.65×10^{-11}	0.98×10^{-11}	1.25×10^{-11}	0.6×10^{-10}
40	0.8×10^{-11}	0.12×10^{-10}	1.5×10^{-11}	0.76×10^{-10}
50	0.83×10^{-11}	0.2×10^{-10}	1.53×10^{-11}	0.97×10^{-10}

ular, $E_{at} = e/a^2 = 2 \times 10^7$ esu for the electron charge $e = 4.8 \times 10^{-10}$ esu and the Bohr radius $a = 0.5 \times 10^{-8}$ cm. Under the experimental conditions studied, the electric field strength E in the light wave can be determined by the formula $E = \sqrt{8\pi I/c}$, where I is the illumination intensity and c is the speed of light; for $I = 0.5 \times 10^4$ W/cm^2 $= 0.5 \times 10^{11}$ esu and $c = 3 \times 10^{10}$ cm/s, this yields $E = 6.5$ esu. Thus, $E/E_{at} \approx 3.25 \times 10^{-7}$ and, hence, the contribution of a nonlinear component at the radiation intensities studied ($\sim 10^4$ W/cm^2) is relatively small. However, the nonlinear effect can exhibit a buildup as a result of accumulation in the course of the light wave propagation. Thus, for a more significant manifestation of the nonlinear attenuation effect, it is necessary to perform investigations using either a shorter laser pulse duration or a scheme with multiple light wave passage through the organic structure studied.

The results of our first experiments at $\lambda = 2940$ nm can be used for creating nonlinear optical absorbers for the middle IR range and spatial light modulators based on fullerene-sensitized PNP structures.

REFERENCES

1. M. Eich, H. Looser, D. Y. Yoon, et al., J. Opt. Soc. Am. B **6**, 1590 (1989).

2. G. Lahajnar, I. Zupančič, R. Blinc, et al., Z. Phys. B **95**, 243 (1994).

3. A. Leyderman, Y. Cui, and B. G. Penn, J. Phys. D: Appl. Phys. **31**, 2711 (1998).

4. Y. Cui, J. Wu, N. Kamanina, et al., J. Phys. D: Appl. Phys. **32**, 3215 (1999).

5. N. V. Kamanina, Pis'ma Zh. Tekh. Fiz. **27** (12), 65 (2001) [Tech. Phys. Lett. **27**, 515 (2001)].

6. V. P. Belousov, I. M. Belousova, V. P. Budtov, et al., Opt. Zh. **64** (12), 3 (1997).

7. V. P. Belousov, I. M. Belousova, E. A. Gavronskaya, et al., Opt. Spektrosk. **87**, 845 (1999) [Opt. Spectrosc. **87**, 772 (1999)].

8. N. V. Kamanina, Opt. Spektrosk. **90**, 1026 (2001) [Opt. Spectrosc. **90**, 931 (2001)].

9. N. V. Kamanina, J. Opt. A: Pure Appl. Opt. **3**, 321 (2001).

10. N. V. Kamanina, J. Opt. A: Pure Appl. Opt. **4**, 571 (2002).

11. L. V. Gurvich, G. V. Karachevtsev, V. N. Kondrat'ev, et al., *Energies of Chemical Bond Breakage, Ionization Potentials, and Electron Affinity* (Nauka, Moscow, 1974).

12. K. Hosoda, R. Tada, M. Ishikawa, and K. Yoshino, Jpn. J. Appl. Phys., Part 2 **36** (3B), L372 (1997).

13. S. A. Akhmanov and S. Yu. Nikitin, *Physical Optics* (Mosk. Gos. Univ., Moscow, 1998).

Translated by P. Pozdeev

On the Incorrectness of the Traditional Proof of the Prigogine Principle of Minimum Entropy Production

M. M. Mamedov

Center of Physicomathematical Research, Turkmenian State University, Ashgabat, Turkmenia
e-mail: Nazarov@online.tm
Received November 18, 2002

Abstract—It is demonstrated that the traditional proof of the Prigogine principle of minimum entropy production is incorrect. Provided that the Onsager reciprocal relations are satisfied, the Prigogine principle is valid when and only when generalized thermodynamic fluxes are simultaneously equal to zero at nonzero values of the generalized thermodynamic forces. © 2003 MAIK "Nauka/Interperiodica".

More than half a century has passed since the principle of minimum entropy production was formulated by Prigogine in 1945. Nevertheless, both scientific publications and textbooks still use variants of the incorrect proof originally proposed by Prigogine [1]. Below, this proof is reproduced in full, with the subscripts T and M replaced by 1 and 2, respectively.

Consider the entropy (S) buildup as a process corresponding to the transfer of substance and energy between two phases with different temperatures. This process is described by the equation

$$\frac{d_i S}{dt} = J_1 X_1 + J_2 X_2 > 0 \qquad (1)$$

and the phenomenological relations

$$J_1 = \gamma_{11} X_1 + \gamma_{12} X_2, \qquad (2)$$

$$J_2 = \gamma_{21} X_1 + \gamma_{22} X_2. \qquad (3)$$

In a stationary state,

$$J_2 = \gamma_{21} X_1 + \gamma_{22} X_2 = 0. \qquad (4)$$

Taking into account that $\gamma_{12} = \gamma_{21}$, we obtain from relation (1)

$$\frac{d_i S}{dt} = \gamma_{11} X_1^2 + 2\gamma_{21} X_1 X_2 + \gamma_{22} X_2^2 > 0 \qquad (5)$$

or

$$\frac{\partial}{\partial X_2}\left(\frac{d_i S}{dt}\right)_{X_1} = 2(\gamma_{21} X_1 + \gamma_{22} X_2) = 2J_2 = 0. \qquad (6)$$

Then, the two conditions

$$J_2 = 0 \quad \text{and} \quad \frac{\partial}{\partial X_1}\left(\frac{d_i S}{dt}\right)_{X_1} = 0 \qquad (7)$$

are completely equivalent.

Let us critically analyze this proof. First, note that, generally speaking, relation (1) must be replaced by a more adequate relation

$$\frac{d_i S}{dt} = J_1 X_1 + J_2 X_2 \geq 0. \qquad (8)$$

Second, for the stationary state (4), we find upon correct reasoning that, for $\gamma_{12} = \gamma_{21}$,

$$\frac{d_i S}{dt} = \gamma_{11} X_1^2 + 2\gamma_{21} X_1 X_2 + \gamma_{22} X_2^2$$
$$= \frac{\gamma_{22}(\gamma_{11}\gamma_{22} - \gamma_{21}^2)}{\gamma_{21}^2} X_2^2 \qquad (9)$$

or

$$\frac{\partial}{\partial X_2}\left(\frac{d_i S}{dt}\right) = \frac{2\gamma_{22}(\gamma_{11}\gamma_{22} - \gamma_{21}^2)}{\gamma_{21}^2} X_2. \qquad (10)$$

Thus, one can readily see that, taking into account (10), the two conditions (7) are not completely equivalent. In fact, for $\gamma_{22} > 0$ and $\gamma_{21} \neq 0$, completely equivalent are the conditions

$$J_1 = 0, \quad J_2 = 0, \quad \text{and} \quad \frac{\partial}{\partial X_2}\left(\frac{d_i S}{dt}\right) = 0. \qquad (11)$$

According to relation (10), the condition

$$\frac{\partial}{\partial X_2}\left(\frac{d_i S}{dt}\right) = 0 \qquad (12)$$

for $\gamma_{22} > 0$ and $\gamma_{21} \neq 0$ leads to the relation

$$\gamma_{11}\gamma_{22} - \gamma_{21}^2 = 0. \qquad (13)$$

Therefore, in order to ensure the existence of a nontrivial solution of Eqs. (2) and (3) for $\gamma_{12} = \gamma_{21}$, it is necessary and sufficient to obey the conditions

$$J_1 = 0 \quad \text{and} \quad J_2 = 0. \tag{14}$$

Conditions (14) imply that, provided that the Onsager reciprocal relations are satisfied, the Prigogine principle is valid when and only when generalized thermodynamic fluxes are simultaneously equal to zero at nonzero values of the generalized thermodynamic forces.

The above analysis can also be performed in the general case, when the number of generalized thermodynamic fluxes is n, by using the theory of matrices and determinants.

Thus, the traditional proof of the Prigogine principle, according to which the entropy production in a stationary state of a complex dissipative system is minimum and nonzero, is incorrect.

Therefore, the Prigogine principle in the traditional formulation is incorrect as well; that is, the entropy production in a stationary state of a linear dissipative system, while being minimum, cannot differ from zero.

REFERENCES

1. I. Prigogine, *Introduction to Thermodynamics of Irreversible Processes* (Interscience, New York, 1968; Russ. transl. of earlier ed.: IL, Moscow, 1960).

Translated by P. Pozdeev

Modulation Instability of Electromagnetic Excitations in the Josephson Junction in a Thin Superconducting Film

A. I. Lomtev

Donetsk Physicotechnical Institute, National Academy of Sciences of Ukraine, Donetsk, Ukraine
e-mail: lomtev@kinetic.ac.donetsk.ua
Received December 9, 2002

Abstract—The modulation instability of plane nonlinear electromagnetic waves with finite amplitudes excited in the Josephson junction in a thin superconducting film has been studied within the framework of nonlocal electrodynamics. A dispersion equation for the increment of the wave amplitude perturbation is obtained, and the regions of the modulation instability development for the waves studied are determined. It is shown that, for the longwave amplitude perturbations, the modulation instability of these waves is developed within a finite region of wavevectors $0 < Q < Q_v$, while the waves with $Q \geq Q_v$ are stable. © 2003 MAIK "Nauka/Interperiodica".

Arising long ago, the interest of researchers in studying various phenomena related to the wave instability in nonlinear systems and media has never decreased [1, 2]. As is known, compression of a nonlinear wave can take place both across and along the direction of wave propagation. Examples are offered by the self-focusing of light as predicted by Askar'yan [3] and the development of instabilities of the types of wave separation into packets and the wave packet self-compression (modulation instability) originally studied by Lighthill [4].

The modulation instability of electromagnetic waves excited in distributed Josephson junctions is described in terms of the instability of solutions of the corresponding sine-Gordon equations. Besides theoretical interest, the phenomenon of modulation instability has a number of applications. For example, this phenomenon is used for generating trains of ultrashort optical pulses at a high repetition rate and for developing new logical devices.

In many cases, the modulation instability has to be studied using spatially nonlocal modifications of the corresponding sine-Gordon equation [5–16]. Since the system geometries in the problems studied are different, the corresponding electrodynamic equations of the Josephson junctions differ in the type of kernel of the integral operator describing the spatially nonlocal coupling effects. However, the spatially nonlocal character of equations for the phase difference in all cases arises due to the nonlocal coupling of magnetic fields at the interface and in the bulk superconductor. This is a universal reason for spatial nonlocality to arise in electrodynamics of the Josephson junctions, where the nonlocality is a rule rather than exception. For example, Abdullaev [17] studied the modulation instability of a plane nonlinear electromagnetic wave with finite

amplitude at the Josephson frequency. The instability was related to the buildup of small amplitude perturbations and led to separation of the wave into packets.

In this context, it would be even more important to study the development of modulation instability in the case of nonlinear electromagnetic waves propagating in a Josephson junction in a thin superconducting film. To our knowledge, this problem has not been studied so far.

One type of nonlinear system in which the modulation instability can develop is a Josephson junction in an ultrathin superconducting film with a thickness much smaller than the wavelength ($d \ll \lambda$). In this case, the dynamics of phase difference $\varphi(x, t)$ between the junction interfaces are described by a nonlinear integro-differential sine-Gordon equation with spatial nonlocality [10],

$$
\sin\varphi(x, t) + \frac{1}{\omega_J^2}\frac{\partial^2 \varphi(x, t)}{\partial t^2}
$$
$$
= l_J \int_{-\infty}^{\infty} dx' K\left(\frac{x - x'}{2\lambda_{\text{eff}}}\right)\frac{\partial^2 \varphi(x', t)}{\partial x'^2}. \tag{1}
$$

Here, ω_J is the Josephson frequency, $l_J = \lambda_J^2/\lambda$, λ_J is the Josephson length, $\lambda_{\text{eff}} = \lambda^2/d$ is the Pearl penetration depth, and $K\left(\frac{x - x'}{2\lambda_{\text{eff}}}\right)$ is a nonlocal (with respect to spatial variable) integral kernel

$$
K\left(\frac{x - x'}{2\lambda_{\text{eff}}}\right) = \frac{2\lambda_{\text{eff}}}{\pi}\int_{0}^{\infty} dq \frac{J_0(q(x - x'))}{1 + 2q\lambda_{\text{eff}}}, \tag{2}
$$

where $J_0(qx)$ is the zero-order Bessel function. Note that the nonlinear character of Eq. (1) is related to the

fact that the Josephson current through the junction is a sinusoidal function of the phase difference between the junction interfaces.

Consider the evolution of a plane nonlinear wave (e.g., of the junction breather type) with the Josephson frequency ω_J and a small but finite amplitude. The phase difference $\varphi(x, t)$ can be written in the following form:

$$\varphi(x, t) = u(x, t)\exp(-i\omega_J t) + u^*(x, t)\exp(i\omega_J t),$$
$$|\varphi(x, t)| \ll 1. \tag{3}$$

Let us retain in Eq. (1) only terms of the lowest order in nonlinearity at the main frequency ω_J and restrict the consideration to the approximation of amplitude $u(x, t)$ slowly varying with time, for which $|\partial^2 u(x, t)/\partial t^2| \ll 2\omega_J|\partial u(x, t)/\partial t|$. Substituting relation (3) into Eq. (1), we obtain the following equation for the amplitude:

$$i\frac{2}{\omega_J}\frac{\partial u(x, t)}{\partial t} + \frac{1}{2}|u(x, t)|^2 u(x, t)$$
$$+ l_J\int_{-\infty}^{\infty} dx' K\left(\frac{x - x'}{2\lambda_{\text{eff}}}\right)\frac{\partial^2 u(x', t)}{\partial x'^2} = 0. \tag{4}$$

This is a nonlocal Schrödinger equation possessing an exact solution of the plane wave type with a constant amplitude A:

$$u_0(t) = A\exp(iA^2\omega_J t/4), \quad A \ll 1. \tag{5}$$

Let us study the stability of solution (5). The character of decay of the plane wave of type (5) can be judged from the pattern of development of its small perturbations. Consider a small perturbation in the wave amplitude:

$$u(x, t) = [A + \psi(x, t)]\exp(iA^2\omega_J t/4),$$
$$|\psi(x, t)| \ll A. \tag{6}$$

Using Eq. (4), we obtain a linear equation for the small perturbation $\psi(x, t)$:

$$i\frac{2}{\omega_J}\frac{\partial \psi(x, t)}{\partial t} + \frac{1}{2}A^2[\psi(x, t) + \psi^*(x, t)]$$
$$+ l_J\int_{-\infty}^{\infty} dx' K\left(\frac{x - x'}{2\lambda_{\text{eff}}}\right)\frac{\partial^2 \psi(x', t)}{\partial x'^2} = 0. \tag{7}$$

Putting here $\psi(x, t) = v(x, t) + iw(x, t)$, we arrive at the following system of equations for the real and imaginary parts of the perturbation amplitude:

$$\frac{2}{\omega_J}\frac{\partial v(x, t)}{\partial t} + l_J\int_{-\infty}^{\infty} dx' K\left(\frac{x - x'}{2\lambda_{\text{eff}}}\right)\frac{\partial^2 w(x', t)}{\partial x'^2} = 0,$$
$$-\frac{2}{\omega_J}\frac{\partial w(x, t)}{\partial t} + A^2 v(x, t) + l_J\int_{-\infty}^{\infty} dx' K\left(\frac{x - x'}{2\lambda_{\text{eff}}}\right)\frac{\partial^2 v(x', t)}{\partial x'^2} = 0. \tag{8}$$

For perturbations of the type

$$v(x, t) = V(Q, \Omega)\exp[i(Qx - \Omega t)],$$
$$w(x, t) = W(Q, \Omega)\exp[i(Qx - \Omega t)] \tag{9}$$

(arbitrary perturbations can be represented as superpositions of these), Eqs. (8) give the following dispersion relation $\tilde{\Omega} = \tilde{\Omega}(\tilde{Q})$:

$$\tilde{\Omega}^2 = \frac{L}{2\pi}\tilde{Q}^2 J(\tilde{Q})\left[\frac{2L}{\pi}\tilde{Q}^2 J(\tilde{Q}) - A^2\right], \tag{10}$$

where $\tilde{Q} = 2Q\lambda_{\text{eff}}$, $\tilde{\Omega} = \Omega/\omega_J$, $L = l_J/2\lambda_{\text{eff}}$, and

$$J(\tilde{Q}) = \int_0^{\infty}\frac{dx}{1 + \tilde{Q}\cosh x}$$

or (see [10])

$$J(\tilde{Q}) = \frac{1}{2\sqrt{1 - \tilde{Q}^2}}\ln\frac{1 + \sqrt{1 - \tilde{Q}^2}}{1 - \sqrt{1 - \tilde{Q}^2}} \quad \text{at} \quad \tilde{Q} \le 1,$$

$$J(\tilde{Q}) = \frac{2}{\sqrt{\tilde{Q}^2 - 1}}\arctan\frac{\sqrt{\tilde{Q}^2 - 1}}{1 + \tilde{Q}} \quad \text{at} \quad \tilde{Q} \ge 1. \tag{11}$$

The dispersion equation (10), with relations (11) for the increment of the wave amplitude perturbation, possesses a positive solution $\text{Im}\tilde{\Omega}(\tilde{Q}) > 0$ in the region of wavevectors $0 < \tilde{Q} < \tilde{Q}_v$, where small amplitude perturbations (9) grow with the time and the plane nonlinear electromagnetic wave (5) is subject to modulation instability. In the range of wavevectors $\tilde{Q} \ge \tilde{Q}_v$, we have $\text{Im}\tilde{\Omega}(\tilde{Q}) \equiv 0$, so that the wave is stable. The boundary wavevector $\tilde{Q}_v$ is determined from the equation

$$\tilde{Q}_v^2 J(\tilde{Q}_v) = \frac{\pi A^2}{2L}. \tag{12}$$

The regions of modulation instability of the plane nonlinear electromagnetic wave (5) with a fixed amplitude A and various values of the parameter L are depicted in the figure.
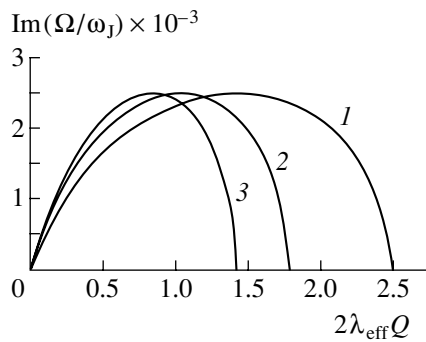
The maximum value of the perturbation increment,

$$(\text{Im}\tilde{\Omega}(\tilde{Q}_m))_{\text{max}} = A^2/4 \tag{13}$$

is attained for the wavevector $\tilde{Q}_m$, which is a solution of the equation

$$\tilde{Q}_m^2 J(\tilde{Q}_m) = \frac{\pi A^2}{4L}. \tag{14}$$

Oscillating at the Josephson frequency, the plane nonlinear electromagnetic wave in the course of the modulation instability development will evolve into a

$\mathrm{Im}(\Omega/\omega_{\mathrm{J}}) \times 10^{-3}$

Regions of modulation instability for a plane nonlinear electromagnetic wave (5) with amplitude $A = 10^{-1}$ and $L = 0.5 \times 10^{-2}$ (*1*), 0.75×10^{-2} (*2*), and 10^{-2} (*3*).

train of pulses (small-amplitude breathers) with a repetition frequency determined by the modulation period of the initial wave: $L_0 = 2\pi/Q$, where $0 < Q < Q_v = \tilde{Q}_v/2\lambda_{\mathrm{eff}}$.

Thus, we have demonstrated that, for the longwave amplitude perturbations, the modulation instability of a plane nonlinear electromagnetic wave (5) is developed within a finite region of wave vectors $0 < Q < \tilde{Q}_v$. For the amplitude perturbations $Q \geq \tilde{Q}_v$, the nonlinear wave is stable. Experimentally, the development of modulation instability can be observed in extended Josephson junctions in thin superconducting films, in which electromagnetic waves with small but finite amplitude are excited at the Josephson frequency.

REFERENCES

1. V. I. Karpman, *Nonlinear Waves in Dispersive Media* (Nauka, Moscow, 1973).
2. B. B. Kadomtsev, *Nonlinear Phenomena in Plasma* (Nauka, Moscow, 1976).
3. G. A. Askar'yan, Zh. Éksp. Teor. Fiz. **42**, 1567 (1962) [Sov. Phys. JETP **15**, 1088 (1962)].
4. M. J. Lighthill, J. Inst. Math. Appl. **1**, 269 (1965).
5. Yu. M. Aliev, V. P. Silin, and S. A. Uryupin, Sverkhprovodimost **5** (2), 228 (1992).
6. A. Gurevich, Phys. Rev. B **46**, 3187 (1992).
7. Yu. M. Ivanchenko and T. K. Soboleva, Pis'ma Zh. Éksp. Teor. Fiz. **51**, 100 (1990) [JETP Lett. **51**, 114 (1990)].
8. Yu. M. Ivanchenko and T. K. Soboleva, Phys. Lett. A **147**, 65 (1990).
9. Yu. M. Ivanchenko and T. K. Soboleva, Fiz. Tverd. Tela **32**, 2029 (1990) [Sov. Phys. Solid State **32**, 1181 (1990)].
10. R. G. Mints and I. B. Snapiro, Phys. Rev. B **51**, 3054 (1995).
11. A. I. Lomtev, Pis'ma Zh. Éksp. Teor. Fiz. **69**, 132 (1999) [JETP Lett. **69**, 148 (1999)].
12. A. I. Lomtev, Fiz. Tverd. Tela (St. Petersburg) **42**, 16 (2000) [Phys. Solid State **42**, 15 (2000)].
13. A. I. Lomtev, Zh. Tekh. Fiz. **70** (9), 63 (2000) [Tech. Phys. **45**, 1159 (2000)].
14. I. O. Kulik and I. K. Yanson, *Josephson Effect in Superconducting Tunneling Structures* (Nauka, Moscow, 1970).
15. Yu. E. Kuzovlev and A. I. Lomtev, Zh. Éksp. Teor. Fiz. **111**, 1803 (1997) [JETP **84**, 986 (1997)].
16. A. I. Lomtev, Zh. Éksp. Teor. Fiz. **113**, 2256 (1998) [JETP **86**, 1234 (1998)].
17. F. Kh. Abdullaev, Pis'ma Zh. Tekh. Fiz. **23** (2), 8 (1997) [Tech. Phys. Lett. **23**, 52 (1997)].

Translated by P. Pozdeev

Structural Changes in the Surface Layers of an EK79-ID Alloy upon Hardening Treatments

D. V. Pavlenko, S. V. Loskutov*, V. K. Yatsenko, and N. V. Gonchar

Zaporozhye National Technical University, Zaporozhye, Ukraine
* e-mail: svl@zstu.edu.ua
Received November 1, 2002

Abstract—Experimental data showing variation of the mechanical properties of the surface layer of a nickel-based EK79-ID alloy depending on the degree of surface straining are presented. The elastic modulus and the proof stress of the surface layer exhibit nonmonotonic variation with the degree of straining. The possible mechanisms determining changes in the elastic modulus in the course of the surface structure variation caused by the strain hardening are considered. © *2003 MAIK "Nauka/Interperiodica".*

As is known, the state of the surface layer determines to a significant extent the loading capability of metal details operating under conditions of reversal loading. In connection with this, most methods used to increase the fatigue resistance of metals and alloys are aimed first at obtaining favorable characteristics of the surface layers.

Among various quantities characterizing the surface layer upon hardening by surface plastic deformation, a special place belongs to the elastic modulus and yield stress. Taking into account that data on the mechanical properties of the surface layers of heat-resistant nickel-based alloys of the EK79-ID type and their dependence on the degree of plastic deformation upon strain hardening are virtually not available in literature, it was important to fill this gap.

The mechanical properties of the surface layer were studied on plates of an EK79-ID alloy strain hardened by treating with metal balls in an ultrasonic installation. The degree of surface straining was determined by measuring the microhardness with a PMT-3 device on the samples before and after the treatment. The elastic and plastic characteristics of the sample surface in the initial state and upon strain hardening were studied by the kinetic indentation technique [1, 2], assuming a linear relation between the contact elastic modulus and the tensile modulus [3, 4]. Under this assumption, the elastic modulus of the surface layer was calculated by an expression for the contact elastic modulus, using experimental values of the time, load, and contact electric resistance measured in the course of interaction of a metal indenter with the sample.

The data were interpreted using the solution of the Hertz problem for the elastic interaction of two bodies. A relation between the contact electric resistance and the real contact surface area was established using preliminary kinetic indentation tests on single crystal niobium samples. The values of kinetic hardness of a thin surface layer were determined in the course of continuous pressing of a spherical indenter into a sample, by monitoring the load and measuring the contact area. With allowance of the testing device rigidity, the depth of the indenter penetration into the surface layer of the alloy studied fell within 48–53 μm.

The experimental plots of the elastic modulus and the conventional yield stress versus the degree of surface straining are presented in the figure. As can be seen, a minimum value of the proof stress is observed for the initial samples. The surface hardening at a degree of straining not exceeding 50% leads to an increase in the proof stress and, accordingly, in the fatigue limit. However, as the degree of straining increases further, the proof stress exhibits a significant decrease, probably as a result of the so-called overstraining accompanied by the loss of material integrity and the formation of microscopic cracks.

The character of variation of the elastic modulus in the surface layer is opposite to that observed for the
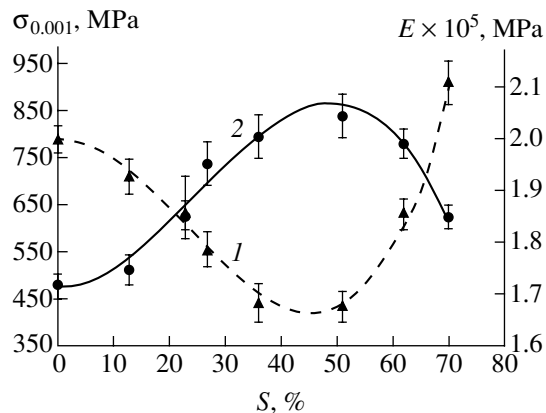
Plots of the (*1*) elastic modulus and (*2*) proof stress versus the degree of surface straining for a nickel-based EK79-ID alloy.

proof stress. This is related to the fact that surface plastic deformation leads to an increase in the density of crystal defects (weakly bound atoms) reducing the elastic modulus. At the same time, a residual microplastic deformation is accumulated and a plane-stressed state is formed in the subsurface material layer. The X-ray diffraction analysis showed that the ultrasonic metal ball treatment gives rise to residual compressive macrostresses in the samples. These macrostresses elastically deform the crystal lattice to make the atoms closer spaced in the sample plane, which accounts for the increase in the elastic modulus. Thus, the alloy subject to surface plastic deformation is under the action of two opposite factors, increasing and decreasing the elastic modulus.

The observed variation in the elastic modulus is equivalent to a change in the interatomic distance upon heating the EK79-ID allow up to about 400°C [5]. Assuming for this alloy $\alpha = 13 \times 10^{-6}$ K^{-1}, the relative deformation of the crystal lattice upon such heating amounts to $\varepsilon = \Delta a/a = 0.005$. According to the X-ray diffraction measurements using the (330) reflection for the alloy sample with a 70% surface straining, $\varepsilon = -\cot\theta\,\Delta\theta = 0.002$. Thus, the kinetic indentation technique provides an overestimated increment of the elastic modulus. By its physical meaning, the elastic modulus characterizes the strength of interatomic bonds and significantly depends on the crystallographic orientation. As is known, the elastic moduli of metals are weakly sensitive with respect to the structure but significantly change with increasing anisotropy of a strained metal. In the case under consideration, straining takes place in a thin subsurface layer with a free boundary, in which the deformation process exhibit certain peculiarities. Therefore, one possible reason for the observed significant changes in the elastic modulus of the subsurface layer is the development of a special deformation texture.

It is also known that the anisotropic properties of multiphase microstructures can be due to a preferred orientation of some phase. We have studied the microstructure of our samples using a JSM T300 scanning electron microscope operating in the secondary-electron imaging mode at an accelerating voltage of 30 kV. It was established that the size of the hardening γ' phase particles and the average interparticle distance depend on the degree of surface straining. As the degree of straining increases to 50%, the γ' particle size drops by half and their average spacing also decreases to half of the initial value, while the surface density of these particles accordingly increases. This implies that the γ' particles are only subject to fragmentation and dispersion, while the surface area occupied by these species remains unchanged. Since the fragmentation implies plastic deformation, and the fcc metals are known to deform by slippage via (111) type planes in one of the

[110] directions, the formation of a deformation texture becomes quite probable. Thus, these considerations are consistent with the experimentally observed dependence of the elastic modulus on the degree of surface straining.

According to the experimental plot presented in the figure, a sample characterized by higher degree of surface straining in the range below 50% must possess a higher plasticity of the surface layer. A decrease in the elastic modulus observed in this range of surface straining leads to decrease in amplitude of the acting variable stresses in the surface layer. By analogy with the margin of safety formula, the ratio of the proof stress to the elastic modulus can be conditionally considered as the margin of safety for the surface layer:

$$n_1(S) = \frac{\sigma_{0.001}(S)}{E(S)}. \tag{1}$$

Approximating the functions $\sigma_{0.001}(S)$ and $E(S)$ by third-order polynomials, we have obtained a polynomial describing the surface strength of the EK79-ID alloy upon the strain hardening treatment with metal balls (correlation coefficient, $R = 0.98$):

$$n_1(S) = -0.05S^3 + 3.93S^2 - 9.91S + 2312, \tag{2}$$

where S is the degree of surface straining (%).

The results of our experimental study of mechanical properties of the surface layer of a nickel-based EK79-ID alloy revealed a complicated pattern of variation of the elastic modulus as a function of the surface plastic deformation. The possible physical mechanisms responsible for the observed behavior have been analyzed. The tests showed that a maximum efficiency of the surface strain hardening with respect to the elastic modulus and proof stress is achieved for the degree of surface straining in the region of 45–55%.

REFERENCES

1. S. I. Bulychov and V. P. Alekhin, *Testing Metals by the Continuous Indentation Technique* (Mashinostroenie, Moscow, 1990).

2. S. V. Loskutov, *Proceedings of the 3rd Intern. Conf. "Equipment and Technology for the Thermal Processing of Metals and Alloys," September 9–13, 2002, Kharkov*, pp. 32–34.

3. V. T. Troshchenko, V. V. Pokrovskiĭ, and A. V. Prokopenko, *Crack Resistance of Metals under Cyclic Loading Conditions* (Naukova Dumka, Kiev, 1987).

4. A. V. Prokopenko and V. N. Torgov, Probl. Prochn., No. 4, 28 (1986).

5. V. S. Zolotorevskiĭ, *Mechanical Properties of Metals* (Metallurgiya, Moscow, 1983).

Translated by P. Pozdeev

The Atomic Structure of Nanotubes Synthesized from a Carbon Mix of High Reaction Ability

I. I. Bobrinetskiĭ, V. K. Nevolin*, V. I. Petrik,
A. A. Stroganov, and Yu. A. Chaplygin

Moscow State Institute of Electronic Engineering (Technical University), Zelenograd, Russia
Research Institute of Physics of Fullerenes and Advanced Materials, Russian Academy of Natural Sciences, Moscow, Russia
* e-mail: vkn@miee.ru
Received October 23, 2002

Abstract—The surface of carbon nanotubes was studied on an atomic resolution level in a scanning tunneling microscope (STM) operating under atmospheric conditions. The nanotubes were synthesized from a carbon mix of high reaction ability. Factors determining distortion of the STM image are analyzed and the main parameters (chiral angle and diameter) of nanotubes are calculated. © *2003 MAIK "Nauka/Interperiodica".*

Discovered by Iijima in 1991, carbon nanotubes (NT) are now considered by many research groups as a base material for nanotechnology. The interest in NTs, as manifested by extensive research in various directions, is related to the unique electrical and mechanical properties of these structures. Being an allotropic modification of carbon, carbon NTs possess the shape of cylinders bent from one (single-sheet NT) of several (multisheet NT) graphite planes. The NTs exhibit variable properties, which are usually explained proceeding from the geometry of the atomic surface structure determined by the chiral angle Θ and the tube diameter [1].

Here, we report on the properties of NTs synthesized from a highly reactive carbon mixture [2]. The investigation was conducted in a scanning tunneling microscope (STM) operating under atmospheric conditions (in contrast to [1], where the experiments were performed at a cryogenic temperature of ~4 K). Based on the experimental data, we will determine the main geometric parameters (chiral angle and diameter) of NTs synthesized under the conditions studied.

The NT synthesis by cold destruction of natural graphite [2] is a new alternative to the well-known techniques based on the thermal decomposition of graphite in an arc discharge, laser evaporation [3], and chemical vapor deposition [4]. The first direct experimental evidence of the NT formation from a carbon mix of high reaction ability (USVR) produced by cold destruction of natural graphite was presented in [5]. Investigation of a USVR sample in an atomic force microscope confirmed the presence of Y-type NTs (called branched) in the free state [6]. However, the detailed structure of the observed carbon nanofibers with diameters up to several tens of nanometers and a length of up to 20 μm remained unclear. In this study, we have used an STM to characterize, for the first time on an atomic resolu-tion level, the surface of NTs synthesized from a USVR.

The experiments were conducted in a modified STM of the Solver-P47H type (NT-MDT Company, Zelenograd). All measurements were performed in air at room temperature. Replaceable STM head with a scanning device (scan range, 12 μm) was mounted in a shock-protected unit with a special suspension system. STM tips were mechanically cut from a platinum–iridium alloy wire (90% Pt–10% Ir). In order to reduce the level of probe and substrate vibrations during the scan, we employed a specially modified acoustic protection system.

The NTs were isolated from a USVR by conventional methods. The USVR components were separated into smaller fractions by ultrasonic dispersion in a dimethyl alcohol solution. In order to decrease the content of unstable nanodimensional formations (C–C complexes, fragments of graphite planes, and amorphous carbon species), the mixture was washed in nitric acid and annealed for several minutes at 800°C. Undesired coarse USVR fractions were removed in the course of sample preparation to the STM investigation. To this end, the mixture with increased NT content was poured onto a fresh (this is an important circumstance for NT adhesion) cleavage of a pyrolytic graphite substrate. The coarse fragments were removed using an air jet gun.

The STM< measurements were performed in a dc regime with a minimum feedback gain level, simulating the levitating point mode. The voltage between the point and substrate was 20–100 mV, and the current was controlled within 40–200 pA. This large scatter of the parameters is caused by significant differences in the electrical characteristics of NTs, related to the pres-
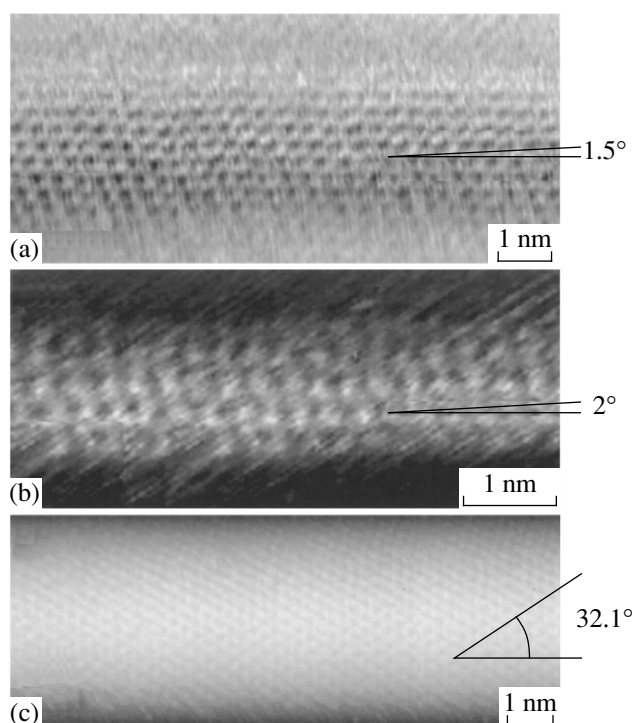
Fig. 1. STM images of carbon nanotubes on an atomic resolution level, showing the structures with (a, b) small and (c) large values of the chiral angle between hexagon rows and the tube axis (see the text for explanations).

In order to provide for the reliability of the STM data, it is necessary first to obtain a high-resolution image of an NT. The chiral angle is measured between the NT axis and most closely packed atomic rows. It is also necessary to take into account a peculiarity of the STM of graphite, whereby the surface structure can be imaged by only a half of the atoms, the orbitals of which overlap with those of the second sublayer [8]. A certain error can be related to the cylindrical shape of NTs, since the result obtained with an STM probe scanning in the dc regime represents a convolution of the probe and NT shapes.

Typical STM images of the surface of several NTs are presented in Fig. 1. These NTs were characterized by the chiral angle, the number of atoms in the cross section perpendicular to the NT axis, and the NT diameter and height. The results of these measurements are listed in the table. The chiral angle of NTs with small diameters is close to zero (Figs. 1a and 1b), to within the experimental error. Note that a hexagonal structure of six atoms is more clearly manifested in Fig. 1a, while the structure in Fig. 1b exhibits a triangular character, being imaged by only half of the atoms actually present on the surface. The phenomenon of appearance and disappearance of the second atomic sublayer is also observed when a flat pyrolytic graphite surface is scanned with variable parameters (voltage and current). These quantities determine the distance between the substrate surface and the probing point tip, thus eventually determining the tunneling electron current distribution in the gap and the character of the STM image. The electrical properties of NTs, determining their conductivity character (semiconducting versus metallic), also influence the above phenomenon. The nanotubes of a large diameter may consist of several layers (Fig. 1c); in this case, even a significant chiral angle (32.1°) does not introduce big perturbations into the STM image of a hexagonal surface structure. Data presented in the table were obtained by directly measuring the diameters and heights of NTs in their visible parts on substrates.

The results of analogous measurements made in [1] were presented with a correction for the scan width changed due to a cylindrical shape of the nanotubes.

ence of adsorbate and in the contact resistance between NT and substrate.

As was noted above, the chiral angle and diameter completely determine the NT surface geometry. In turn, the structure of defect-free NTs determines their electrical properties. According to the general rule, the chiral NTs exhibit metallic properties if the difference $n - m$ (characterizing direction of the chirality vector) is a multiple of three, and semiconductor properties, in all other cases [7]. A change in the chiral angle (by a fraction of degree) and in the NT diameter (by a few Ångströms) may lead to significant changes in the conductivity. This circumstance requires the measurements to be performed at maximum precision.

The characteristics of nanotubes determined from STM images presented in Fig. 1

Nanotube type	Θ, deg	Number of visible atoms	Width, nm	Height, nm	Free nanotube diameter (nm) determined from	
					elliptic cross section on substrate	counted number of atoms
a	1.5	8	2.5	0.43	1.04	1.36
b	2	4	1.8	0.22	0.62	0.63
c	32.1	13	7.0	1.30	3.0	3.17

This shape leads to a variation in the direction of the tunneling current density vector, which results in an increase in the image width. In addition, under the action of a van der Waals force from the substrate, NTs cannot retain their regular form and the NT cross section acquires an oval shape [9]. This assumption is confirmed by the results of measurements of the NT height. The NTs can also be flattened under the action of a force produced by the STM probe. The NT bending may become especially pronounced when the measurements are performed under atmospheric conditions (self-confined tunneling regime).

Some theoretical descriptions [10] offered an analysis of the graphite lattice distortions related to deformation of the atomic planes. It is believed that this distortion is insignificant, amounting to a fraction of percent of the lattice parameter. Thus, the NT diameter can be calculated once the number of atoms accommodated on the circumference (for a nonchiral NT) or on a trajectory most close to circular (on a chiral NT) is known. In the latter case, the result should be projected onto the normal to the tube axis. The error can be related to 1–2 atoms occurring on the side surfaces. The NT diameter can also be estimated assuming that the tube cross section is close to an ellipse. The results of calculations using both methods are given in the table. As can be seen, the experimental diameter to height ratio changes from 8.2 for the narrowest NT to 5.4 for the widest one. The ratio of the calculated diameter of a free nanotube to the experimental height on a substrate varies from 3.2 to 2.3.

Thus, we have demonstrated for the first time STM images obtained in air at an atomic resolution for the NTs synthesized by cold destruction of natural graphite. The STM data are indicative of a significant change in shape of the nanotubes on pyrolytic graphite substrates. Factors responsible for the STM image distortions have been analyzed. Based on the experimental results, the main parameters (chiral angle and diameter) of nanotubes have been calculated.

REFERENCES

1. L. C. Venema, V. Meunier, Ph. Lambin, and C. Dekker, Phys. Rev. B **61**, 2991 (2000).
2. V. I. Petrik, RF Patent No. 2 128 624 (17.10.97).
3. T. Guo, P. Nikolaev, A. Thess, *et al.*, Chem. Phys. Lett. **243**, 49 (1995).
4. H. Kind, J. M. Bonard, K. Hernadi, *et al.*, Langmuir **16**, 6877 (2000).
5. V. V. Minaev, V. K. Nevolin, and V. I. Petrik, Mikrosist. Tekhn., No. 1, 41 (2002).
6. I. I. Bobrinetskiĭ, V. K. Nevolin, and V. I. Petrik, Izv. Vyssh. Uchebn. Zaved., Élektronika, No. 2, 105 (2002).
7. M. S. Dresselhaus, G. Dresselhaus, and P. C. Eklund, *Science of Fullerenes and Carbon Nanotubes* (Academic Press, San Diego, 1996), p. 180.
8. V. S. Edel'man, Prib. Tekh. Éksp. **32** (5), 25 (1989).
9. T. Hertel, R. E. Walkup, and P. Avouris, Phys. Rev. B **58**, 13870 (1998).
10. P. M. Ajayan and T. M. Ebbesen, Rep. Prog. Phys. **60**, 1025 (1997).

Translated by P. Pozdeev

The Fractal Structure of a Carbon Deposit Formed during Graphite Spraying in an Electric Arc

Yu. V. Sokolov and V. S. Zheleznyǐ
Voronezh State Technical University, Voronezh, Russia
e-mail: wwwfalcon@mail.ru
Received October 25, 2002

Abstract—Experimental data obtained by atomic force microscopy showing that a carbon deposit formed during graphite spraying in an electric arc possesses a fractal structure. The deposit is composed of clusters with dimensions on the order of 1–5 nm. The surface and profile of the deposit exhibit a self-affine fractal structure. The fractal dimensions of the deposit surface and profile, as well as the Hurst index characterizing the self-affine fractal, are determined. © *2003 MAIK "Nauka/Interperiodica".*

During the synthesis of fullerenes by the electric arc technique, a carbon deposit appears on the cathode surface. The formation of this product is determined by nonequilibrium conditions (temperature gradient, concentration of carbon atoms) in the system during the electric arc operation. Besides a large number of publications devoted to the synthesis and characterization of fullerenes, there are several papers (see, e.g., [1, 2]) devoted to the microscopic investigation of such carbon deposits. According to Yoshinori [1], the carbon deposit is composed of nanotubes and nanoparticles, whereas Grushko *et al.* [2] obtained a different morphology called "protuberances."

We have studied the surface structure of a carbon deposit obtained under the following conditions. The working chamber of a reactor was evacuated to 10^{-2} Torr and filled with argon or helium (working gas) to a pressure controlled in the range from 10 to 600 Torr. Then a graphite electrode, shaped as a rectangular rod with 5×3 mm cross section and 100 mm length with sharpened end, was brought into contact with another (immobile) graphite electrode with an area of 1.5×1.5 cm to initiate the electric arc. At an applied voltage of 15–20 V, the arc current was on the order of 170–190 A. The duration of arc operation (i.e., the time of carbon deposition on the immobile graphite electrode) was varied from 10 to 180 s. The carbon deposit formed in the region of contact appeared as a silver bright ring with a thickness of 1–3 mm, depending on the arc operation time.
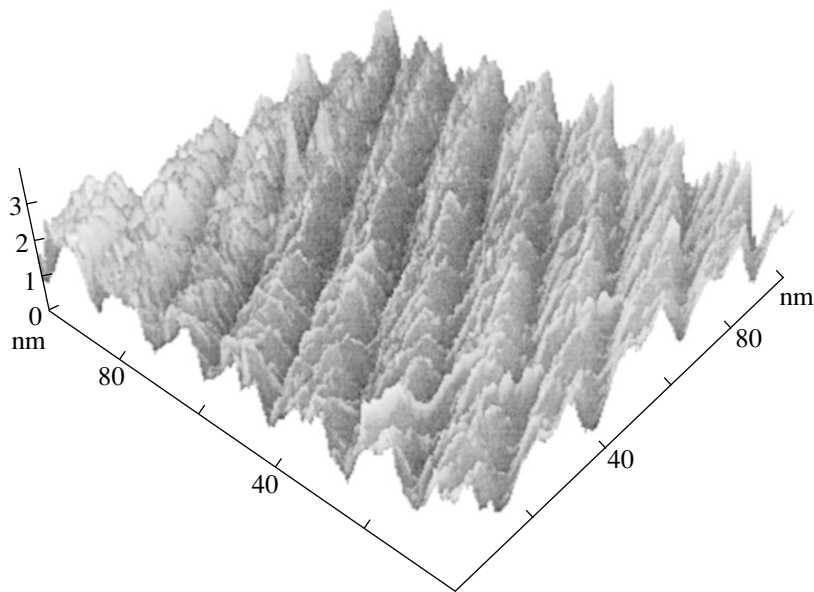

Fig. 1. A typical AFM image of a carbon deposit (scanned area, 100×100 nm).

The surface of the carbon deposit was studied in an atomic force microscope (AFM). Figures 1 and 2 show a typical AFM image of the deposit surface and a profile obtained by scanning the sample surface along a line. As can be seen from these data, the sample surface exhibits extended, well-developed hills and valleys with sharp edges and a width on the order of 20–40 nm. The image also reveals carbon clusters with dimensions about 5 nm, which consist of smaller clusters ~1 nm in size.

No carbon deposits with fractal structures were obtained in [1, 2], where the arc current density was within $j = 169$–372 A/cm^2. We have obtained a deposit at $j = 1000$–1200 A/cm^2. Such a high current density, at which the arc temperature reaches up to 10^4 K, provides for the formation of a carbon deposit possessing a fractal structure. The fractal formations grow by the cluster–cluster aggregation mechanism [3] from carbon clusters with dimensions on the order of a few nanometers, nucleated during a time period of 10^{-4} s in a carbon plasma generated in the interelectrode gap.

By fractal is implied a structure composed of parts similar to the whole. Magnified parts of such an object, while not precisely matching the whole, have proved to be asymptotically self-similar in probabilistic estimates [4]. In constructing fractals, a similarity transform changes the structure in all directions with the same coefficient. During the self-affine fractal growth, the transformation coefficients are generally different.

We have calculated the fractal dimensions D of a sample surface and a scan profile for the carbon deposit studied. The surface has $D = 1.8$ and is self-affine, since the size of fractal structures in the z direction is smaller by a factor of 30–50 than that in the x and y directions. The scan profile represents a self-affine curve with a fractal dimension of $D = 1.1$. For random three-dimensional surfaces, the Hurst index H used to characterize self-affine fractals is defined as [4]

$$H = E + 1 - D, \qquad (1)$$

where E is the Euclidean space dimension. For a surface, the Hurst index is related to the fractal dimension as [5]

$$H = 3 - D. \qquad (2)$$

For the surface and a scan profile of the deposit studied, the Hurst indices are 1.2 and 1.9, respectively. By its physical meaning, this quantity represents the cof-
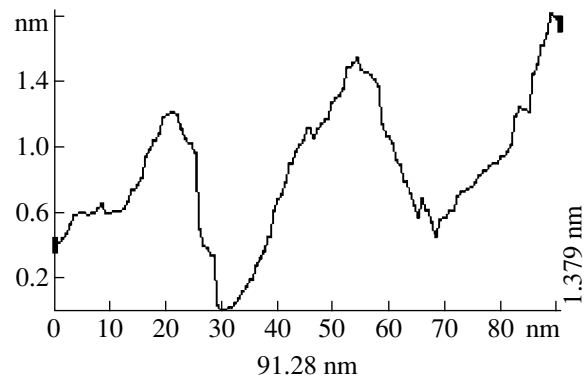

Fig. 2. A typical AFM scan profile of a carbon deposit surface.

ractal dimension. This parameter, used to describe fractals and multifractals, characterizes rough and uneven surfaces.

The carbon deposit studied is composed of clusters with dimensions on the order of one to several nanometers. The specific surface S is calculated by the formula

$$S = 3/\rho r, \qquad (3)$$

where ρ is the density of the carbon deposit and r is the average size (effective radius) of carbon clusters. For $\rho = 1.32$ g/cm^3 and $r = 3$ nm, we obtain $S = 757.6$ m^2/g. Thus, carbon deposits possess very large specific area and, hence, can be used as effective adsorbents.

REFERENCES

1. A. Yoshinori, Fullerene Sci. Technol. **2** (2), 173 (1994).
2. Yu. S. Grushko, V. M. Egorov, and I. N. Zimkin, Fiz. Tverd. Tela **37**, 1838 (1995) [Phys. Solid State **37**, 1001 (1995)].
3. I. V. Zolotukhin, Yu. V. Sokolov, and V. P. Ievlev, Fiz. Tverd. Tela **40**, 584 (1998) [Phys. Solid State **40**, 539 (1998)].
4. Yu. G. Bobro, V. N. Mel'nik, and A. V. Shostak, Metally, No. 3, 109 (1999).
5. S. Talibuddin and J. P. Runt, J. Appl. Phys. **76**, 5070 (1994).

Translated by P. Pozdeev